DNA AND RNA OLIGONUCLEOTIDES IN THERAPY: THE PROMISING APPLICATIONS

Francesca Greco

Dottorato in Biotecnologie – XXXV ciclo

Università di Napoli Federico II

Dottorato in Biotecnologie – XXXV ciclo

Università di Napoli Federico II

DNA AND RNA OLIGONUCLEOTIDES IN THERAPY: THE PROMISING APPLICATIONS

Francesca Greco

Dottorando: Francesca Greco

Relatore: Prof. GennaroPiccialli

Coordinatore: Prof. Marco Moracci

Settore Scientifico Disciplinare CHIM-06

Short abstract

Oligonucleotides are small molecules with easy-to-handle design and rapid production steps that have already proven their extraordinary efficacy, as witnessed by the recent development of mRNA-based vaccines against the SARS-CoV-2 virus.
Natural oligonucleotides are not suitable for therapy and diagnostics due to their low thermal and enzymatic stability and modest bioavailability. Still synthetic oligonucleotide (ODN) analogous are synthesized for increasing their application.
In this contest, my research studied the (ODN) relevance in diagnostics and therapy.

Specifically, my research work has been focused on:

- Chemical synthesis and structural and biological characterization of Peptide Nucleic Acids (PNAs) as antisense oligonucleotide and development of novel delivery platforms

- Stabilization of the c-myc promoter region conformed in G-quadruplexes as promising antitumoral approach.

- Realization of a new supramolecular structures formed by C-rich oligonucleotides (CROs) sequences through the introduction of non-nucleotidic linker.

Long abstract

La tesi di dottorato discute il contributo della mia ricerca all'applicazione degli oligonucleotidi sintetici (ODN) in terapia e nanotecnologia.

Ad oggi, il cancro è la prima causa di mortalità nel mondo e l'interesse globale è rivolto alla ricerca di una terapia anti-tumorale che oltre ad allungare l'aspettativa di vita del paziente non ne infici la qualità di vita. Alla base dell'insorgenza del cancro ci sono mutazioni dell'assetto genetico che determinano alterazione della fisiologica omeostasi cellulare. L'individuazione della mutazione genetica artefice della malignità permette di agire specificamente su di essa implementando la risposta terapeutica. Nel rispetto del dogma DNA-RNA-PROTEINA il tumore si manifesta a seguito dell'espressione deregolata di una proteina; pertanto, arginare tale deregolazione è un mezzo per contenere l'insorgenza della malattia stessa. Il controllo ab-initio dei processi di trascrizione e traduzione all'interno della cellula permette di monitorare l'espressione genica dell'individuo, rappresentando una promettente terapia antitumorale. A tale fine, gli oligonucleotidi, in quanto molecole facili da progettare e sintetizzare, possono essere dei validi strumenti terapeutici. La bassa stabilità enzimatica e la breve emivita di queste molecole limitano la loro promettente applicazione in vivo. A questo proposito, si è proceduti con la progettazione di molecole modificate che conservano le proprietà funzionali degli oligonucleotidi seppur con migliorate caratteristiche chimico-fisiche. Parte del mio percorso di dottorato si è basato sullo studio di sistemi oligonucleotidici a base di mimetici del DNA (PNA) che controllassero attività trascrizionale e di traduzione in cellule di cancro.

Il mio lavoro di tesi ha portato ai seguenti risultati:

1. Progettazione e sintesi di un nuovo oligomero di PNA con attività antisenso contro un tratto dell'mRNA CD5 coinvolto nell'insorgenza della leucemia linfocitica cronica (B-CLL). Il livello di espressione della proteina CD5, sovraregolato nei pazienti affetti da B-CLL, è stato modulato dopo il trattamento con il proposto PNA antisenso. L'effetto biologico decisivo del PNA nell'inibire il meccanismo di traduzione è stato, dunque, confermato.
2. Progettazione di una nuova sequenza di PNA complementare ad una regione del trascritto di PD-L1, il cui coinvolgimento nella genesi del tumore è stato fortemente dimostrato. Il lavoro ha altresì previsto, per la

somministrazione di tale ODN, lo sviluppo di un sistema di rilascio controllato basato su nanoparticelle di diatomite. Il rilascio del PNA sfrutta gli alterati equilibri ossido-riduttivi dell'ambiente tumorale per innescarsi.

3. Progettazione e sintesi di nuovi PNA antitumorali complementari ad un tratto dell'mRNA PD-L1. Quali pionieri nel campo, lo studio ha interessato lo sviluppo di una nuova piattaforma di rilascio per il PNA mediata dalla funzionalizzazione di superficie di un adenovirus oncolitico in grado di infettare e proliferare selettivamente nelle cellule tumorali.

Lateralmente, la mia ricerca si è anche focalizzata sullo studio delle strutture secondarie non canoniche del DNA. Dati dei presupposti di sequenza, DNA ed RNA possono conformarsi in strutture quadruplex a base di Guanine o di Citosine. Tali strutture quando riscontrate nel genoma umano, sono associate a regioni regolatrici di oncogeni house-keeping (promotori e iniziatori). La loro presenza impedisce la normale trascrizione del DNA in RNA perché i fattori adibiti a tale compito non sono in grado di funzionare in loro presenza. La stabilizzazione di tali strutture, soprattutto delle G-quadruplex, è stata riconosciuta come incoraggiante terapia antitumorale. A tale scopo è stato condotto lo studio strutturale per valutare l'interazione di composti naturali con le G-quadruplex. Nota la loro capacità di interagire con il DNA, si è indagata la stabilizzazione derivata dall'interazione delle trans-polidatine con una regione del promotore dell'oncogene c-myc, previamente conformato in G-quadruplex.
Di contro, le C-quadruplex (i-motif) sebbene ampiamente rappresentate nel genoma trovano ottimo riscontro nelle nanotecnologie, date le loro peculiari caratteristiche strutturali. Pertanto ho seguito la progettazione e sintesi di nuovi oligonucleotidi ricchi di citosina strutturalmente modificati mediante linker non nucleotidici. Tali molecole consentono di formare strutture i-motif stabili aprendo la strada all'ingegnerizzazione di nuovi biomateriali a carattere sopramolecolare, pH-sensibili.
Oltre alle indagini sulle catene oligonucleotidiche, parte dei miei studi è stata dedicata anche alla progettazione strutturale e alla sintesi di piccoli nucleosidi quali mediatori intracellulari. Nello specifico ci siamo occupati della sintesi di un mimetico dell'adenosina difosfato ribosio ciclico (cADPR). Sulla base degli

esperimenti in vitro, il composto proposto ha mostrato incrementata attivazione del rilascio di calcio intracellulare in cellule neuronali.
Il potenziale crescente degli oligonucleotidi ed analoghi abbraccia una delle applicazioni moderne delle biotecnologie. Dalla fusione delle scienze naturali e ingegneristiche, la biotecnologia promuove la sintesi di composti che imitano le loro controparti naturali da utilizzare nella diagnostica e nella terapia. Tra questi, i derivati nucleotidici ed oligonucleotidici sintetici, grazie alla loro progettazione maneggevole e alle rapide fasi di produzione, hanno già dimostrato la loro straordinaria efficacia, come testimonia il recente sviluppo di vaccini a base di mRNA contro il virus SARS-CoV-2.

CHAPTER 1 Oligonucleotides and analogues: economical implication of using oligo in therapy and diagnostics.

1.1 INTRODUCTION

The Covid-19 health emergency highlighted the importance of synthetic oligonucleotide applications. Still, aside from the SARS-CoV-2 virus world spreading, the application of ODNs as therapeutics and diagnostics started years ago, finding application in the broad field of genetic disorders acting as genetic drugs [1], fig 1. Unconventionally, genetic drugs do not recognize proteins and enzymes but endogenous nucleic acids (DNA and RNA). Facing up the genome response, ODN-based therapies eradicate congenital diseases avoiding the palliative effects of the traditional drugs[2].
Together with genetic disorders, tumors account for the highest level of mortality, nowadays. The etiology of cancers is related to the production of dysfunctional proteins that alter cellular fitness. The canonical approach for the treatment of metabolic disorders consent to fix symptoms, even the mortal ones, by acting against improper protein targets.
The idea of definably healing patients affected by tumors might be mediated only by gene therapy, i.e. a system that controls the gene expression upstream of the disease onset [3].
With this aim, synthetic oligonucleotides have been more and more studied in the last forty years. Synthetic oligonucleotide chains can specifically recognize and interact with complementary endogenous DNA or RNA strands when introduced in the intracellular compartment[4]. The interaction causes the modulation of the DNA/RNA genetic function i.e. transcription and translation processes.
According to this, and depending on the cellular localization of the interactions, two main kinds of approaches exist the anti-gene and the antisense one.

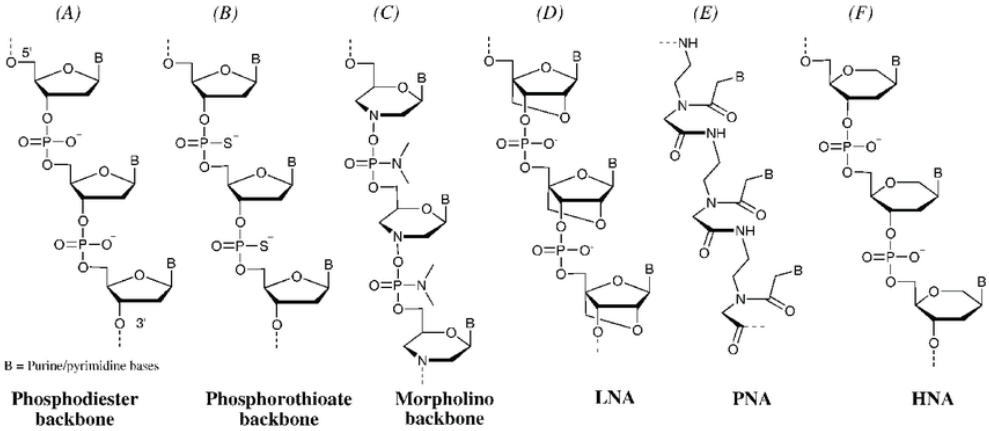

Figure 1 Structures of natural and modified oligonucleotide backbones: (A) natural phosphodiester; (B) phosphorothioate; (C) morpholino; (D) locked nucleic acid (LNAs); (E) peptide nucleic acids (PNAs); and (F) hexitol nucleic acids (HNAs).

Eventually, state of the art in synthetic oligonucleotides is also increasing the application of aptamers in therapy and diagnostics, exploiting their antibody-like activity[5].

Likewise, another class of therapeutics DNA-based is the modified nucleoside[6-7].

In nature, nucleosides represent a class of small molecules needed for regular biochemical processes. Firstly, they represent the building blocks of nucleic acid chains. Then they also act as intracellular messengers for inducing cell responses to internal or external stimuli. Lately, modified nucleosides have shown promising therapeutic effects to mediate the intracellular deficit of nucleic acid bricks and cell mediators that could cause the outbreak of pathological defects. But, they are used as chemotherapeutics for both antitumoral and antiviral approaches. Chemical manipulation of the natural compound could impact its antiviral or antitumoral efficacy and drug resistance. Generally, modified nucleosides can exploit the therapeutical effects because of the ability to be recognized by intracellular important enzymes as substrates.

For many years the ODN studies for their in vivo applications assisted a slow transition from theory to practice due to the ODN's chemical nature. The limitations connected to the ODN spread as therapeutics concerned their low pharmacokinetic profile (short half-time, high degradation, and poor bioavailability). Accordingly, the

synthesis of a compound analogous to oligonucleotides was proposed for conferring higher enzymatic resistance and improved chemical characteristics, such as solubility. The analogous compounds are characterized by chemical modification on the sugar-phosphate backbone of the canonical nucleic acid one or by modification of the reactive group of sugar domains. Phosphorothioate (PS), Methyl phosphonate, N3'-P5 DNA (NP), 2'-O-Methyl(2'-OMe), 2'OMethoxylethyl (2'-MOE) Locked Nucleic Acid (LNA), Morpholino-Oligonucleotide (MO), Phosphorodiamidate morpholino (PMO), S-Constrained ethyl (cEt) and Peptide Nucleic Acid (PNA) are the analogous applied for the development of antisense and anti-gene ODN[8].

The global upset derived from the spreading of the SARS-Cov 2 virus in the last two years induced the scientific community to face novel therapies development for controlling the pandemic effects. The pushing demands for finding antiviral prevention and therapeutic systems allowed the rising of improved synthetic oligonucleotide (ODN) methodologies, such as the mRNA-based vaccine promoted by Pfizer/BioNTech and Moderna companies[9]. The ODNs as a class of therapeutic compounds are characterized by practical advantages such as the easy-to-handle design and rapid production steps and the important property of acting against undruggable targets. The global attempts in the recent health emergency allowed the scientific community to overcome their low distribution pharmacokinetic profile thanks to the development of suitable delivery platforms.

1.2 Market analysis

A market analysis of the past two years has been conducted on the growing application of ODNs. North America, Europe, Asia, Latin America, the Middle East, and Africa represent the protagonists of the global market, fig 2. In 2020, ODN production in North America outperforms other components due to the growing expansion of life science fields, particularly in the research and development sector. The largest number of specialized companies in the field are found in this part of the world focused on volunteering to develop high-quality research instrumentation. The market analysis predicts that the production of oligonucleotides in Asia will grow rapidly, considering the actual large investments in the trade and rising demand.

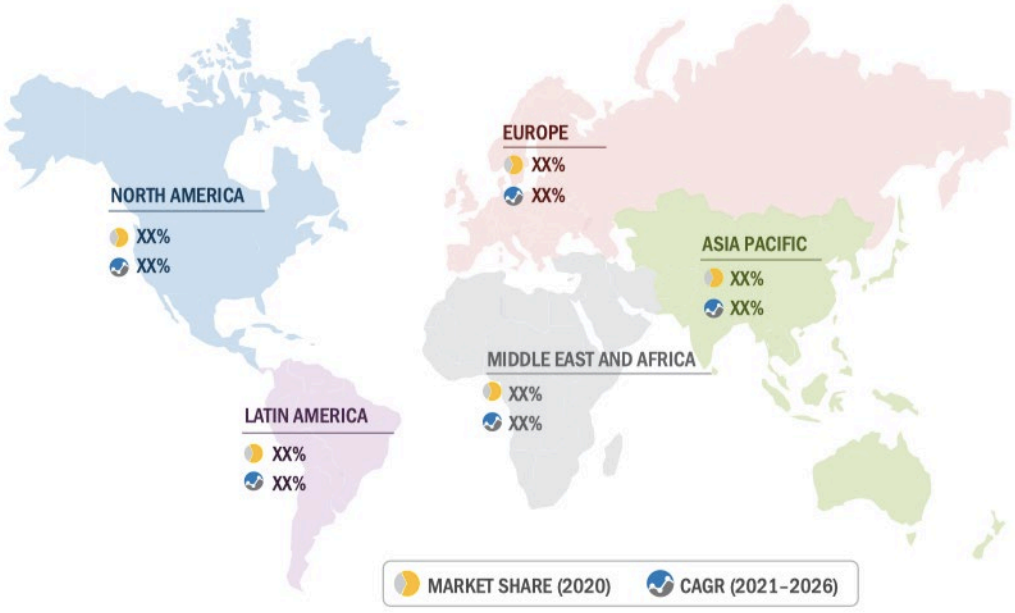

Figure 2- Geographical snapshot of the oligonucleotide synthesis market. Source: World Health Organization (WHO), Food and Drug Administration (FDA), National Center for Biotechnology Information (NCBI), Industry Association of Synthetic Biology (IASB), Biotechno Geographical snapshot of the oligonucleotide synthesis market

The market trend refers to the chemical synthesis of nucleic acid strands, designed with precise structural and operational purposes. Synthetic ODN application is expected to achieve a Compound Medium Growth Rate (CAGR) of XX% to reach USD XX in 2026 from USD XX in 2021. The outcome of generating therapies for the prevention and correction of congenital diseases leads to the study of personalized therapies and ODNs find easy application in this intent despite the difficulties related to practical applications. In the last years, personalized medicine represents a global approach to the prevention, diagnosis, treatment, and monitoring of diseases based on the characteristics, genetic and not only, of a person. The oligonucleotide therapeutic products, embracing these purposes, are considered a rising speculation area, fig.3.

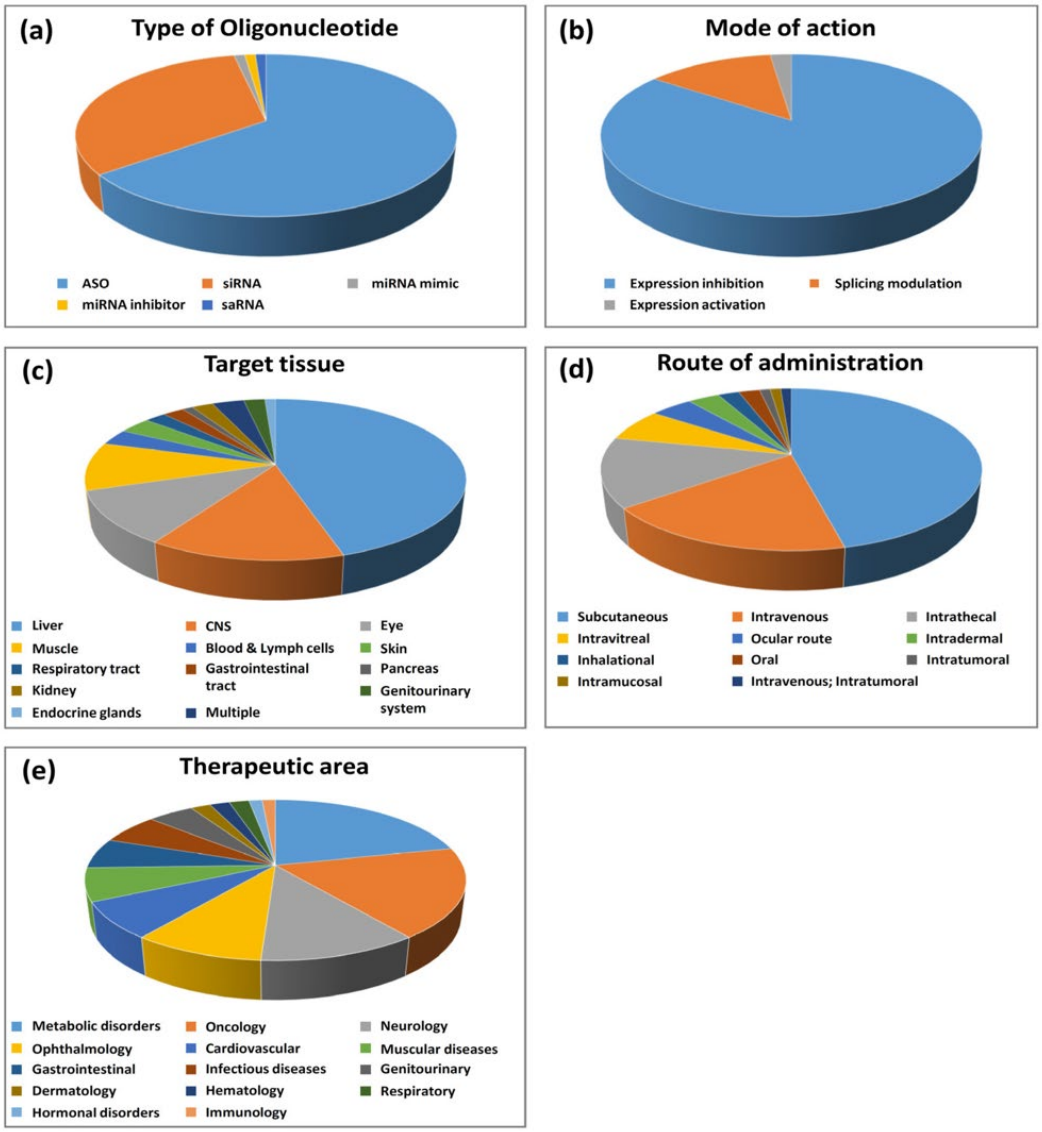

Figure 3 Statistical analysis of oligonucleotides present in the market and in clinical development phase. (a) Type of oligonucleotide; (b) mode of action; (c) target tissue; (d) route of administration; (e) therapeutic area.

Moumné L, Marie AC, Crouvezier N. Oligonucleotide Therapeutics: From Discovery and Development to Patentability. Pharmaceutics. 2022 Jan 22;14(2):260. doi: 10.3390/pharmaceutics14020260. PMID: 35213992; PMCID: PMC8876811.

1.3 Oligonucleotides and analogues in the antigene and antisense strategy

New molecules able to precisely and selectively interact with endogenous DNA or RNA took advancement in human health

protection. The strategies exploit the central role of nucleic acids as carriers of genetic information. The gene expression is mediated by a dual process consisting of two main steps: transcription and translation. In the nucleus compartment of cells, the transcription of a double-stranded DNA brings to the synthesis of many copies of messenger RNAs (mRNAs) ready for being successively converted into protein by the translational machinery. The translation lap is skipped when this stage is interrupted and the gene expression is altered. Together with the transcription mechanism alteration, hindering the mRNA translation in the cytoplasm also arrests protein generation. Gene-drugs oligonucleotide-based, act as a breaker of protein production, sharing a therapeutic approach. The anti-gene ODNs target the genomic DNA controlling the transcription process, while the antisense one targets mRNA sequences and prevents the translational stage.
The synthesis and design of anti-gene or antisense oligonucleotide requires identifying the base content of the sequence to target. The sequence-specific recognition is the crucial point for both approaches; the absence of maximum specificity in the synthetic oligonucleotides makes them stray bullets free to intercept and alter the expression of many sequences in the genome. Hence, the entirely complementary and the minimum length, 15-23 nt, prerequisites assure to keep the specificity and highest selectivity of the interaction.

1.3.1 Anti-gene strategy

In the anti-gene strategy, a synthetic ODN complementary to a gene tract recognizes the target following multiple mechanisms of action such as the triplex formation or the double-helix strand displacement[10-11].
The triplex-forming oligonucleotides (TFOs) belong to the class of ODN therapeutics that interact with a double-stranded DNA through Hoogsteen hydrogen bonds alongside the major groove of the DNA helix. Polypurine and polypyrimidine TFO sequences are mainly required to mediate the polypurine target's recognition common in promoter and intron sequences of genes. TFOs might inhibit transcription by binding with high specificity to the DNA, in that way blocking both the recruitment and function of transcription factors for particular sequences.
TFOs and their targets are usually long, 10-30 nucleotides (nts).

The triplex invasion is also considered a way of interaction with the genomic DNA thanks to a complementary ODN action, able to recognize the same strand in a bis-functional mode. On one hand, the ODN specifically binds the complementary strand of the DNA double-helix, forcing out the not complementary one. On the other hand, the exogenous strand interacts through the Hoogsteen side with the target gaining a three-way-complex. The novel triple-helix system has higher stability compared to the canonical triplex.
According to the strand displacement activity, the ODNs also might promote the DNA duplex invasion, displacing the DNA strands from the double helix. The duplex invasion complexes are unstable due to the endorsement of a DNA loop, fig.4.
The described mechanisms sterically preclude the transcriptional factors and enzyme recruitment inhibiting the transcription. The state-of-the-art anti-gene approach describes that applying synthetic ODNs to arrest the gene transcription does not record huge success due to the ODN's difficulties in reaching the nuclear compartment and the target.

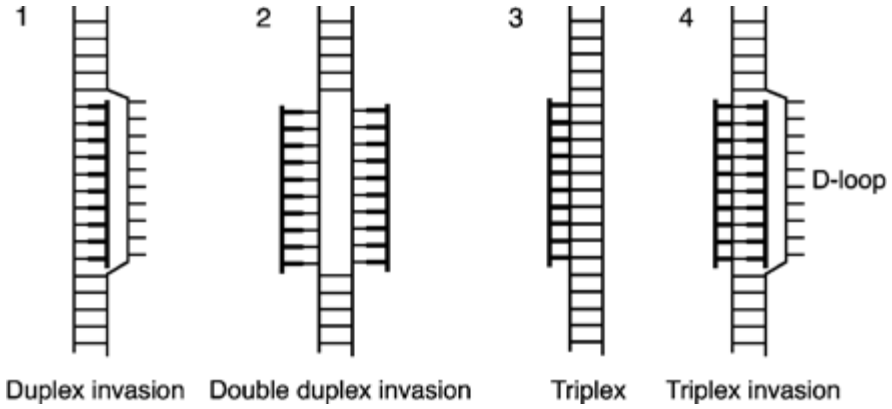

Figure 4 Schema of peptide nucleic acid (PNA) binding modes for targeting double-stranded DNA. PNA oligomers are drawn in bold. (1) Standard duplex invasion complex formed with some homopurine PNA. (2) Double-duplex invasion complex, very stable but only possible with PNA containing modified nucleobases. (3) Conventional triple helical structure (triplex) formed with cytosine-rich homopyrimidine PNA binding to complementary homopurine DNA targets. (4) Stable triplex invasion complex, leading to the displacement of the second DNA strand into a 'D-loop'.

F. Pellestor, P. Paulasova, M. Macek, S. Hamamah, The peptide nucleic acids: a new way for chromosomal investigation on isolated cells?, Human Reproduction, Volume 19, Issue 9, September 2004, Pages 1946–1951, https://doi.org/10.1093/humrep/deh386

1.3.2 Antisense strategy

The antisense strategy, providing the degradation of mRNA molecules, obtained more remarkable success in therapy, fig.5, than the anti-gene approach for two main reasons: the target intracellular localization and the number of disposable targets.
The cytoplasmatic mRNA localization helps the ODNs activity by allowing the target easy-to-reach mechanism after the cellular internalization. The internalization of ODNs represents one of the main problems for their application, and developing a delivery platform is often necessary.
The transcription of a single gene brings numerous copies of mRNA, making mRNA more manageable objectives to silence or control.
The inhibition mechanisms behind mRNA silencing are diverse[12-13]. The Watson and Crick base pairing is the driving force of the ODN activity that explicitly recognizes the mRNAs to down-regulate forming a partially double-stranded mRNA. The downregulation process is mediated by:

- Activation of the RNase H enzyme cleaves the RNA-ODN heteroduplex and degrades the target mRNA, leaving the ASO intact.

- Arresting the started translation step by inducing the steric hindrance and preventing the conventional ribosomal activity.

- Destabilizing the pre-mRNA in the nucleus is the less known mechanism.

Disease	Targeted gene	Targeting agent	Pursued by	Latest status
Acromegaly	Growth hormone receptor	antisense	ISIS/Antisense Therapeutics Limited	Ph 2 recruiting
Hepatitis C virus	*miR-122*	LNA-antimir	Santaris	Ph 2 ongoing
Hypercholesterolemia	*ApoB-100*	antisense	ISIS/Genzyme	Approved by FDA
Hypercholesterolemia	*ApoB-100*	siRNA	Tekmira	Ph 1 terminated
Hypercholesterolemia	*ApoB-100*	LNA	Santaris	Ph 1 completed
Hypertriglyceridemia	*ApoCIII*	antisense	ISIS	Ph 2 recruiting
Hypercholesterolemia	*PCSK9*	siRNA	Alnylam/Medicines Company	Ph 1 completed
Hypercholesterolemia	*PCSK9*	LNA	ISIS/BMS	Ph 1 halted
Inflammatory disorders	*CRP*	antisense	ISIS	Ph 2 recruiting
Liver cancer	*KSP/VEGF*	siRNA	Alnylam	Ph 1 completed
Liver cancer	*PLK1*	siRNA	Tekmira/Protiva	Ph 1 ongoing
Liver cancer	*miR-34*	miRNA mimic	miRNA therapeutics	Ph 1 recruiting
Obesity	*FGFR4*	antisense	ISIS/Verva Pharmaceuticals	Ph 1 ongoing
Thrombosis	Factor IXa	aptamer	Regado Biosciences	Ph 2a completed
Thrombosis	Factor XI	antisense	ISIS	Ph 2 recruiting
TTR amyloidosis	*TTR*	antisense	ISIS/GSK	Ph 3 recruiting
TTR amyloidosis	*TTR*	siRNA	Alnylam	Ph 2 recruiting
Type 2 diabetes	*GCCR*	antisense	ISIS	Ph 1 ongoing
Type 2 diabetes	*PTP-1B*	antisense	ISIS	Ph 1 completed
Cushing's syndrome	*GCGR*	antisense	ISIS	Ph 1 ongoing

Figure 5 Oligonucleotide therapeutics in clinical trials.

https://doi.org/10.1016/j.jhep.2013.05.045.

1.3.3 ASO, Antisense Oligonucleotide, design and synthesis.

Even though the Watson and Crick interaction leads the action of ASOs, the stability of the interaction strongly depends on diverse factors, and ODN synthetic scheme must consider the following parameters:

- thermodynamics stability of the hybrid RNA:ODN complex;
- preformation of the target mRNA in secondary structures;
- the closeness of the hybridization locus to some operative domains.

For the designing of the ASO strand to get the highest winning result, the ASO sequence must be predicted to not conform to the secondary structure and to the target to avoid the failure of the hybridization. In silico analysis based on the bioinformatic tool, table 1, is used for the structural and binding energy predictions.
Based on experimental evidence, the presence of CCAC, TCCC, ACTC, GCCA, and CTCT motifs in the ASOs was associated with positive results in terms of hybridization rate[14].

BIOINFORMATIC TOOLS:	
REVERSE TRANSLATE- BIOINFORMATICS	https://www.bioinformatics.org/sms2/rev_trans.html
OLIGOANALYZER TOOL ™-IDT	https://eu.idtdna.com/pages/tools/oligoanalyzer
BLAST	https://blast.ncbi.nlm.nih.gov/Blast.cgi
NCBI	https://www.ncbi.nlm.nih.gov/
UniProt	https://www.uniprot.org/

Table 1 Bioinformatic tools used for the design of promising ASO strands.

1.3.4 Non-coding RNAs as target: anti-miRNA and anti-siRNA strategies

miRNA and siRNA are two non-coding RNA types involved in gene regulation[15], fig.6. They also serve as a new class of therapeutic agents in the treatment of cancers and infections. Mirna and siRNA are short, duplex RNA molecules that exert gene-silencing effects by targeting messenger RNA (mRNA) at the post-transcriptional level. Although their function is similar to gene silencing, the mechanisms of action and clinical applications differ. The main difference between miRNA and siRNA is that miRNA can act on multiple target mRNAs, but siRNA only acts on a single mRNA target, which is very specific to the siRNA type. The miRNA strands repress the translation by degrading mRNAs, and no endonucleolytic cleavage occurs. Conversely, siRNAs regulate gene expression by endonucleolytic cleavage, finding that the therapeutic approaches of miRNA and siRNA are also different. Administration of ODN complementary to miRNA/siRNA or miRNA/siRNA mimic represents another modality of controlling gene expression.

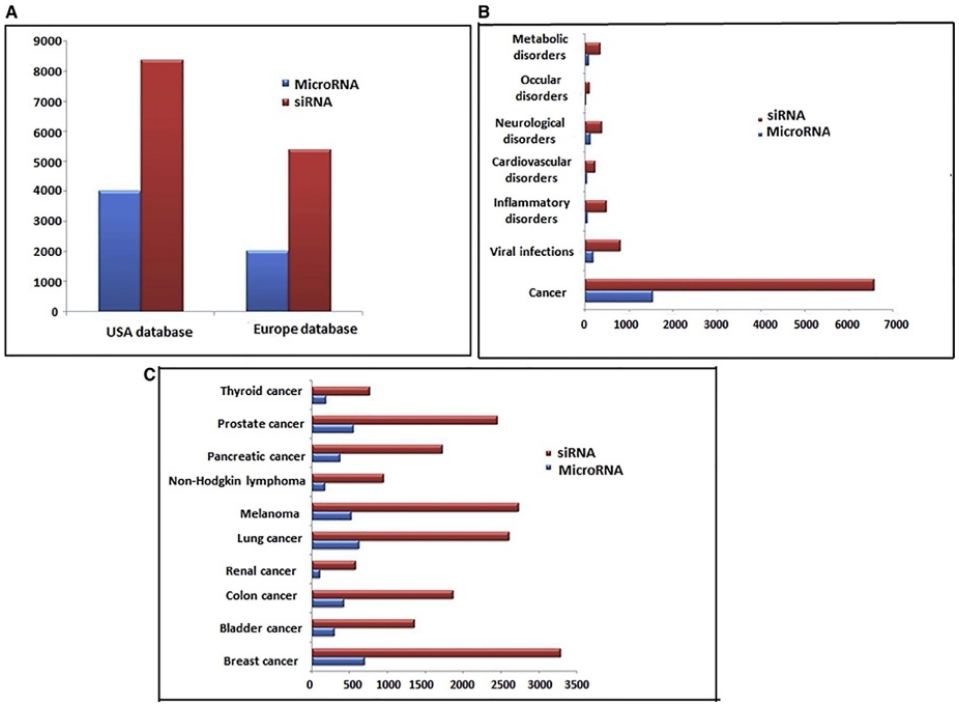

Figure 6 miRNA and siRNA Patents (A) Total number of keyword searches ("microRNA" and "siRNA") performed in both the US patent search database and the European patent office database. (B) Number of patents in "microRNA" and "siRNA" in case of the different diseases. (C) Number of patents in "microRNA" and "siRNA" in event of the different type of cancers[5].

1.4 Nucleosides and modified nucleosides

Nucleoside units are made up of a nitrogen base linked to the sugar moiety, usually a pentose residue via an N-glycosidic bond. The natural nucleosides are represented by the deoxyribose and ribose sugar contents joined to a purine or pyrimidine base. The biological role of these molecules is to compose the nucleic acid chains and contribute to signaling pathways as soluble compounds. In nature, modified nucleosides are diffused, and they primarily build the non-coding RNA, especially tRNA. Synthetically modified nucleosides, fig.7, are molecules that are structurally like the natural ones but induce a different response in the cell homeostasis, acting as antimetabolites or improving the cellular response by acting as mimics[16-17]. Nucleoside analogs cross the cell membrane due to the interaction with nucleoside transporters. Once reached the cytoplasm, they are mono or bis phosphorylated by kinases. The

phosphorylation converts the inactive compounds in active ones suitable to work as intracellular substrates.

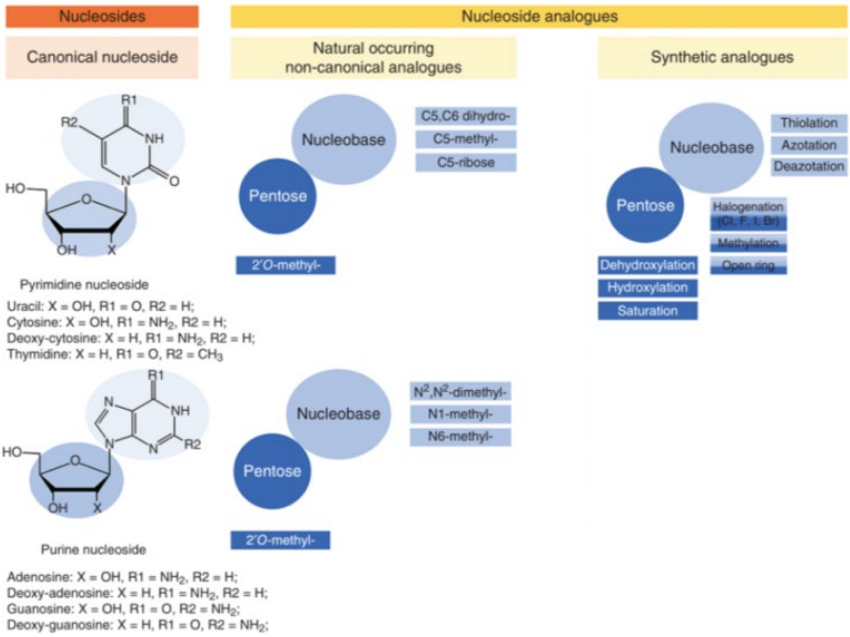

Figure 7 Classification of nucleotide and nucleoside analogues.

1.5 Aptamers

Aptamers, also known as chemical antibodies, are nucleic acid-based compounds (20-100 nt) able to peculiarly bind a target measuring a very low or a total absence of off-target responses. In the aptamer architectures, the oligonucleotides exploit the secondary structure conformation to recognize specifically and precisely target, usually a protein. They derived from the Systematic evolution of ligands by exponential enrichment (SELEX) cyclic technique, where starting from a ten-thousand-long ODN library, only one ODN is isolated for its highest specificity protein binding rate.

The in vitro process described by Tuerk and Gold (1990) and Ellington and Szostak (1990) involves the progressive selection of aptamers, by the repetition of binding cycles and the elution and amplification of ligands from a random nucleic acid library (DNA and RNA) to the selection of sequences with a higher binding affinity for the target is achieved[18-19]. The differences in the majority of RNA SELEX fig.8 A protocols, compared to DNA SELEX, fig.8B, include:

i) the protection of RNA from RNAases through modifications of their ends 5 'or 3', ii) amplification by T7 RNA polymerase and iii) reversed transcription step before PCR. After this iterative process, the resulting nucleic acid molecules can be chemically modified, in order to provide them additional properties and, above all, to extend their half-life in biological fluids. The characteristics of the selected ONs are identified by using various physical, chemical, and biological assays.
Aptamer's targets are small molecules, metallic ions, and proteins, table 3.

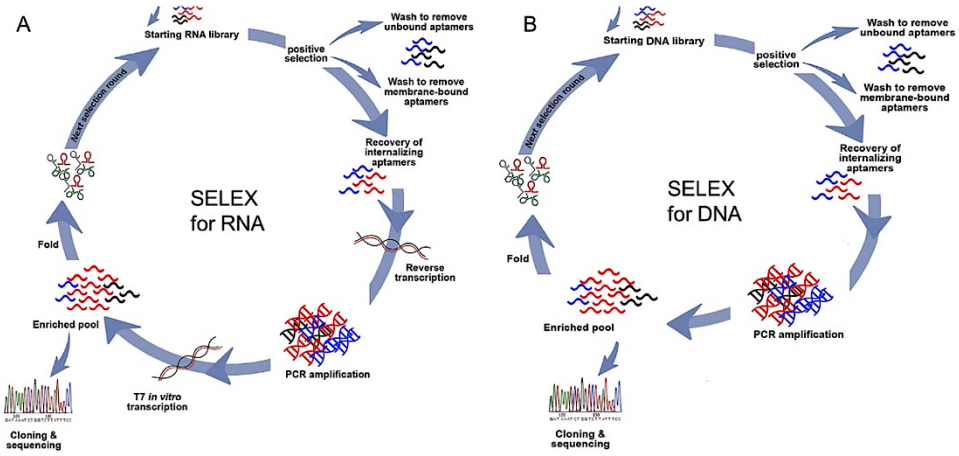

Figure 8 DNA and RNA SELEX processes.

Aptamer Name	Company	Target	Indication	Clinical Stage
Macugen (Pegaptanib)	Eyetech Pharmaceuticals/ Pfitzer	VEGF-165	AMD Diabetic retinopathy	Approved Phase III
E10030	Ophthotech Corp./Archemix Corp.	PDGF-B	AMD	Phase II
ARC1905	Ophthotech Corp./Archemix Corp.	C5	AMD	Phase I
ARC1779	Archemix Corp.	vWF	TMA	Phase II
NU172	ARCA Biopharma/ Archemix Corp.	Thrombin	Acute coronary artery bypass surgery	Phase II
REG-1 (RB006/RB007)	Regado Biosciences/ Archemix Corp.	Factor IXa	Percutaneous coronary intervention	Phase II
NOX-A12	NOXXON Pharma	SDF-1α	Lymphoma patients (undergoing autologous stem cell transplantation)	Phase I
NOX-E36	NOXXON Pharma	CCL2	Type 2 diabetes and diabetic nephropathy	Phase I
AS1411 (AGRO001)	Antisoma/Archemix Corp.	Nucleolin	AML	Phase II

Table 3 Aptamer in clinical trials.

New insight into clinical development of nucleic acid aptamers - Scientific Figure on ResearchGate. Available from: https://www.researchgate.net/figure/Aptamers-in-Clinical-Trials_tbl1_51450919 [accessed 14 Oct, 2022]

1.6 Approved delivery platform and intracellular uptake in vivo nucleic acid therapeutics.

In the clinic, the subcutaneous, intravitreal and intrathecal routes of administration are tested for approved ODN drugs, fig 9. Depending on the clinical effect, the intracellular absorption of ODN varies. The most common ODNs in the preclinical and clinical phases are the ASOs. Their intracellular uptake is mediated by various cell surface proteins, including receptors, which can interact with ASOs directly or via ASO-conjugated ligands. The cell surface receptor can internationalize them via clathrin- or caveolin-dependent endocytic pathways or unconventional endocytic pathways, including macropinocytosis.

The asialoglycoprotein receptor (ASGPR) regulates the delivery of GalNAc - siRNA conjugates to hepatocytes[21].

Besides the siRNAs loaded into the Lipid Nanoparticles (LNPs) follow the intracellular uptake of the low-density lipoprotein receptor (LDLR). Intramuscular administration is the preferred route of administration for LNP-mRNA vaccines due to the high stimulation of the immune system response[22]. Adeno-associated viruses (AAVs) as vectors are used with dual routes of administration: local and intravenous administration.

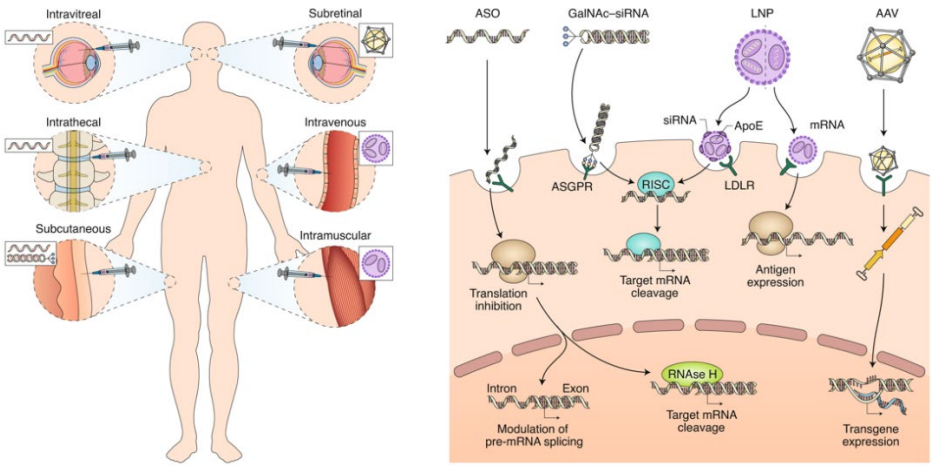

Figure 9 Routes of administration and modes of action for approved in vivo nucleic acid therapeutics.

Nature Nanotechnology (Nat. Nanotechnol.) ISSN 1748-3395 (online) ISSN 1748-3387

1.7 Aim of thesis

The aim of the thesis bears the extensive field of application of oligonucleotides.

The main core of my Ph.D. work is based on developing dual innovative approaches ODN-based:

1. the synthesis of valid oligonucleotide analogs proper for antisense strategy;
2. studies of DNA secondary structure models acting both as target and effective molecules.

Within the antisense field, the tumoral onset was widely investigated and two different targets were identified and explored. As a starting point, B-cell chronic lymphocytic leukemia (B-CLL), the most frequent type of leukemia in adults, was studied. The clonal expansion of mature CD5+ B-lymphocytes accumulating in peripheral blood, bone marrow, and lymphatic tissues causes the arising of the tumor spreading. In order to inhibit cancer growth we targeted the CD5 transcript for downregulating its exposure on the B-cell surface.

Out of this, we studied the PD-L1 transmembrane protein level of expression, whose pivotal role in cancer was commonly proven. As previously described, the antisense approach PNA based was explored but in addition, we developed two alternative delivery platforms. The corroboration of a tissue-specific response mediated by a redox-responsive system and oncolytic adenovirus release approach compared to undelivered compounds was demonstrated.

The dynamic conformation of the oligonucleotide lends itself to active modification of its structure. The formation of secondary structures has assisted conspicuous molecular mechanisms such as the control of gene expression. In this regard, we extensively analyzed the genomic oncogenes forming the G-quadruplex alternative structure. Stabilization of the c-myc oncogene via ligand interaction has been demonstrated and used as proof of concept for novel anticancer approaches.

Consistently, the engineering of DNA and RNA structures due to the dynamism of oligonucleotide-based constructs paved the way for polymer-oligonucleotide nanomaterials. The construction of peculiar DNA secondary structures, I-motifs, has been investigated to obtain promising architectures suitable for several therapeutic employments.

Even though the promising application of the aforementioned strategies, the ODN's effective employment as therapeutics is still limited due to the occurrence of weak points such as:

• poor bioavailability and low enzymatic resistance of natural oligonucleotides;
• lack of new proven delivery systems;
• deficiency of innovative and more specific anticancer treatments.

Within this context, my thesis work is committed to addressing these application limits.

1.8 References.

1. Borbone, N.; Piccialli, I.; Falanga, A. P.; Piccialli, V.; Roviello, G. N.; Oliviero, G. Nucleic Acids as Biotools at the Interface between Chemistry and Nanomedicine in the COVID-19 Era. International Journal of Molecular Sciences. MDPI April 1, 2022. https://doi.org/10.3390/ijms23084359.
2. Kulkarni, J. A.; Witzigmann, D. The Current Landscape of Nucleic Acid Therapeutics. https://doi.org/10.1038/s41565-021-00898-0.
3. Wirth, T.; Parker, N.; Ylä-Herttuala, S. History of Gene Therapy. Gene 2013, 525 (2), 162–169. https://doi.org/10.1016/j.gene.2013.03.137.
4. Lundin, K. E.; Gissberg, O.; Smith, C. I. E. Oligonucleotide Therapies: The Past and the Present. Human Gene Therapy. Mary Ann Liebert Inc. August 1, 2015, pp 475–485. https://doi.org/10.1089/hum.2015.070.
5. Song, K. M.; Lee, S.; Ban, C. Aptamers and Their Biological Applications. Sensors 2012, 12 (1), 612–631. https://doi.org/10.3390/s120100612
6. Parker WB, Secrist JA 3rd, Waud WR. Purine nucleoside antimetabolites in development for the treatment of cancer. Current Opinion in Investigational Drugs (London, England : 2000). 2004 Jun;5(6):592-596. PMID: 15242246.
7. Kimura, Ken-ichi, and Timothy DH Bugg. "Recent advances in antimicrobial nucleoside antibiotics targeting cell wall biosynthesis." Natural product reports 20.2 (2003): 252-273.
8. Glen F. Deleavey, Masad J. Damha,Designing Chemically Modified Oligonucleotides for Targeted Gene Silencing,

Chemistry & Biology, Volume 19, Issue 8, 2012, Pages 937-954, ISSN 1074-5521,https://doi.org/10.1016/j.chembiol.2012.07.011.
9. Liang Y, Huang L and Liu T (2021) Development and Delivery Systems of mRNA Vaccines. Front. Bioeng. Biotechnol. 9:718753. doi: 10.3389/fbioe.2021.718753
10. G. Felsenfeld and A. Rich, “Studies on the formation of two- and three-stranded polyribonucleotides,” BBA - Biochim. Biophys. Acta, vol. 26, no. 3, pp. 457–468, 1957.
11. P. B. Dervan, “DNA-Binding Molecules of,” 1968.
12. S. T. Crooke, “Progress in Antisense Technology,” Annu. Rev. Med., vol. 55, no. 1, pp. 61–95, 2004.
13. N. Dias and C. A. Stein, “Antisense oligonucleotides: Basic concepts and mechanisms,” Mol. Cancer Ther., vol. 1, no. 5, pp. 347–355, 2002.
14. Chan JH, Lim S, Wong WS. Antisense oligonucleotides: from design to therapeutic application. Clin Exp Pharmacol Physiol. 2006 May-Jun;33(5-6):533-40. doi: 10.1111/j.1440-1681.2006.04403.x. PMID: 16700890.
15. Chiranjib Chakraborty, Ashish Ranjan Sharma, Garima Sharma, C. George Priya Doss, Sang-Soo Lee, Therapeutic miRNA and siRNA: Moving from Bench to Clinic as Next Generation Medicine, Molecular Therapy - Nucleic Acids, Volume 8, 2017, Pages 132-143, ISSN 2162-2531,https://doi.org/10.1016/j.omtn.2017.06.005.
16. Rachakonda, Suguna, and Leanne Cartee. "Challenges in antimicrobial drug discovery and the potential of nucleoside antibiotics." Current medicinal chemistry 11.6 (2004): 775-793.
17. Simons, Claire, Qinpei Wu, and Thet T. Htar. "Recent advances in antiviral nucleoside and nucleotide therapeutics." Current Topics in Medicinal Chemistry 5.13 (2005): 1191-1203.
18. Miura, Shinji, and Shunji Izuta. "DNA polymerases as targets of anticancer nucleosides." Current drug targets 5.2 (2004): 191-195.
19. S. C. B. Gopinath, “Methods developed for SELEX,” Anal. Bioanal. Chem., vol. 387, no. 1, pp. 171–182, 2007.
20. C. P. Rusconi et al., “RNA aptamers as reversible antagonists of coagulation factor IXa,” Nature, vol. 419, no. 6902, pp. 90–94, 2002.

21. Crooke, S., Wang, S., Vickers, T. et al. Cellular uptake and trafficking of antisense oligonucleotides. Nat Biotechnol 35, 230–237 (2017). https://doi.org/10.1038/nbt.3779
22. Albertsen, Camilla Hald, et al. "The role of lipid components in lipid nanoparticles for vaccines and gene therapy." Advanced Drug Delivery Reviews (2022): 114416.
23. Chan, Ying Kai, et al. "Engineering adeno-associated viral vectors to evade innate immune and inflammatory responses." Science translational medicine 13.580 (2021): eabd3438.

CHAPTER 2 Peptide nucleic acids (PNAs): an important tool for the modulation of gene expression

2.1 INTRODUCTION

Peptide Nucleic Acid is the most used analogous of DNA and RNA and was discovered during the 1990s by groups of biochemist Peter Nielsen and organic chemist Ole Buchardt[1].
It replaces the nucleic acid sugar-phosphate backbone with a peptidyl one. Units repeated of N-2-aminoethylglycine join the terminal carboxyl groups to the canonical nitrogenous bases by methylene bridges. Its backbone is acyclic, achiral and neutral. The novel scaffold properly orients the nucleobases without affecting the duplex formation respecting the orientation and disposition in the space of the bases that are still able of matching with complementary PNA, DNA and RNA counterparts, fig.10. Surprisingly, the stability of the base pairing is enhanced as a result of lack of charges and electrostatic repulsions. PNA demonstrates to form preferentially heteroduplex complexes in a more selective and specific way compared to the DNA and RNA strands. They recognize and hybridize complementary strands following different modes, namely: parallel, antiparallel, triplex and strand invasion. Among them the antiparallel pairing resulted to be the most stable, thermodynamically. Furthermore, the substitution of the natural scaffold with a synthetic one, protects PNAs from the enzymatic degradation in cell compartments. So, the improved thermodynamic facilities and the enhanced enzymatic stability elected PNA as a successful mimic among the other xeno-nucleic acids, even though the synthetic backbone confers PNA low water solubility and still low intracellular distribution. For the aforementioned skills, PNA is mostly used for controlling the gene expression by anti-gene, antisense, and antimiRNA activities[2].

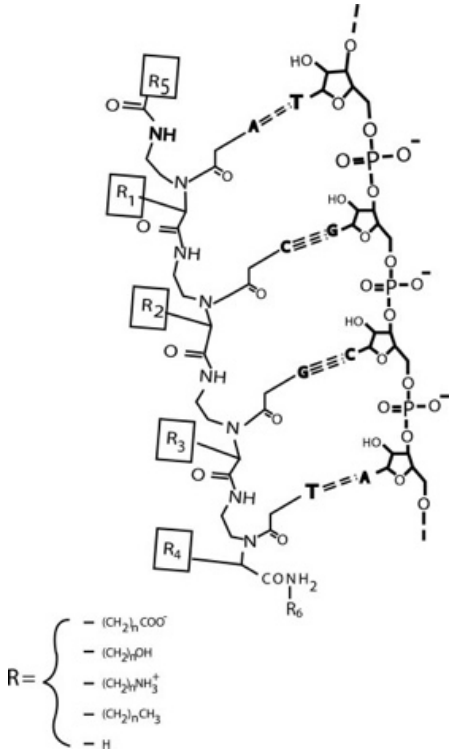

Figure 10 PNA base paring with complementary DNA and RNA.

2.2 Synthesis, purification, and characterization of PNA

PNA can be synthesized using automated procedures (Mayfield and Corey, 1999) or manual methods (Norton et al., 1995). The large-scale synthesis records high yields following the manual Fmoc or Boc solid-phase strategy. For the solid phase synthesis, the solid support is insoluble in the synthetic condition, and orthogonally functionalized respect to the PNA monomers are functionalized in harmony with the synthetical strategy. The rink amide resin is an example of solid support used for the PNA elongation. The synthesis procedure is a cycling process made up of five stages: deprotection, pre-coupling, coupling, capping, and detachment of the raw PNA from the support. The synthesis starts with the swelling procedure, required for the distension and activation of the functionalized solid support. It is performed only at the beginning of the synthesis. For proceedings with the PNA chain's elongation, a synthesis protocol congenial to the protecting groups' reactivity must be used.

Generally, Boc or Fmoc protecting groups at the -NH2 terminal of each monomer are used, as in the peptide synthesis. The formation of Boc-protected amine amino acids or PNA monomers is conducted under either aqueous or anhydrous conditions, by reaction with a base and the anhydride Boc2O. Whereas the Fmoc monomers were obtained by reacting the amine with fluorenylmethyloxycarbonyl chloride with the amino acids or PNA monomer.
Deprotection is the first step of the synthetic cycle. In the case of Fmoc-based synthesis[3], the deblocking step removes the Fmoc protecting group from the resin, amino acids, and PNA monomer.
Fmoc groups are removed by basic treatment with 20% piperidine in DMF, in soft agitation for 2-20 minutes. A more substantial base, 2% DBU in DMF, may be used for challenging deprotections. To accomplish the coupling step, the carboxylic acid group attaching the amino group of the incoming monomer must be activated in a previous step called precoupling. To promote the success of the coupling reactions, an excess of activators, such as HBTU, HCTU, Py BOP, HATU, HOBt/DIC, or DCC, is added and dissolved in a base solution. The bases used during coupling are DIPEA. Generally, the activator/base ratio should be 1:2 to 1:4, and typical monomer solution concentrations range from 0.1 to 0.5 M in DMF. The coupling efficiency determines the final purity of the elongated chain. The lasting of the coupling step depends on the activator used, the monomer coupled, and the sequence of the PNA. The chemical structure of the monomers reacting might tend to aggregate or clump together, hiding the reactive sites at the end of the peptide chains and preventing the success of the next elongation steps. Various methods can be employed to reduce the effects of aggregation, including using different solvents such as NMP, chaotropic salts, or conditions of synthesis such as elevated temperature or microwave stimulation. The excess reagents in the reacting batch must be eluted away from the resins. Copious washings were performed before continuing with the process (2 to 6 times for 30 seconds) because otherwise, the residual unreacted monomers could sterically limit the next coupling steps or any piperidine left after the deblock phase could preventively remove the Fmoc group from the monomer to be introduced, for example. Capping, the last step of the synthetic cycle, is performed to permanently acetylate possible unreacted amino groups from the prior coupling reaction or the N-terminus of a completed PNA. Typical capping solution compositions include 1:1:3 acetic

anhydride/base/DMF, where pyridine or DIPEA may be used as the base.
Blocking the reactivity of the cortamers determines a more straightforward purification step after the compound's detachment from the support.
Eventually, one step performed in a 90% TFA solution is used to deprotect the side chains of monomers added and detach the PNA from the resin. The addition of scavengers (EDT, water, thioanisole, TIS, and phenol) into the detachment solution is necessary to avoid the deprotected groups' reattachment to the reactive ones.
After the total evaporation of TFA, the crude PNA was isolated by precipitation treating the batch with cold diethyl ether, and the sediment was then purified through reverse phase C-18 column using the support of UV-HPLC instrumentation.
The purification step is a critical point an ad hoc protocol is required usually exploiting the eluotropic strength of an apolar solvent such as Acetonitrile.
A standard protocol of purification:

- Centrifuge a PNA solution for 3 min at 12,000 × g, room temperature, to remove particulate.
- Heat a C18 reversed-phase HPLC column to 55°C.
- PNAs tend to form internal structures or higher-order aggregates; sharper peaks will often
- be obtained if the column is maintained at 55°C using a heated water jacket
- Set up a gradient of 0% to 100%(v/v)RP-HPLC buffer B in buffer A for a time from 30 to 45 minutes
- Inject sample
- Collect fractions corresponding to major peaks.

2.3 Limits of PNA application in therapy
The successful activity of the PNA as therapeutics faces its losing chemical asset that limits its use. The peptide backbone, charge-lacking, does not consent to PNA crossing cell membranes. On account of this, without a delivery instrument or a transfection method, PNA does not reach sufficient intracellular concentration for carrying out the desired therapeutic efforts (anti-gene, antisense, or antimiRNA). Thus, the occurrence of PNA backbone’s modifications or PNA conjugation with platforms (nanoparticles, nanotubes, carriers, liposomes) is used to module the intracellular uptake of

PNAs. In addition, the development of a suitable system might also mediate a specific compartment or specific-tissue PNA distribution[4].

2.4 Modification and nature of the PNA backbone

In 1991, for the first time the aminoethylglycyl (aeg) PNA was proposed. It was described as a triplex-forming ODN, sharing a novel triplex invasion mode of action. The original asset of the aeg was poorly soluble in water and lowly responsive to intracellular uptake, limiting its application. To overcome its restricting appliance improved and modified aeg PNA models were continuously tested. Firstly, the introduction of diverse functional groups into the PNA backbone enhanced the solubility and cellular uptake. Considering that several attempts of modifying were tried, the tested chemical modifications are divided into three categories[5](fig.11):

- acyclic backbone modification
- cyclic backbone modification
- modification that does not follow the aeg PNA template.
-

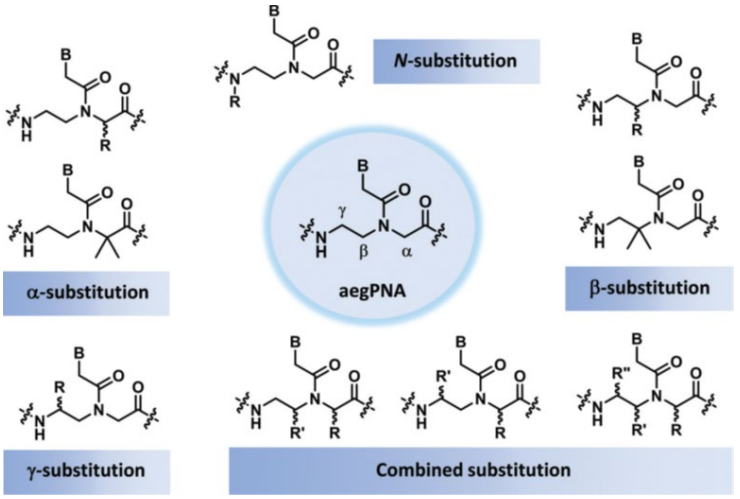

Figure 11 Schematic representation of PNA chemical modification

2.3.1. Backbone modification

Functionalization of the PNA scaffold on the C (2) or C (5) position with positively charged akylammonium, akylguanidium, and PEG residues was experimented with. The optimized intracellular uptake and increased target affinity were found, even though the synthetic procedure of the modified compounds is long and difficult. These findings pushed to explore alternative ways for improving its cellular uptake.

2.3.2. Conjugation with carriers

The dynamism of PNA synthesis allows designing the PNA strands to adjust their cell delivery according to the desired application. Consequently, the addition of peptidyl residue at PNA terminals is used to regulate the overall charge of the PNA. The addition of the serine phosphate residue confers on PNA backbone a negative charge, suitable for the complexation of lipofectamine, used as a standard for the intracellular trasfection of exogenous DNA and RNA molecules, for example. PNA solubility depends on the base content and size, but can be augmented by conjugating charged residues or other solubility-enhancing molecules. PNAs have been subjected to terminal modification with charged L-lysine to improve their limited aqueous solubility and self-aggregation.
It was reported that PNA system modified as descibed are able to cross the cell membranes and interfere with the intracellular processes.

2.3.3. Delivery platform

Nanomedicine, as arising field of research, develops nanometric-scaled delivery platform based on nanoparticles, nanotubes or surfaces, also known as smart nanosystems. The PNA delivery mediated by these platforms is widely studied and tested in the last years reaching optimal results. Lately, novel delivery platforms are based on the functionalization of living organism, such as viruses or bacteria. Above all, the promising application of nanomedical carriers lies in the construction of tunable tools with specific-tissue and/or controlled release.

2.4 The aim of the work

Peptide Nucleic Acids (PNAs) are oligonucleotides that mimic DNA and RNA by replacing the sugar-phosphate backbone with a neutral peptidyl group enabling the precise recognition of a complementary DNA or RNA strand and the formation of a more robust heteroduplex complex suitable for the antisense and antigene therapeutic approach.

During my Ph.D. course as first point (Objective 1) I studied the ability of an antisense PNA to specifically downregulate the expression of a mRNA target. For the study we used the lipofectamine transfection method for assessing the ability of the PNA to accomplish its downregulative role. The research, developed in collaboration with a molecular biologist team, foresaw the synthesis of a PNA complementary to the CD5 mRNA, a protein that is over expressed in the the B-cell Chronic Lynfocitic Leukemia outbreak.

Objective 1 Exploring a peptide nucleic acid-based antisense approach for CD5 targeting in chronic lymphocytic leukemia (Publication n°4)

B-cell chronic lymphocytic leukemia (B-CLL), the most frequent type of leukemia in adults, is characterized by the clonal expansion of mature CD5+ B-lymphocytes that accumulate in peripheral blood, bone marrow, and lymphatic tissues [6,7]. CD5 is a surface glycoprotein expressed in normal T-lymphocyte and only in a small subset of B-lymphocytes. Additionally, its aberrant expression is detected in some B-lymphocyte malignancies, including B-CLL, for which immunophenotyping diagnostic protocols include detection of cell surface CD5 antigene [8]. Recently, CD5 expression levels have also been proposed as a novel prognostic marker [9–11]. The presentation and course of CLL are highly variable. In some cases, the disease is latent, whereas in others, it rapidly progresses with an aggressive course. Despite significant progress in therapy options, the more severe conditions are characterized by an inadequate response to conventional treatment and the development of drug resistance. Accordingly, novel treatments efficiently directed toward specific CLL targets still lack and represent an urgent medical need. Recent compelling evidence suggests that CD5 abnormal expression is involved in the

development and progression of B-CLL through negative regulation of BCR-induced signaling or signaling pathways triggered by CD5 itself [12–14]. Therefore, besides representing a diagnostic and prognostic marker, CD5 is emerging as a promising therapeutic target in B-CLL [15]. CD5 is highly expressed in B-CLL cells, but it is almost undetectable in normal B-cells, thus supporting a role of CD5 as a specific target for B-CLL. In the light of this evidence, many preclinical studies are being conducted to explore the potential use of anti-CD5 immunotherapy approaches in B-CLL treatment [16,17]. In addition, the inhibition of CD5 expression by antisense strategies based on natural and modified oligonucleotides (ONs) could represent a valid alternative approach to be explored [18]. With this aim, in this paper we evaluated the feasibility of an antisense Peptide Nucleic Acid (PNA)-based approach to target CD5. PNAs are synthetic analogs of DNA and RNA in which the canonical sugar-phosphate backbone is replaced by an N-(2-aminoethyl)-glycine repeating unit [19]. PNAs represent an attractive tool to selectively modulate gene expression using either antisense [20–22], anti-miRNA [18–20], or antigene [26,27] strategies. The study reported in this paper can be divided into two parts. In the first part, we investigated by chemical-physical methodologies the ability of the synthesized 12-mer PNA to specifically recognize the complementary ON sequence located in the target mRNA. Non-denaturing polyacrylamide gel electrophoresis (PAGE), thermal difference spectra (TDS), circular dichroism (CD), and CD melting studies allowed us to ascertain the topology of the obtained complex, as well as the hybridization efficiency and structural stability. In the second part, we used an immortalized human leukemia T-cell line (Jurkat cells), which stably expresses the CD5 protein at high levels, and peripheral blood mononuclear cells (PBMC) from B-CLL patients to assess the ability of PNA to down-regulate the expression of CD5 as intended. In Jurkat cells, we demonstrated that PNA decreased CD5 expression both at mRNA and protein levels. To determine the consequences of PNA-mediated CD5 down-modulation in a more physiologically relevant setting, we carried out PNA treatment in PBMCs isolated from B-CLL patients. Consistent with results obtained in Jurkat cells, we observed CD5 reduction following PNA treatment. Intriguingly, we observed that PNA co-treatment with fludarabine significantly increases the drug-induced

apoptotic effects, thus highlighting a potential therapeutic application of this approach.

Selection of the target

The CD5 mRNA sequence to be used as the target of our antisense approach was selected as described in the Experimental Section. Since DNA is more nuclease-resistant than RNA [36], to ease the preliminary in vitro hybridization studies, we used the 12-mer DNA sequence having the same sequence of the 12-mer mRNA tract as a model to evaluate the ability of PNA to recognize its target specifically. Next, we synthesized the corresponding 12-mer DNA sequence

Sample	Sequence
PNA	tttctctcccaa-Gly-Ser(P)-Ser(P)-Gly-NH_2 (N→C)
PNA-FITC	FITC$(AEEA)_2$-tttctctcccaa- Gly-Ser(P)-Ser(P)-Gly-NH_2 (N→C)
scrambled PNA	cctattactcct-Gly-Ser(P)-Ser(P)-Gly-NH_2 (N→C)
scrambled PNA-FITC	FITC$(AEEA)_2$-cctattactcct-Gly-Ser(P)-Ser(P)-Gly-NH_2 (N→C)
DNA	TTGGGAGAGAAA (5'→3')
pyrimidine-rich control DNA	CCTCTGGTCTCC (5'→3')
purine-rich control DNA	GGAGACCAGAGG (5'→3')

Lowercase letters indicate PNA bases.

Table 4 ***PNA and DNA molecules used in this study***

specifically(DNA in Table 4) used for the in vitro hybridization studies. The interaction between the target DNA model and its complementary PNA (PNA) or not complementary PNA (scrambled PNA) (Table 4) was assessed using non-denaturing polyacrylamide gel electrophoresis (PAGE), thermal difference

spectra (TDS), circular dichroism (CD), and CD melting, as reported below.

PAGE analysis

The ability of the synthesized PNA to selectively bind the complementary DNA model sequence was first investigated by PAGE analysis (Fig 9). We used the pyrimidine-rich control DNA, purine-rich control DNA, and scrambled PNA sequences as negative controls (Table 2). The PAGE mobility of DNA/PNA and DNA/scrambled PNA mixtures at the 1:3 molar ratio (Fig 9A, lanes 2 and 5, respectively) was compared to that of DNA, PNA, and scrambled PNA alone (Fig 9A, lanes 3, 1, and 4, respectively). DNA and PNA migrated as a single band, with the first having a faster migration rate because of the higher negative charge of the sugar-phosphate backbone. The addition of 3 equiv. of PNA to DNA resulted in the dis- appearance of the band of free DNA and the

appearance of a new intense band corresponding to the DNA/PNA heteroduplex (Fig 12A, lane 2). Conversely, the addition of 3 equiv. of scram- bled PNA to DNA did not cause the disappearance of the free DNA's band nor the appearance of a new band attributable to the DNA/scrambled PNA heteroduplex (Fig 12A, lane 5). Indeed, differently from PNA, scrambled PNA did not migrate as a single band, but as a couple of bands, the first of which has the same mobility as PNA. Though the ESI-MS and HPLC data confirmed the purity and chemical nature of scrambled PNA, it is possible that the presence of minor amounts of incomplete scramble PNA could be responsible for the faster band (Fig 12A, lane 4). The binding selectivity of PNA for the fully complementary DNA sequence was established by the absence of any interaction with the purine-rich control DNA (having the complementary purine to pyrimidine ratio than PNA) and pyrimidine-rich control DNA (having the same pyrimidine to purine ratio than PNA), which were chosen as the negative DNA control sequences, as disclosed by the analysis of the PAGE run reported in Fig 12B.

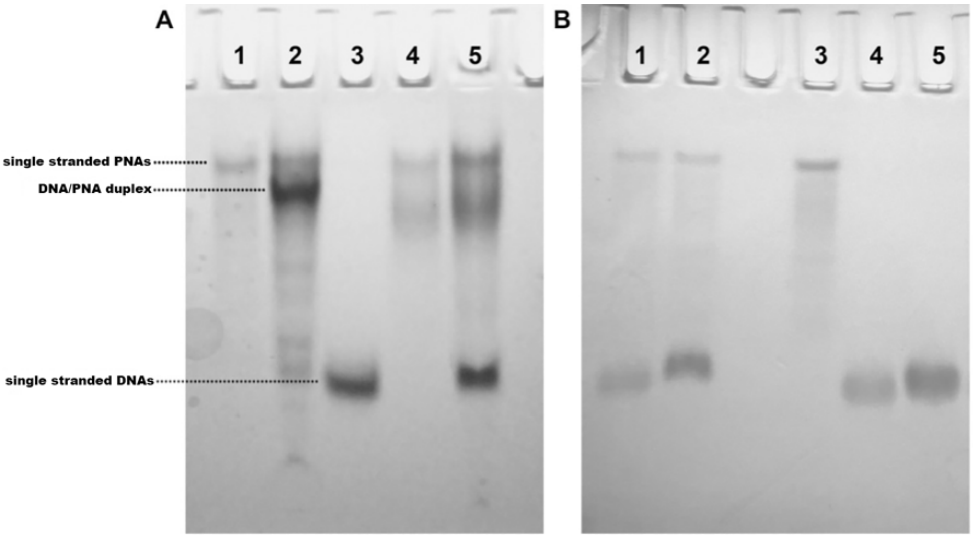

Figure 12. PAGE in 100 mM PBS of: A) ***PNA*** *(lane 1),* ***DNA*** *mixed with* ***PNA*** *(lane 2),* ***DNA*** *(lane 3),* ***scrambled PNA*** *(lane 4), and* ***DNA*** *mixed with* ***scrambled PNA*** *(lane 5); B)* ***pyrimidine-rich control DNA*** *mixed with* ***PNA*** *(lane 1),* ***purine-rich control DNA*** *mixed with* ***PNA*** *(lane 2),* ***PNA*** *(lane 3),* ***pyrimidine-rich control DNA*** *(lane 4), and* ***purine-rich control DNA*** *(lane 5). All mixtures were prepared at a 1:3 DNA/PNA ratio.*

CD, CD melting and TDS experiments

To confirm the formation of the DNA/PNA heteroduplex, we recorded the CD profiles of the DNA/PNA and DNA/scrambled PNA mixtures (1:3 molar ratio) (dashed lines in Fig 13, panel A and B, respectively) in comparison with the CD spectra of DNA (solid black lines), PNA (dotted line, panel A) and scrambled PNA (dotted line, panel B) alone. The **DNA/PNA** spectrum showed the characteristic CD profile of an antiparallel DNA/PNA heteroduplex, characterized by two positive Cotton's effects around 220 nm and 260 nm and two negative Cotton's effects around 200 and 240 nm [19]. Conversely, the absence of the typical CD heteroduplex profile and the complete overlapping of the experimental CD spectrum of DNA/scrambled PNA with the arithmetic sum of the individual spectral components (red line) confirmed that the DNA probe does not bind the not-complementary scrambled PNA. The analysis of the CD profile of the DNA/PNA complex showed a higher value of CD absorbance than the arithmetic sum of two components (red line, Fig 10 panel A). We attributed this finding to the formation of stacking interactions between different planes of the DNA/PNA heteroduplex. The binding interaction was further confirmed by the 6 nm blue shift observed for the longer wave- length positive CD maximum, centered at 265 nm rather than at 271 nm (Fig 10, panel C). To investigate the thermal stability of the DNA/PNA heteroduplex, we performed a CD melting study. The resulting melting temperature (Tm) was found to be 37℃. This data supported the suitability of the herein proposed PNA-based antisense approach at the physiological body temperature, also considering that the Tm of PNA/RNA heteroduplexes is generally higher than that of the corresponding PNA/DNA heteroduplexes. Thermal difference spectroscopy (TDS) provides a simple and reliable technique for identify- ing nucleic acid secondary structures (e.g., duplex, triplex, quadruplex). Mergny et al. reported the TDS profiles of three duplexes having 100%, 50%, and 0% GC base composition . In particular, the 50% GC-duplex was characterized by a positive diagnostic peak at 267 nm. Considering that our DNA/PNA complex (42% GC composition) showed the major positive peak at 267 nm, we attributed its TDS profile to that of a DNA/PNA heteroduplex. On the contrary, no significant peak was found at 267 nm for the DNA/scrambled PNA mixture.

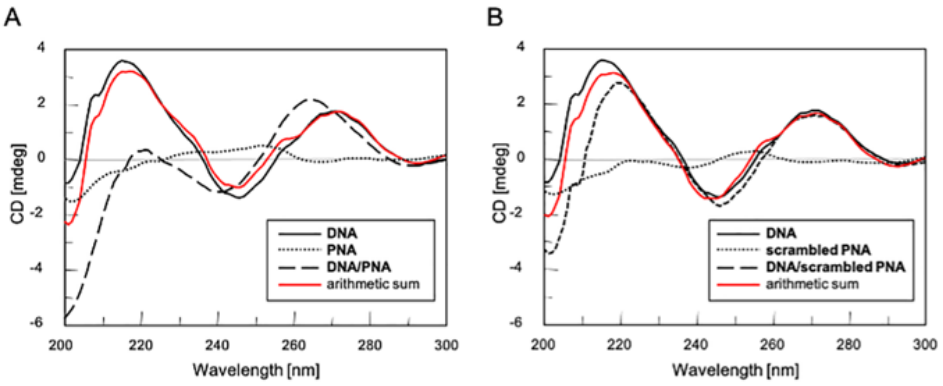

C

Sample	λ max (nm)	λ min (nm)
DNA	215-271	246
DNA/PNA	221-265	200-240
DNA/scrambled PNA	220-271	202-246

Figure 13. CD profile of the single-strand DNA alone (solid black line, panel A and B) and after annealing with PNA or scrambled PNA (dashed line, A and B respectively); samples were dissolved in 100 mM PBS at pH 6.8. The arithmetic sum of DNA and PNA or DNA and scrambled PNA is reported as the red line (panel A and B, respectively). The CD profile of PNA or scrambled PNA alone is reported as the dotted line (panel A and B, respectively). All spectra were acquired at 5°C in the range 200–300 nm and normalized at 300 nm; Table (C) λ values of CD minima and maxima of each sample

Downregulation assessment: RT-PCR, flowcytometry and apoptosis assays.

To examine the cellular delivery of the PNA directed against the CD5 mRNA, we transfected Jurkat cells with different concentrations of the PNA-FITC and scrambled PNA-FITC. The PNA delivery was analyzed by flow cytometry 48 h after transfection. The optimal conditions of PNAs transfection were evaluated by quantifying the background-fluorescence in non- transfected cells used as negative control (NT Jurkat in Fig 14A). As shown in Fig 14 A, the PNA transfection efficiency was measured by evaluating the FL1-A fluorescence corresponding to the uptake of PNA-FITC. The percentage of PNA intracellular delivery was 52.3%, 59.4%, 62.2% and 66.5% at the concentration of 1 μM, 2.5 μM, 5 μM and 10 μM PNA, respectively. No variations in delivery efficiency were observed with scrambled PNA (data not shown). Since a reduction of the total cell number without a notable increase in transfection

efficiency was observed at higher PNA concentrations (5 μM and 10 μM), we chose to use PNA concentrations of 1 μM and 2.5 μM for the subsequent experiments. To assess whether PNA transfection can cause cellular toxicity at the selected doses, we evaluated the cell death of Jurkat cells transfected with 1 μM and 2.5 μM PNA or scrambled PNA 48 h after transfection (Fig 14 B).

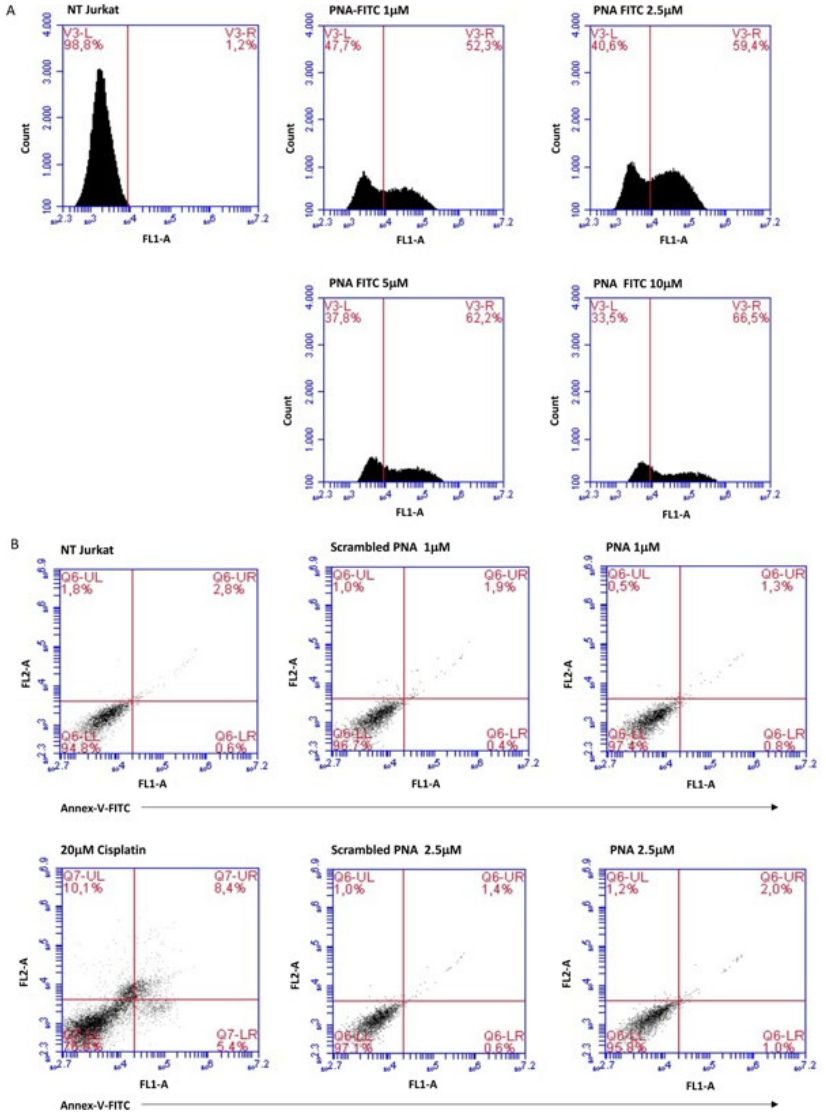

Figure 14. Evaluation of PNA transfection efficiency and cell death analysis in Jurkat cells.

Cells were stained with annexin V and PI and subsequently analyzed using flowcytometry to differentiate between necrosis and early and late apoptosis. The dual negative staining of transfected cells demonstrated that PNA transfection does not affect cell viability. Therefore, no significant side effects were observed in these cells. We next examined the ability of PNA to target CD5 mRNA specifically. To this aim, Jurkat cells were transfected with two different concentrations of PNA or scrambled PNA as negative control and then analyzed for CD5 mRNA expression levels by quantitative reverse transcrip- tion PCR (RT-qPCR). As shown in Fig 15 A, PNA treatment significantly down-regulated CD5 mRNA levels at both concentrations, even though more efficiently at 2.5 μM. Next, we confirmed the reduction of CD5 expression at the protein level by flow cytometry. We initially measured the membrane-bound CD5 levels in Jurkat cells transfected with PNA-FITC and scrambled PNA-FITC. FITC positive cells were gated to assess CD5 expression only in the transfected cells. The percentage of CD5+ cells was found reduced of 16% in cells transfected with PNA-FITC at both PNA concentrations tested, although with no consistent dose-dependent effect (Fig 15, panels B, C). To better elucidate the effect of PNA treatment on CD5 protein levels in Jurkat cells, we then separately evaluated membrane-bound and intracellular CD5 expression levels. In this case, cells were transfected with the higher PNA dose (2.5 μM) according to the more dramatic reduction in mRNA levels detected at this concentration (Fig 15A). Positive cell percentages for membrane or intracellular CD5 proteins are shown in Fig 15D and 15E.

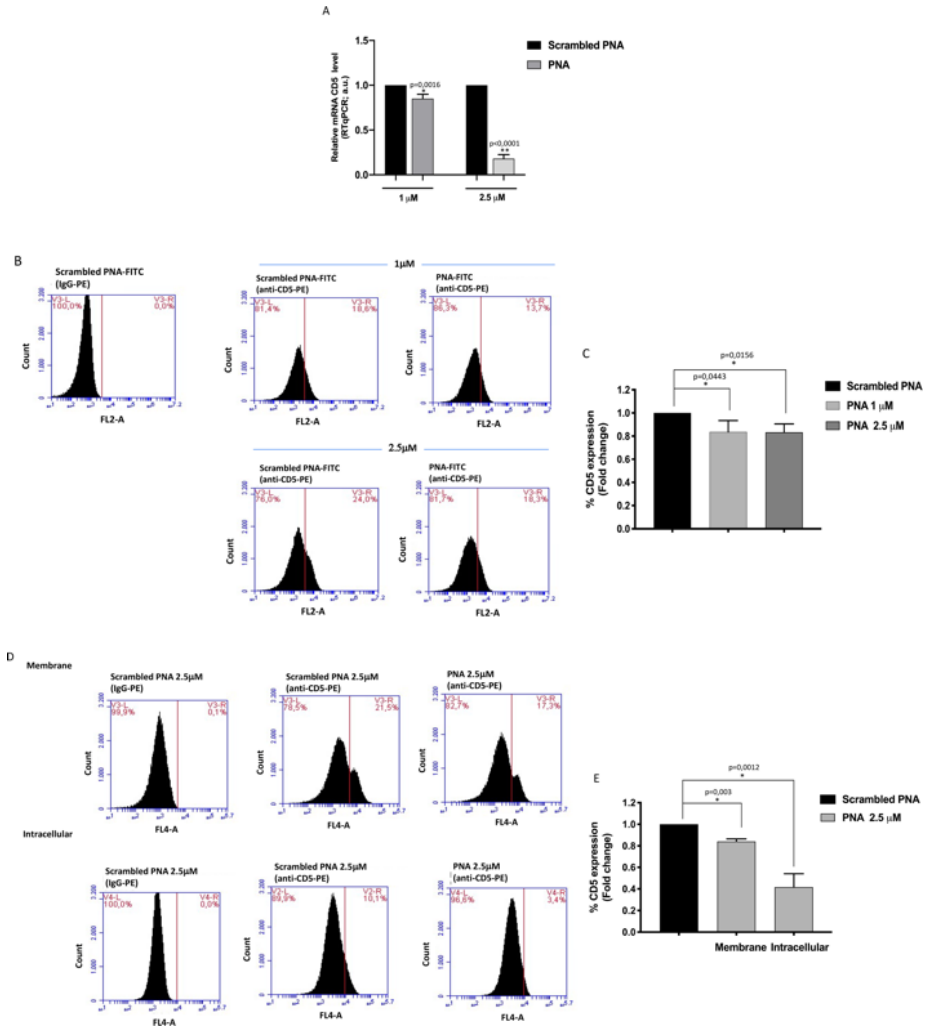

Figure 15 Evaluation of PNA effect on CD5 expression.

Results indicate a more significant reduction in intracellular CD5 expression (59%) with respect to the membrane fraction (16%) following PNA transfection. We speculate that the stronger reduction of intracellular CD5 in comparison to membrane-bound CD5 can be related to the slow turnover rate of surface CD5 protein. Nevertheless, a reduction of about 75% in the total CD5 protein expression (membrane plus intracellular fractions) was found following PNA treatment (see Fig 15E). Our results prove that the negative regulatory effects of the PNA treatment are directly related to impaired CD5 mRNA function and, consequently, to reduced

protein levels. PBMCs purified from peripheral blood of B-CLL patients were characterized for the presence of CD5+CD19+ B-cells, typically enriched in B-CLL patients (Fig 16, panel A). Given the limited amount of PBMC recovery from each patient, each cell sample was sufficient for only one or at most two different experiments. Since the 1 μM PNA concentration had resulted effective in substantially reducing CD5 mRNA levels (Fig 16, panel C), we used this lower effective dose in primary PBMCs. Firstly, we evaluated membrane-bound CD5 protein levels in PBMC cells transfected with PNA or scrambled PNA by flow cytometry. Results showed that PNA specifically downmodulates cell membrane-CD5 levels in B-CLL patients (Fig 16, panel B). In detail, in PBMC from two B-CLL patients (P1 and P2) we observed an average reduction of about 25% of membrane-bound CD5 protein levels following PNA treatment with respect to cells treated with scrambled PNA. Furthermore, we observed that CD5 mRNA levels were decreased of 77% in B-CLL PBMCs compared to the scrambled control (Fig 16, panel C). To examine if CD5 down- modulation can enhance sensitivity to chemotherapy, CLL PBMCs from patients P3 and P4 transfected with PNA or scrambled PNA were treated with the chemotherapic drug fludarabine. Then apoptosis was evaluated by annexin V/PI assay (Fig 16, panel D). Consistent with results in Jurkat cells, PNA alone does not induce cell death whereas, interestingly, in combination with fludarabine, PNA treatment significantly increased the percentage of apo- ptotic cells (22.5% in P3 and 13% in P4), also supporting the physiological significance of PNA-dependent CD5 down-modulation in CLL. Collectively, these results show that PNA treatment reduces CD5 mRNA and protein levels in PBMCs from B-CLL patients and sensitizes B-CLL cells to chemotherapy-induced cell death.

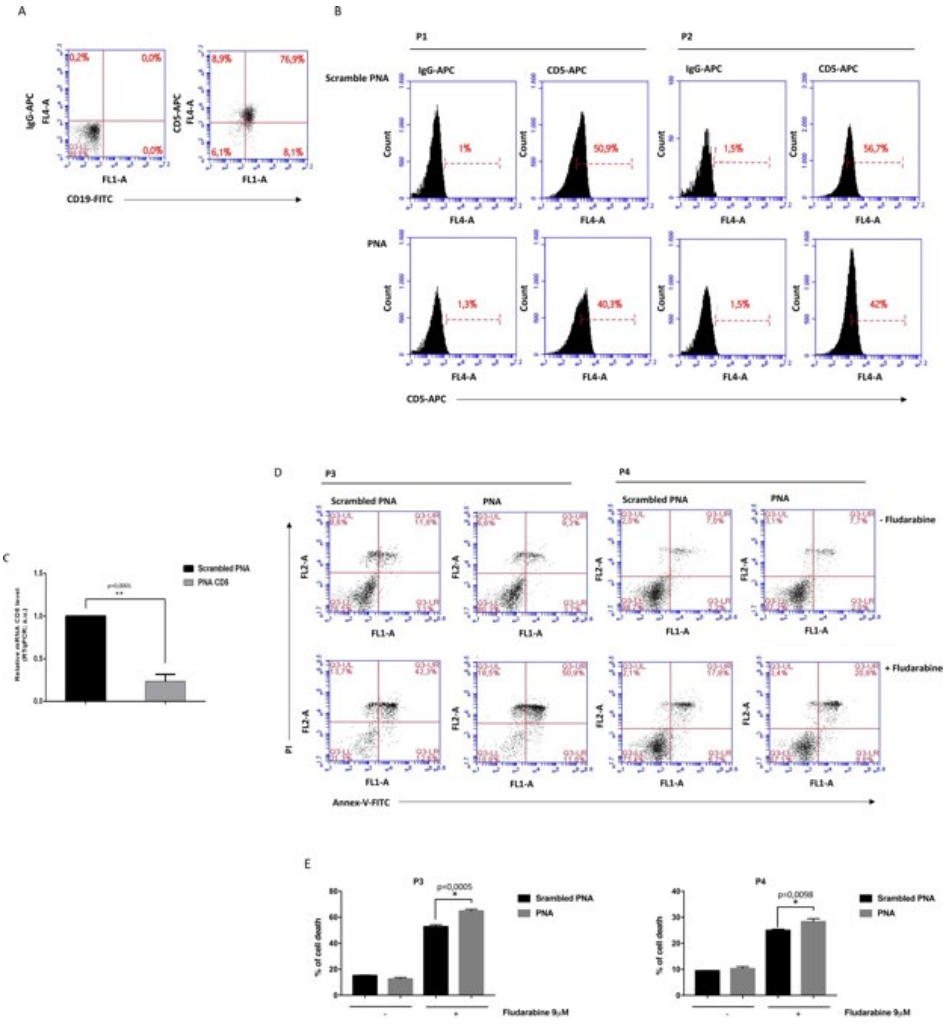

Figure 16. PNA impairs CD5 expression in B-CLL cells and sensitizes to fludarabine-induced cell death.

Experimental section

DNA analysis, synthesis, and characterization

To select and design an efficient antisense PNA targeting the CD5 mRNA sequence (NCBI Reference Sequence: NM_014207.4), we used the OligoWalk algorithm embedded in the RNA structure software (http://rna.urmc.rochester.edu/). The M-fold algorithm(http://rothlab.ucdavis.edu/genhelp/mfold.html) was also

used to predict secondary structures in CD5 mRNA to exclude those sequences that could fall back on not accessible mRNA regions. Among all the selected 12-mer putative targets on the CD5 mRNA, we chose a tract with a high purine base content, starting 1050 nt from ATG, because of the higher synthetic yield of pyrimidine-rich PNA strands. The synthesis, purification, and desalting of the corresponding DNA strand (DNA, Table 4) were performed by standard following the protocol reported elsewhere [27]. The ON concentration was determined using a Jasco (Easton, MD, USA) V-530 UV spectrophotometer at 260 nm and 90℃, using the molar extinction coeffi- cient ε = 131.6 cm–1 mM–1, calculated with the Sigma-Aldrich OligoEvaluatorTM web tool (www.oligoevaluator.com). The structure of DNA, dissolved in ammonium acetate buffer and methanol (1:1, v/v) at the final concentration of 2 μM, was confirmed by ESI-MS (S1 Fig). The 12-mer purine-rich control DNA and pyrimidine-rich control DNA sequences (Table 2) were synthesized and purified as previously described.

PNA synthesis and characterization

Specific CD5 PNA (PNA) and a scrambled PNA (Table 1) used as non-specific negative con- trol were synthesized using the 9-fluorenylmethoxycarbonyl (Fmoc) solid-phase strategy and purified following the protocol reported elsewhere [28]. To promote the PNAs delivery across the cellular membranes, we used Lipofectamine 2000 (Invitrogen, Carlsbad, CA) as a transfection reagent. The cationic head group of lipofectamine governs the interaction between lipids and PNAs. Due to the absence of charges in the PNA backbone, it was necessary to introduce two negative charges on the PNA oligo- mers by adding two serine-phosphate monomers at the C-end of the PNA chains. For this pur- pose, we used two Fmoc-Gly-OH and two Fmoc-L-Ser [PO(OBzl) OH]-OH residues in the first four couplings of the solid-phase strategy. To evaluate PNAs' transfection efficiency and select the transfected cells, we labeled the PNAs' N-terminus with the fluorescein isothiocya- nate (FITC) fluorophore, thus obtaining the corresponding PNA-FITC and scrambled PNA-FITC (Table 1). After purification by RP-HPLC, all the PNA products were character- ized by ESI-MS. The amount of all PNA samples, dissolved in pure water, was esti- mated by a Jasco V-530 UV spectrophotometer at 260 nm and 90℃, using the molar extinction coefficient ε = 104.4 cm–1 mM–1, calculated with

the Sigma-Aldrich OligoEvalua- torTM web tool (www.oligoevaluator.com).

Preparation of samples

All DNA and PNA samples were analyzed in 100 mM phosphate-buffered saline (PBS) at pH = 6.8. For DNA and PNA preparations, 10 nmol of each ON were lyophilized and dis- solved in 10 μL of 100 mM PBS buffer to obtain 1 mM stock solutions. DNA/PNA mixtures were prepared at the 1:3 ratio by mixing 10 nmol of lyophilized DNA with 30 μL of 1 mM PNA stock solution in water. Sample solutions were dried and re-dissolved in 10 μL of PBS to have 1 mM solutions. Finally, solutions were heated at 90 ℃ for 10 min, equilibrated at 4 ℃ overnight, and used for PAGE analysis. For CD studies, 7 μL of each sample were diluted to 400 μL with 100 mM PBS buffer to obtain a 17.5 μM concentration. These solutions were fur- ther diluted to 3.5 μM for TDS investigations. Finally, a 50 μM solution of DNA/PNA mixture was used for CD melting measurement.

Non-denaturating Polyacrylamide Gel Electrophoresis (PAGE)

Polyacrylamide gel was prepared at 18% of acrylamide/bis-acrylamide solution. 1 × Tris- Borate-EDTA (TBE) buffer supplemented with 30 mM KCl at pH 7.0 was employed for the gel run. Samples were loaded at 1 mM concentration. 3 μL of each sample was added to 7 μL of loading buffer (glycerol/1 × TBE + 30 mM KCl 1:9) for gel loading. PAGE was carried out at a constant voltage of 120 V at 5 ℃ for about 1 h. The gel was visualized by using a UV-Vis lamp at 254 nm.

Thermal Difference Spectra (TDS)

TDS of DNA/PNA and DNA/scrambled PNA were obtained by the arithmetic difference between UV spectra acquired at 90 ℃ (unfolded) and 5 ℃ (folded). The UV spectra were recorded at a concentration of 3.5 μM of samples on a Jasco V-530 UV spectrophotometer equipped with a Peltier-type temperature control system (model PTC348WI) using the follow- ing settings: range λ = 250–320 nm, 400 nm min–1 scanning speed, 2.0 nm bandwidth, and averaged over three scans using 0.1 cm path-length cuvette.

Circular Dichroism (CD) and CD melting

CD spectra were recorded at 5 ℃ using a Jasco 1500 spectropolarimeter equipped with a Jasco PTC-348-WI temperature

controller unit. The thermal denaturation curve of DNA/PNA mixture was recorded at 265 nm in the temperature range 5–90℃, 1℃ min–1 heating rate.

Peripheral Blood Mononuclear Cells (PBMCs) isolation from CLL patients and drug treatment

Peripheral Blood Mononuclear Cells (PBMCs) were isolated by a Ficoll-PaqueTM density gra- dient (Merck, Darmstadt, Germany) from the peripheral blood of B-CLL untreated patients in the stationary phase of the disease [24]. B-CLL diagnosis was obtained according to clinical and immunophenotypic criteria. Five patients (P1, P2, P3, P4, P5) who had > 75% CD19 + cells co-expressing CD5 (patients P1-P5) were selected. The patients provided appropriate written informed consent. The study was approved by the Ethics Committee of the University of Naples Federico II. PBMCs were maintained in RPMI 1640 (Sigma-Aldrich, Milan, Italy) supplemented with 10% human serum and 20 µL of anti-Human CD3 antibody (10 µg/mL) (eBioscience Thermo Fisher, Inc, Waltham, MA) as previously reported [30,31]. For drug treatment, 24 h after PNA transfection, PBMCs were treated with 9 µM fludarabine (Teva Pharmaceutical Industries Ltd, UK) for 72 h.

Cell cultures and treatment

The human Jurkat cell line was obtained from the Cell Culture Facility, CEINGE (Naples, Italy). Cells were maintained in RPMI 1640 (Sigma) medium supplemented with 10% fetal bovine serum (FBS) (Gibco, Thermo Fisher Scientific Inc, Waltham, MA) at 37℃ in a humidi- fied 5% CO2 atmosphere. As a positive control of cell death, Jurkat cells were treated with 20 µM cisplatin (Accord Healthcare, London, UK) for 24 h.

Transient transfection

For transfection experiments, freeze-dried PNAs were dissolved in RNase-free water and tri- fluoroacetic acid (TFA). Jurkat cells were plated in 12-well plates at a density of 4 × 105 cells/ well and transiently transfected with either 1 µM or 2.5 µM PNA or scrambled PNA as an aspecific negative control, using Lipofectamine 2000 (Invitrogen, Carlsbad, CA) as transfection reagent as previously reported [32].Also, CLL PBMCs were plated in 12-well plates at a density of 1 × 106 cells/well and transiently transfected with 1 µM

PNA or scrambled PNA. 48 h after transfection, Jurkat cells, and CLL PBMCs were collected to evaluate CD5 mRNA and protein levels. The same cells were also used to perform Annexin V/propidium iodide (PI) assays.

Real-time PCR analysis

Total RNA extraction from Jurkat cells and B-CLL PBMCs, reverse transcription, and quanti- tative real-time PCR were performed as previously described[33–35].Primers used to detect the expression of CD5, and HPRT (endogenous control) were: Each real-time PCR was performed in triplicate in a 15 µL reaction mix containing 7.5 µL of 2 × SsoAdvanced Universal SYBR Green supermix (Bio-Rad Laboratories GmbH, Munich, Germany), 0.28 µL of a 20 µM primer mix, 1.5 µL of cDNA, and 5.72 µL of nuclease-free water. The cycling parameters were set up as follows: a denaturation step at 95℃ for 3 min, fol- lowed by 40 cycles (95℃ for 15 s, 60℃ for 30 s) and 80 cycles performed according to stan- dard protocols for melting curve analysis.

Flow cytometric analysis

To evaluate the transfection efficiency, 1 × 105 Jurkat cells were harvested 48 h after transfec- tion with PNA-FITC and scrambled PNA-FITC, washed in PBS, and analyzed with a BD AccuriTM C6 Cytometer (BD Biosciences, San Jose, CA, USA). The study population was identified and gated on the base of its forward and side scatter to exclude debris found at the bottom left corner of the FSC/SSC density plot. Gated events, of the acquired population, were then analyzed for their fluorescence in the FL-1 channel to assess PNA delivery thanks to their labeling to the FITC fluorochrome. Data were expressed in a FL-1 histogram where, in order to accurately identify the positive dataset, non-transfected cells were used to place a vertical bar and determine the background/autofluorescence and to set the negative population, thus allowing the positive cells to be accurately identified and gated for further analysis. Membrane CD5 staining in Jurkat cells was performed using anti-CD5-phycoerythrin (PE)-conjugated (ImmunoTools, Friesoythe, Germany) at a concentration of 0.05 µg/mL. Instead, the intracellular CD5 expression was measured on Jurkat cells fixed with 1% paraformaldehyde in PBS 1× for 20 min and permeabilized with 0.5% Triton X-100. Cells were then incubated with the specific anti-CD5 antibody PE-conjugated. B-CLL

PBMCs were identified using an FSC/SSC dual parameter dot plot and characterized for the expression of CD19 and CD5. The measure of membrane CD5 and CD19 was performed using an anti-CD5 Allophycocyanin (APC)-conjugated and anti-CD19 (FITC)-conjugated (ImmunoTools), at a concentration of 0.05 µg/mL. Human Fc block (2.5 µg/106 cells) (Pharmingen BD, San Diego, CA, USA) was used to minimize the non-specific binding of immunoglobulins to Fc receptors before the flow cytometric staining. Control IgG isotypes conjugated with each used fluorochrome, IgG-PE/FITC (Santa Cruz Biotechnology, Santa Cruz, CA, USA), or APC-con- jugated (Pharmingen BD) were used in each staining to assess the non-specific binding. Each staining was performed by incubating cells with the antibodies mentioned above for 30 min in the dark at 4℃. Cells were then washed and analyzed by flow cytometry. Cell death analysis was conducted by double-staining with Annexin-V (FITC-conjugated, Immunotools) and Propidium iodide (PI) (Merck Millipore, Milan, Italy). Briefly, the cells were harvested, washed in PBS, and incubated in 100 µL of binding buffer (10 µM Hepes/NaOH pH 7.5, 140 µM NaCl, and 2.5 µM CaCl2) containing 1 µL of Annexin-V-FITC (Pharmingen BD) for 15 min in the dark. Then, 100 µL of the same buffer was added to each sample and analyzed by flow cytometry.

Statistical analysis

When appropriate, T-test and one-way analysis of variance procedure followed by Dunnett's multiple comparison test were used to calculate statistical significance. Differences were con- sidered significant when $p \leq 0.05$ (*) or highly significant when $p \leq 0.0001$ (**).

Conclusion

Recently, CD5 has been proposed as a promising therapeutic target in CLL. Given the severity of the disease and the importance of the newly emerged roles of CD5, great efforts are being made to develop novel therapeutic approaches to inhibit the oncogenic potential of the aberrant CD5 signaling. The downregulation of transmembrane protein overexpressed by B cell in CLL is the preferential antitumoral strategy used. The control of protein expression is mostly gained by monoclonal antobody administration.Yoshikane Kikushige et al. In a paper review reports the state of the art about development of novel treatment strategy anti B-CLL (DOI: 10.3960/jslrt.20036). PNAs are oligonucleotides analogs characterized by high resistance to nucleases and proteases, excellent chemical and biological stability and high hybridization affinity and sequence specificity toward DNA and RNA. Many studies have recently addressed the therapeutic potential of PNAs in gene modulation in several disease models. In this paper, we synthesized a suitable PNA molecule to investigate its ability to bind the target sequence on the CD5 mRNA, and effectively down-modulate CD5 expression in CLL. Functional studies in a human leukemic cell line showed reduced membrane-bound and intracellular CD5 protein levels following PNA delivery and CD5 mRNA targeting without significant cell toxicity. Based on the high PNA/DNA complex's stability evaluated in this study, it is expected that this PNA molecule is able to hybridize with higher affinity to its mRNA target, thus further reinforcing the relevance of our functional results. Impairing CD5 mRNA function through this approach thus represents an effective potential therapeutic tool to down-modulate the BCR pro-survival pathways triggered by CD5 in CLL. In addition, the unique features of the prolonged intracellular half-life of PNA offer a great advantage in terms of stable long-term modulation of CD5 expression levels compared either with other antisense approaches or traditional antibody-based therapies. In conclusion, our results pave the way to further studies to evaluate CD5 PNA treatment's feasibility in combination with chemotherapy as an appealing approach for more effective therapeutic strategies in CLL

Objective 2 Development of surface chemical strategies for synthesising redox-responsive diatomite nanoparticles as a green platform for on-demand intracellular release of an antisense peptide nucleic acid anticancer agent (Publication n°5)

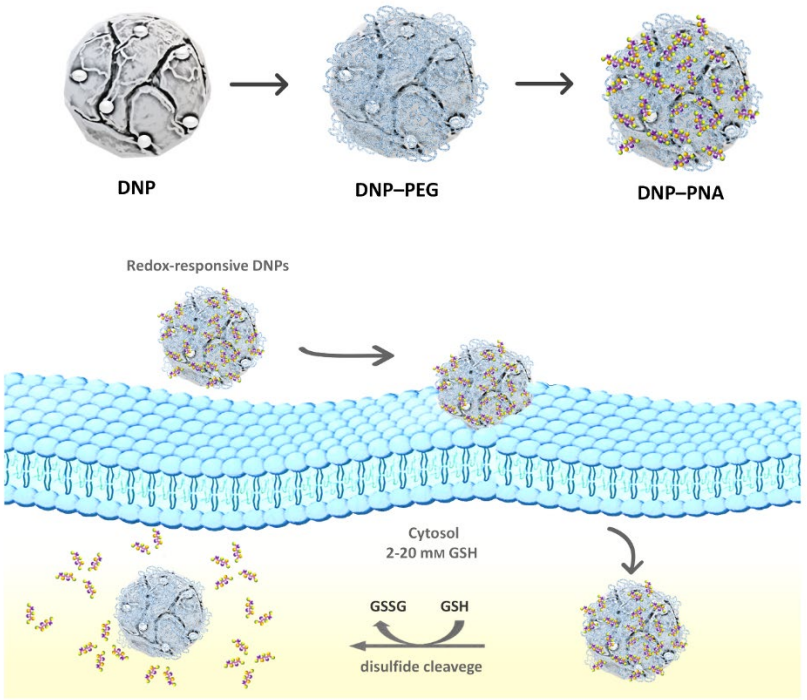

Scheme 1 Schematic diagram of redox-responsive DNP–PNA (where DNP is diatomite nanoparticles, PNA is peptide nucleic acid) synthesis and internalization in cancer cell. The high glutathione (GSH) concentration in cancer cells induces the cleavage of disulfide bonds between the NPs and the PNA, promoting a controlled intracellular drug delivery

The effectiveness of diatomite NPs (DNPs) to deliver different small molecules by endocytic uptake and their accumulation mainly in the cytoplasmic region of cancer cells makes these systems suitable for antisense PNA transport for cancer treatment.[51–55] PNA is a neutral charged artificial oligonucleotide mimetic molecule remarkably similar to DNA and RNA in intramolecular spacing and geometry.56 PNA shows unique and improved properties compared to conventional oligonucleotides, including resistance to enzymatic digestion, higher stability combined with excellent hybridization

affinity toward DNA and RNA, making it an attractive molecule for a wide range of biomedical applications.[57–59] Although PNAs act as effective antisense or antigene agents for inhibition of transcription or translation of target genes, their poor intracellular uptake still limits their therapeutic use. Therefore, there is a need to find valuable methods to enhance the access of PNAs into intracellular space, to increase the success of a PNA-based therapy. [60–63]

For this purpose, we developed an easy one-pot redox-responsive functionalization strategy to engineer DNPs for controlled antisense PNA intracellular delivery aiming to inhibit the immune checkpoint programmed cell death 1 receptor/ programmed cell death receptor ligand 1 (PD-1/PD-L1) in cancer cells. PD1/PD-L1-mediated immune checkpoint is an important component of the immune escape mechanism used by tumor cells against the host immune system.[64] The activation of the PD1/PD-L1 signaling pathway is the mechanism by which tumors escape the recognition and killing by antigen-specific T cells, promoting tumor cell survival and metastasis. Clinical data demonstrated that the blockade of PD-1 signaling significantly enhanced antitumor immunity, producing durable clinical responses and prolonging patients' survival.[65–67]

The DNPs were bioengineered with a polyethylene glycol (PEG) shell acting as gatekeeper for the controlled drug release, where the PEG and PNA were connected via a disulfide bond (S–S), cleavable upon exposure to a reducing environment.[68] Polymers are extensively used in the development of drug delivery systems to improve stability, biocompatibility, circulation half-time, and reduce adsorption of blood proteins, delaying the reticuloendothelial system's action (RES).[69–71] We explored different reaction conditions to obtain DNPs with the highest surface PEG functionalization yield and evaluated them by qualitative and quantitative techniques, such as 1D solution-phase proton nucleic magnetic resonance (NMR), colorimetric assays, dynamic light scattering (DLS), transmission electron spectroscopy (TEM) and spectrophotometric analyses. The best NPs formulation was used for studies of PNA-conjugation, redox-triggered release, hemocompatibility, cells toxicity, cellular uptake, as well as activity on MD-MBA 231 triple negative breast cancer cells, A549 lung cancer and U87 glioblastoma cells chosen for their high expression of PD-L1. A proper surface chemical functionalization of nanomaterials is paramount, especially for targeted drug delivery applications. The NPs' surface is frequently functionalized to

improve their physicochemical properties, enrich their functionalities and affect their behaviour in biological systems.[72–74] Therefore, the precise quantification of available surface functional groups on the NPs' surface is fundamental to adequately control the surface chemical processes. To synthesize the redox-responsive DNPs with the highest surface functionalization yield, we explored different chemical conditions evaluating qualitatively and quantitatively the available functional groups by 1D solution-phase proton nuclear magnetic resonance (NMR), colorimetric assays and dynamic light scattering (DLS).The first chemical approach was based on a conventional multi-step procedure that introduces the desired reactive groups or functional moieties through independent and consecutive chemical reactions until obtaining the desired NPs. The bare NPs (DNPs–OH) were obtained by mechanical crushing, sonication, and acid purification of raw diatomaceous earth powder (see Materials and Methods, Supporting Information). The DNPs–OH were silanized by the chemical reaction between the triethoxy groups of aminopropyltriethoxysilane (APTES) and the −OH groups on the silica surface, thus introducing –NH2 groups needed for the covalent conjugation with the redox gatekeeper PEG molecules (5000 Da). The molecular weight of PEG molecules used for NPs PEGylation is fundamental to confer properties suitable for drug delivery applications. It was previously demonstrated the silica NPs with PEG 5000 Da coating have higher aqueous solution stability than PEG 2000-500 Da coating; PEG with high molecular weight (MW) has longer side chains than PEG with low MW, so it functions more effectively as a steric stabilizer and prevents adsorption of plasmatic proteins.[75] The 1H NMR spectrum of APTES-modified DNPs solution in Figure 14A show the characteristic peaks of the protons of the aminopropyl chain from 0.60 to 2.90 ppm (peak a, b, c) and the absence of protons of ethoxy groups at 3.80 and 1.18 ppm, confirming the complete grafting of the APTES to NPs' surface.[76]Then, we determined the number of APTES molecules onto NPs' surface by quantitative NMR (qNMR). We quantified the DNPs silanization with the integration of the peaks area of 1H spectrum of the NPs solution by the internal standard fumaric acid and calculated 5.2 ± 0.5 μmol mg-1 of grafted APTES according to Equations 1 and 2. Subsequently, we used the ninhydrin assay for both qualitative and quantitative determination of the free –NH2. The reaction of primary amines on DNPs with ninhydrin generates a colored product known as Ruhemann's purple measurable

desposabe amine groups to be functionalized in the next step of the reaction. The amount of accessible –NH2 on DNPs' surface estimated by the analysis of the NPs supernatant resulting from ninhydrin assay, was 0.20 ± 0.06 µmol mg-1. The PEGylation of the DNPs–NH2 by the (N-Hydroxysuccinimide) NHS esters of the heterobifunctional PEG molecules with the amine groups of the NPs at different conditions. The 1H NMR spectrum of PEGylated DNPs shows a very weak signal of the large backbone (OCH2CH2)44 from 3.6-3.7 ppm, suggesting a low functionalization yield for both conditions, as confirmed by the qNMR analysis (0.002-0.005 µmol mg-1, corresponding to 1-2.5 %, Figure 17C).

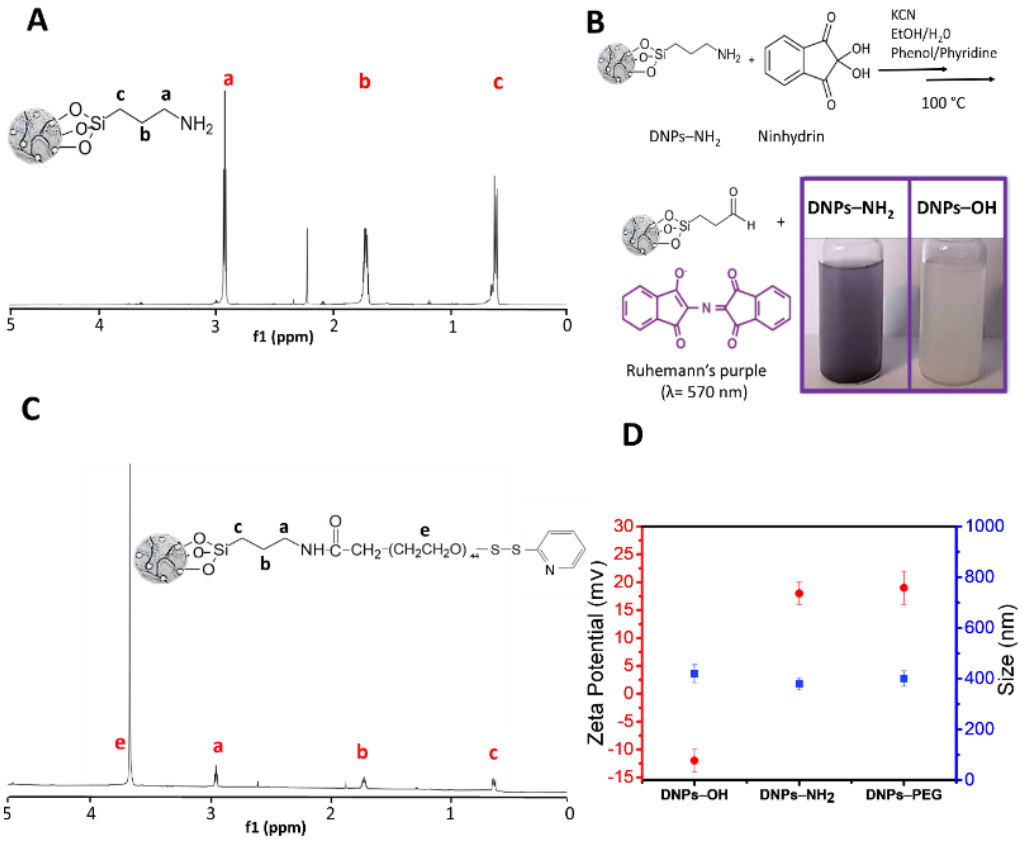

Figure 17 A) [1]H nuclear magnetic resonance (NMR) spectrum of aminopropyltriethoxysilane (APTES) modified diatomite nanoparticles (DNPs) (DNPs–NH2) colloidal solution. B) Reaction of ninhydrin with aminated silica (DNPs–NH2) followed

by generation of Ruhemann's purple colored product. The reaction of the bare NPs (DNPs–OH) with ninhydrin does not lead to any colored product. C) ^{1}H NMR spectrum of PEG-modified DNPs (DNPs–PEG) colloidal solution. D) DNPs zeta potential and size before and after multistep functionalization determined by dynamic light scattering (DLS).

One-pot chemical strategy for the development of redox-responsive nanosystems

Therefore, we developed an easy direct wet chemistry based on a one-pot strategy, allowing to silanize and PEGylate the DNPs' surface as one step to prevent the loss of functional amine groups. This strategy consists in first synthesizing a complex of APTES–PEG, then used to directly functionalize the NPs avoiding intermediate purification steps that could mainly impact on functionalization yield.

We characterized the complex formation over time (up to 24 h) by 1H NMR and compared the obtained spectrum with free APTES one, paying attention to the 2.6-0.0 ppm region where occurring mainly proton signals change. We observed a change in signals of the aminopropyl chain protons of the aminosilane due to the formation of an amide bond between the –NH2 of APTES and the activated –COOH of PEG, confirmed by the disappearance of signal a at 2.6 ppm, and the shift of b from 1.47 to 1.58 ppm. It is important to note the presence of the ethoxy group protons at 1.2 (e), validating that this chemical strategy preserves the APTES from hydrolysis, allowing then the silanization of the NPs.

Subsequently, we functionalized the DNPs with the synthesized complex and evaluated the yield of reaction by qualitative and quantitative analyses. In Figure 18, 1H NMR spectrum of PEGylated DNPs showed an intense signal of protons of the large PEG backbone (OCH2CH2)44 from 3.7-3.9 ppm proving the successful NPs PEGylation, as confirmed by the qNMR analysis (6.5 ± 1 μmol mg-1, ~80%).

We estimated the number of available thiol groups (–SH) on PEG-modified DNPs' surface (DNPs–PEG) by colorimetric assay (ThermoFisher®), after their treatment with dithiothreitol (DTT) reducing aqueous solution (20 mm) to deprotect thiols from orthopyridyl disulfide (OPSS) groups. In this assay, thiols reduce a disulfide-inhibited derivative of papain (papain–SSCH3), releasing the active enzyme (papain–SH). The enzyme cleaves the chromogenic papain substrate (L-BANPA) with the release of yellow nitroaniline chromophore (Amax= 405 nm) whose color intensity is

directly proportional to the content of accessible thiols. We used L-cysteine at different concentration to create a standard curve and quantified 0.615 ± 0.065 µmol mg-1 of –SH available onto NPs' surface for PNAs conjugation. Subsequently, we evaluated the changes occurring in the NPs morphology after the one-pot modification by transmission electron microscopy (TEM) imaging (Figure 18B). The analysis showed the typical irregular shape and porous morphology (10 nm < pores diameter < 50 nm) of the DNPs (bare DNPs), highlighting a dense polymeric layer onto NPs' external surface and inside the pores due to the chemical modification (DNPs–PEG).12 We further confirmed the success of the NPs' functionalization by DLS analysis, resulting in an increase of the particles' size from 420 ± 70 to 480 ± 85 nm and a change of surface charge from -12 ± 2 mV to 20 ± 5 mV (Figure 18C).

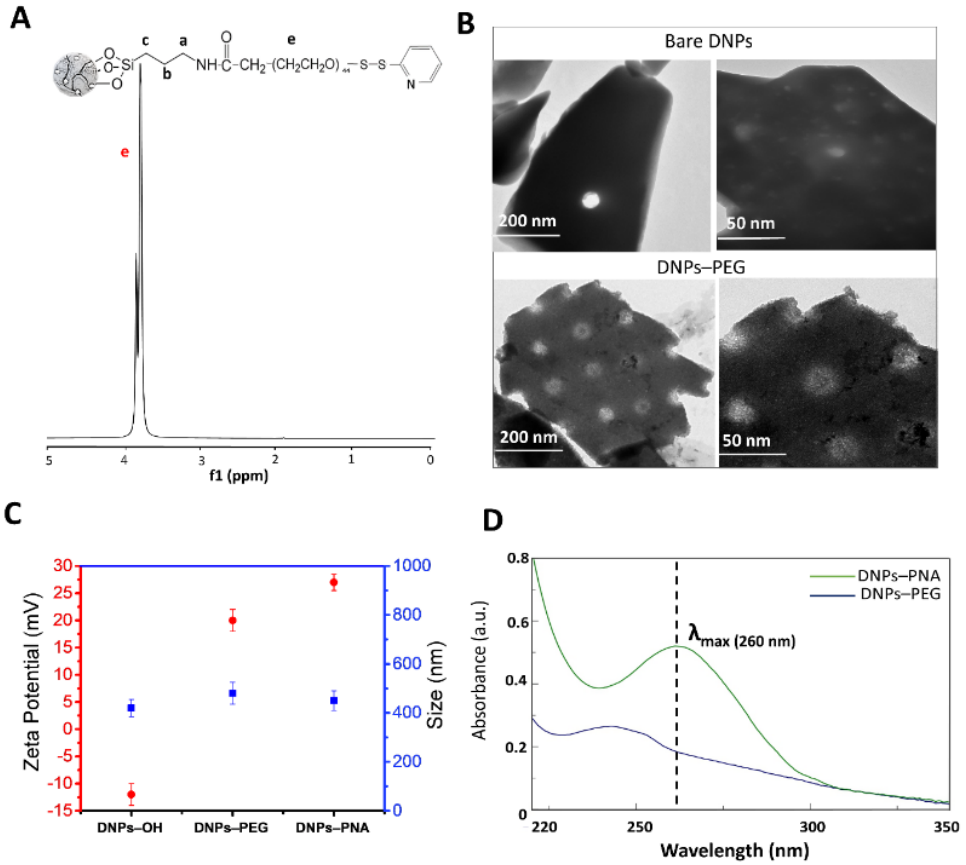

Figure 18 A) [1]H nuclear magnetic resonance (NMR) spectrum of one-pot functionalized diatomite nanoparticles (DNPs) (DNPs–PEG) solution. B) Transmission electron spectroscopy (TEM) images of bare DNPs and DNPs–PEG and increasing zoom of NPs'

surface, respectively. C) DNPs zeta potential and size before and after one-pot functionalization and peptide nucleic acid (PNA) conjugation determined by dynamic light scattering (DLS) at RT. D) UV–visible (UV–vis) spectrum of DNPs before (DNPs–PEG) and after the bioconjugation (DNPs–PNA).

PNAs synthesis and conjugation to redox-responsive DNPs

To develop an effective antisense PNA to inhibit the PD-L1 expression, we used computational tools to select the specific mRNA region to target (NCBI Reference Sequence: NM_014143.4).The synthetized PNAs were covalently bound onto the NPs' surface by disulfide (S–S) bond formation due to exchange reaction among the sulfhydryl (–SH) side chains of the cysteine (Cys) residues of the PNAs and the OPSS of PEG-modified DNPs, respectively. Since having the thiols in a reduced form is mandatory for the success of the reaction, the PNAs were treated with an excess of reducing DTT prior the DNPs conjugation.[77] The NMR analysis of the DNPs–PNA showed very weak signals of amino protons of nucleobases (A, T, C) and aromatic amide protons of the PNA backbone (9.0-5.0 ppm); methyl protons of the A, T, C and the methylene protons of the PNA backbone (4-1 ppm), confirming the success of the bioconjugation. After the PNA conjugation, the size of the DNPs did not change, contrarily to their surface charge which increased to 27 ± 3 mV due to the positive poly-lysine (poly-Lys) chain of the PNA (Figure 18C). Furthermore, we confirmed the successful PNA-conjugation onto the NPs surface by absorbance spectroscopy due to the appearance of an absorbance maximum at 260 nm, typical of the PNA, in the UV–vis spectrum of DNPs (DNPs–PEG) after the conjugation with the PNA (DNPs–PNA) (Figure 18D). TEM analysis showed no changes in the nanosystems morphology after bioconjugation with the PNA; however, this result confirmed that the NPs exposure to the chemicals and procedures used in the biofunctionalization did not alter the chemical coating of the nanosystems.

Drug loading and release studies

The reducing environment of tumours serves as an internal signal for the precise release of loaded drugs from redox-responsive nanocarriers.[79] Since the disulfide bond onto modified-NPs acts as redox-responsive linkage, we used this feature to release the bonded fluorescein isothiocyanate (FITC)-labelled PNA molecules from the NPs surface and quantify it. The amount of PNA-loaded in

the DNPs (i.e., the loading capacity) was determined by fluorescence analyses of the NPs supernatant after 48 h treatment with high DTT (20 mm) concentration. The loading capacity of the DNPs was 0.0485 ± 0.004 μmol mg−1 (corresponding to ~48% and 306 ± 25 μg PNA mg−1DNPs). Furthermore, when the particles were exposed to an excess of DTT (100 mm), no PNAs were further released.

To investigate the release behaviour of the redox-responsive nanosystems, we performed an in vitro release test under physiological conditions (PBS, pH 7.4), and in conditions mimicking the reducing tumour environment (PBS, DTT 20 mm, pH 5.5). The tumour environment is highly reducing and hypoxic, with the intracellular GSH concentration at least four-fold higher than normal cells. This significant difference in the concentration of GSH between the healthy and tumour cells is relevant for the redox-triggered release into a specific site.[45]Figure 19A shows a complete release of PNA (~98%, calculated with Equation 3 and 4), with a plateau at 24 h, only for the DNPs treated with the reducing agent DTT (DNPs–PNA), contrarily, there was not much release (~4%), in the absence of the DTT (CTR). Moreover, we also investigated the release behaviour of the NPs in PBS at pH 5.5 mimicking the acid tumor environment and a PNA release comparable to the CTR was observed (data not shown). The obtained results confirmed that the disulfide bond cleavage controls the PNA release from the developed nanosystems and allows on-demand drug release at the tumour site.

Hemocompatibility study

Hemocompatibility should be one of the foremost concerns in the design and development of NPs for therapeutic applications.

The hemolytic activity of the DNPs–PNA was based on the quantification of percentage (%) of lysed RBCs after their exposure to the NPs at increasing incubation times (1, 4, 24, and 48 h) and concentrations (25, 50, 100, and 200 μg mL-1). We characterized the released hemoglobin spectrometrically at 577 nm and quantified the %-hemolysis with Equation 5 (see Materials and Methods, Supporting Information). The % of lysed RBCs after 48 h of incubation at the maximum concentration of modified-DNPs (200 μg mL-1) was 5 ± 2 % for the DNPs–PNA, confirming the hemocompability of the developed redox-responsive nanosystems

and their potential application for drug delivery applications. As control, the hemolytic activity of the free PNA molecules (0.01 μmol) is 30 ± 5 % and 8 ± 2.5 % for the DNP–PEG (200 μg mL-1), demonstrating that the bioconjugation onto NPs' surface reduces the PNA hemotoxicity as well as improves the hemocompatibility of the PEGylated DNPs (Figure 19B).[49]
We ascribed the hemotoxicity of the free PNA to the thiol (–SH) of the Cys used to modify the molecule for the disulfide (S–S) bond formation with the DNPs–PEG. The hemotoxicity tested of the Cys alone (0.01 μmol) resulted much lower (2.5 ± 0.5 %) than when bound to PNA because of the free carboxylic group (–COOH), which may lead to repulsion with negative charged RBCs' membrane avoiding a possible thiol interaction with them. In the bonded Cys–PNA, the –COOH is involved in peptide bond with Lys chain (used to give a positive charge to PNA for improving solubility) and lacking the repulsive force, the thiol freely interacts with the membrane of the RBCs and activates mechanisms that lead to the cells hemolysis.[81-82] Finally, we also tested the hemotoxicity of a Lys chain-PNA sequence without Cys, resulting in blood compatibility.

Cell viability studies

Although nanostructured silica from diatoms has been recently introduced in nanomedicine, to date, there are numerous in vitro and in vivo studies that demonstrated the biocompatibility and the safety of this emerging material.10 The ATP intracellular content, as an indicator of the physiological state of cells, was used for determining the viability of MD-MBA 231 triple-negative breast cancer cells and A549 lung cancer cells exposed to different DNPs and PNA concentrations (up to 200 μg mL-1 and 0.01 μmol, respectively) up to 72 h of incubation time. The physiological state of the cells incubated with the samples was compared with the negative control, represented by cells incubated with complete medium (10 % FBS RPMI or DMEM, respectively). The modified-DNPs (DNPs–PNA) did not reduce cells viability on both cell lines, even at high concentrations and longer incubation times, confirming the safety of the DNPs for PNA delivery (Figure 19C and D).
As control, the cytotoxicity of the PEGylated DNPs (up to 200 μg mL-1) and free PNAs (up to 0.01 μmol) after 72 h was evaluated. The results confirmed the biocompatibility of the PEGylated NPs due to PEG coating, which positively affects the cells viability.

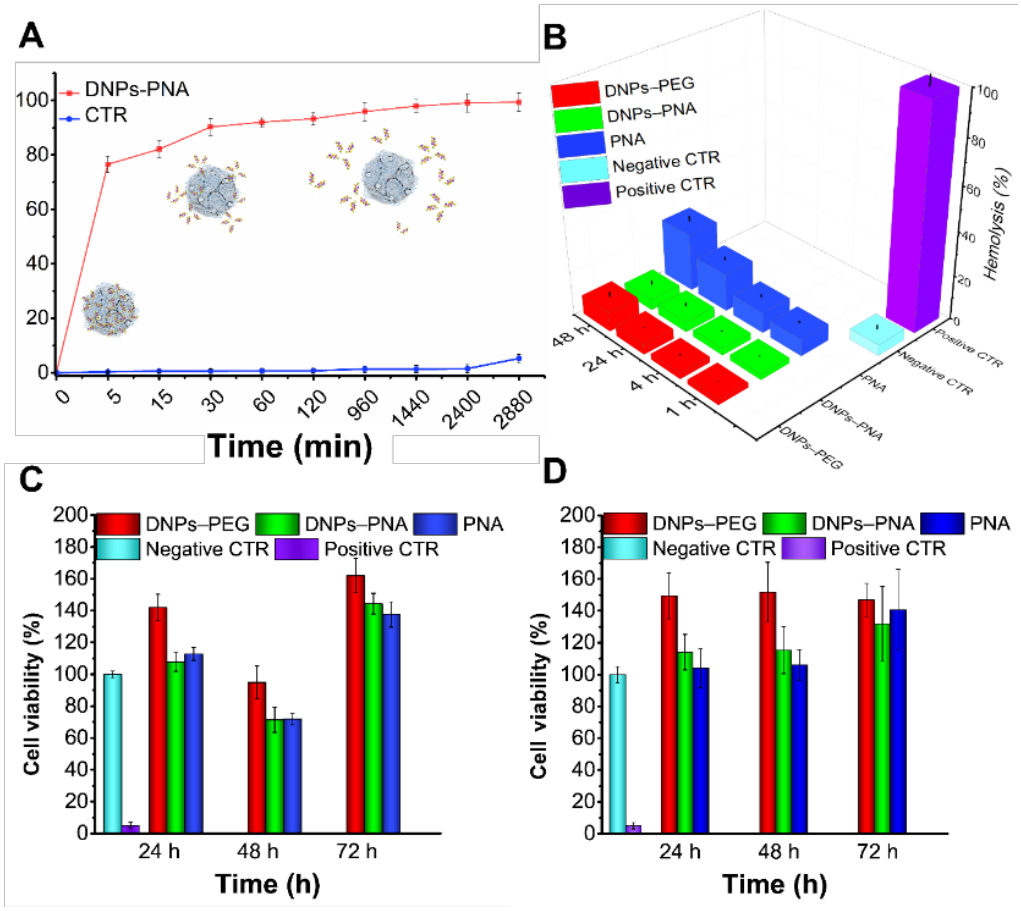

*Figure 19 A) Drug release profile of the DNPs–PNA (where DNP is diatomite nanoparticles, PNA is peptide nucleic acid) complex in dithiothreitol (DTT)/PBS reducing solution (DNPs–PNA) and in PBS solution without DTT (CTR) at 37 °C. Values represent the mean ± s.d. (n = 3). B) Hemocompatibility of the modified-DNPs and free PNA estimated by spectrophotometric methods (577 nm) to analyze the amount of lysed-hemoglobin %. The data are presented as mean ± s.d. (n = 3) and were analyzed with one-way analysis of variance (ANOVA). The level of significance from negative control was set at the probabilities of *p < 0.05, **p < 0.01, and ***p < 0.001. C) Cell viability of MDA-MB-231 and D) A549 cells after exposure to the modified-DNPs and free PNA at concentrations of 200 μg mL^{-1} and 0.01 μmol, respectively. Complete medium (10% FBS RPMI) and Triton X-100 (1%) were used as negative and positive controls, respectively. The data are presented as mean ± s.d. (n = 3). Statistical analysis was made by one-way ANOVA comparing all datasets to the negative control. The level of significance was set at the probabilities of *p < 0.05, **p < 0.01, and ***p < 0.001.*

Cellular uptake study

The cellular uptake was investigated by flow cytometry at two different incubation times (6 and 12 h) to evaluate the enhancement

in the uptake given by the delivery of the PNA molecule with the diatomite-based hybrid nanosystems compared to the free PNA. A complete internalization was already observed after 6 h of incubation for the DNP–PNA particles, while free PNA further increased the internalization between 6 and 12 h (Figure 17A and B; Figure 20 A and B).

The cellular uptake evaluated by confocal microscopy imaging on both cancer cells up to 24 h of incubation with the labelled DNPs (DNPs–PNA*, 50 μg mL-1), confirming that these nanocarriers improved the internalization of the PNA molecules and increased their intercellular accumulation (Figure 20C and Figure 20C). In previous studies, the NPs modified with positively charged functions showed better cellular uptake than negative or neural charged ones due to electrostatic interaction with negatively charged cell membrane[84-85]. Despite the PNAs being synthesised with the positive poly-Lys chain, the obtained results confirm the advantage of using NPs for the intracellular delivery of PNA, facilitating the cell membrane barrier crossing.

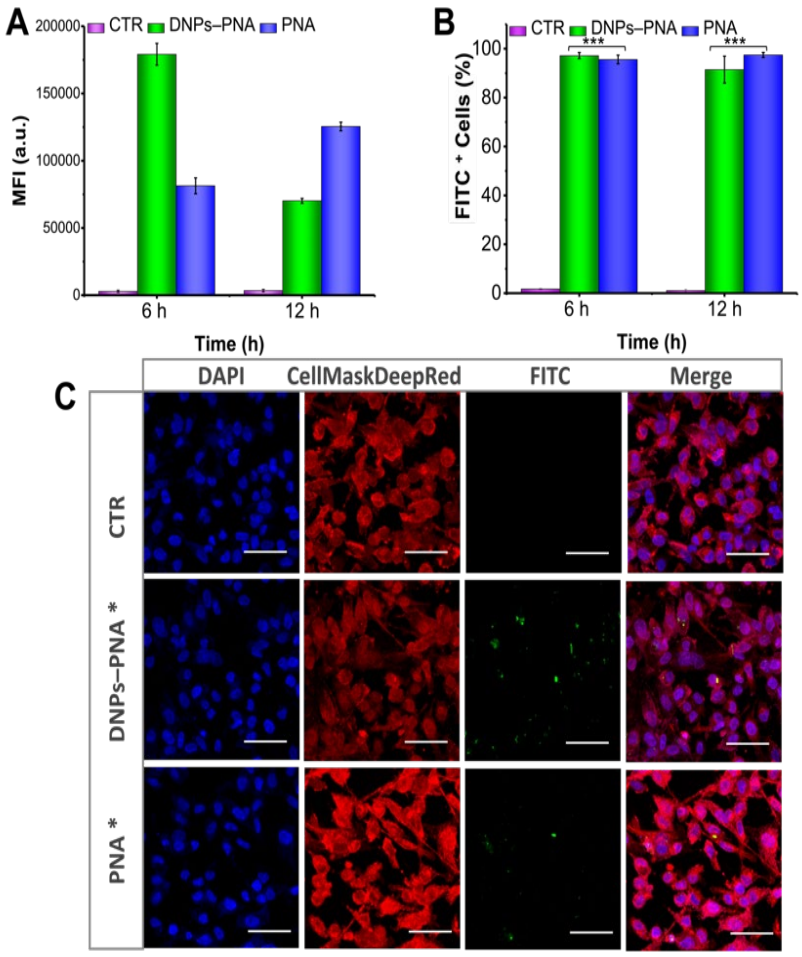

Figure 20 A) Mean fluorescence intensity (MFI) and B) percentage of FITC⁺ MDA-MB-231 (where FITC is fluorescein isothiocyanate) incubated with DNP-PNA-FITC (DNPs–PNA, 50 μg mL^{-1}) (where DNP is diatomite nanoparticles, PNA is peptide nucleic acid) or free PNA-FITC (PNA*, 0.005 μmol) in complete medium for 6 or 12 h. Upon each time point, the wells were extensively washed, and the cells detached. The samples were then incubated with 0.005% Trypan Blue to quench the FITC fluorescence outside the cells. The fluorescence was then analyzed by flow cytometry. The data are presented as mean ± s.d. (n = 3) and were analyzed with one-way ANOVA. The level of significance from negative control was set at the probabilities of *p < 0.05, **p < 0.01, and ***p < 0.001. C) Confocal microscope images of MDA-MB-231 cells incubated with DNPs–PNA* or PNA* for 24 h. Upon each time point, the wells were extensively washed. We then stained the cell membrane with Cell Mask Deep red, while the cell nuclei were stained with DAPI. The images were acquired with a Leica TCS SP8 STED 3X CW 3D inverted microscope, using a 63× objective*

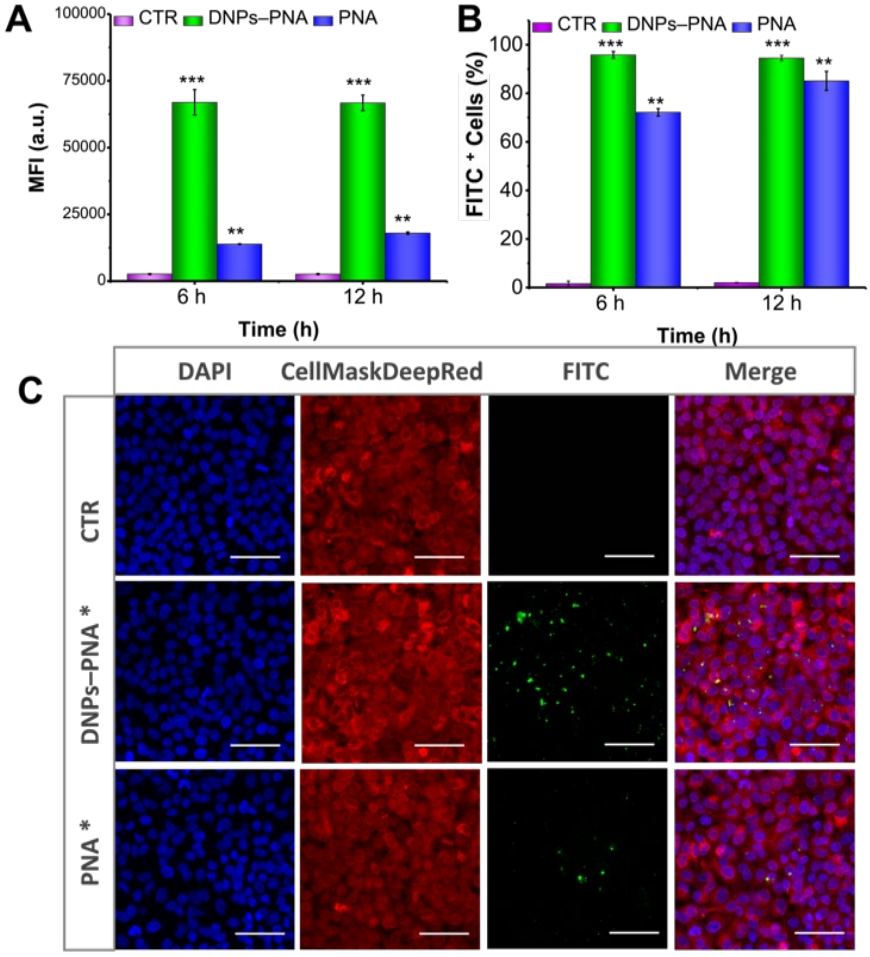

Figure 21 A) Mean fluorescence intensity (MFI) and B) percentage of FITC⁺ A549 (where FITC is fluorescein isothiocyanate) incubated with DNP-PNA-FITC (DNPs–PNA, 50 μg mL^{-1}) (where DNP is diatomite nanoparticles, PNA is peptide nucleic acid) or free PNA-FITC (PNA*, 0.005 μmol mL^{-1}) in complete medium for 6 or 12 h. Upon each time point, the wells were extensively washed, and the cells detached. The samples were then incubated with 0.005% Trypan Blue to quench the FITC fluorescence outside the cells. The fluorescence was then analyzed by flow cytometry. The data are presented as mean ± s.d. (n = 3) and were analyzed with one-way ANOVA. The level of significance from negative control was set at the probabilities of *p < 0.05, **p < 0.01, and ***p < 0.001. C) Confocal microscope images of A549 cells incubated with DNPs–PNA* or PNA* for 24 h. Upon each time point, the wells were extensively washed. We then stained the cell membrane with Cell Mask Deep red, while the cell nuclei were stained with DAPI. The images were acquired with a Leica TCS SP8 STED 3X CW 3D inverted microscope, using a 63× objective.*

2.5.8 Activity study

The efficacy of the developed PNA-based nanosystems in downregulating PD-L1 was evaluated by flow cytometry analysis of the extracellular PD-L1 expression after cells exposure to DNPs–PNA 50 μg mL-1 up to 72 h. [86-88] For this study, MD-MBA 231 triple negative breast cancer cells, A549 lung cancer and U87 glioblastoma cells were chosen for their high expression of PD-L1.
Firstly, the downregulation of PD-L1 was functionally achieved only in MDA-MB-231 cells with a reduction of about 30 % after 72 h (Figure 21A-6B). We initially hypothesized that a functional downregulation could be achieved only in cell lines expressing high basal level of PD-L1, ca. 90% of MDA-MB-231 cells express PD-L1 on their membranes in the same conditions of the study (Figure 21 B). The percentage of A549 cells expressing PD-L1 ranges between 40 and 60%, with a time-dependent increase in the expression in the assay conditions (Figure 21C-21D). Thereby, we chose the U87 cell line for its higher expression of PD-L1 (between 70 and 90%, with a time-dependent decrease in the assay conditions; Figure 21E- F). However, the results obtained in U87 cells highlight that the basal expression of PD-L1 is not influencing the activity level of the PNA.
Importantly, the downregulation of PD-L1 on MDA-MB-231 was achieved only by the NPs conjugated to the wild-type sequence (DNP–PNA) proving that the NPs can effectively deliver PNA to the cells and the presence of the redox-responsive bond allows for the timely detachment of the PNA. Furthermore, the NPs conjugated to a scrambled PNA sequence (DNPs–PNA-CTR) built with the same components in random order does not show any effect, confirming the specificity of the PNA sequence produced towards PD-L1. Interestingly, in the case of A549 cells, the incubation with DNP–PNA particles increases the expression of PD-L1, while no statistically significant changes were detected in U87. However, further studies will be carried out to better understand these preliminary results. [89-91]

Experimental Section

Synthesis of peptide nucleic acid oligomers (PNA), purification and analysis

To develop an effective antisense PNA, we selected the 18-mer target sequence on the PDL-1 mRNA (NCBI Reference Sequence: NM_014143.4). First, we consulted the Uniprot database (https://www.uniprot.org) to identify the wild-type PD-L1 protein (Q9NZQ7) to select the corresponding mRNA tract (NM_014143.4) found in the NCBI dataset (https://www.ncbi.nlm.nih.gov). Within the whole transcript, we identified the PD-L1 Open Reading Frame (ORF) by the Reverse Translate Program, part of the Sequence Manipulation Suite tool (https://www.bioinformatics.org/sms2/rev_trans.html).
Into the ORF region, we identified the most suitable sequence to target, also considering the appropriate characteristics of the PNA sequence to synthesize. The following criteria had to be satisfied: (i) Isolate a high purine tract in the target mRNA to synthesize a complementary antisense PNA rich in pyrimidines and increase the yield % of the synthetic process; (ii) Design the hybridization process in the antiparallel orientation, considered the most stable and efficient form of interaction thermodynamically; (iii) Find nucleotide repeated motifs along the target and synthetic PNA strands to enhance the chance of a successful hybridization; (iv) Verify the lack of self-complementarity or self-dimerization, by using the OligoAnalyzer™ Tool (https://eu.idtdna.com) for both the selected mRNA tract and the complementary PNA sequences; (v) Demonstrate almost the absence of complementarity with the whole transcriptome in both parallel and antiparallel orientation, to avoid potential interactions with random RNA located in the cytoplasm by using the Basic Local Alignment Search (BLAST) Toolset in the BLASTn (nucleotide) interface (https://blast.ncbi.nlm.nih.gov/Blast.cgi). We synthesized the PNA oligomers with a 6-lysine chain (6Lys) to improve solubility and cellular internalization (Table 5) by the 9-fluorenylmethoxycarbonyl (Fmoc) solid-phase strategy and purified them by semipreparative by HPLC analysis, according to the method described elsewhere.[26] We characterized the final pure products by electrospray mass spectrometry (ESI-MS) using a 4000 QTRAP mass spectrometer (ThermoFisher Scientific, Waltham, MA, USA).Prior to each conjugation step with the NPs, we also treated the sequences with an excess of DTT (PNA: DTT = 1: 50 molar ratio) for 30 min under gently stirring to reduce eventually undesired disulfide bridges and purified them by HPLC.

Sample	Sequence
wild type PNA (PNA)	N-term-ACCATACTCTACCACATA-6Lys-Cys-C-term
wild type-FITC PNA (PNA*)	N-term-FITC-ACCATACTCTACCACATA-6Lys-Cys-C-term
scrambled PNA (PNA-CTR):	N-term-ACATCATATCCAATCCAC-6Lys-Cys-C-term
scrambled PNA-FITC (PNA-CTR*)	N-term-FITC-ACATCATATCCAATCCAC-6Lys-Cys-C-term

Table 5 PNA molecules synthesized by solid phase peptide synthesis method and used for DNPs surface functionalization.

One-pot synthesis of redox-responsive DNPs and PNAs conjugation
We synthetized the redox-responsive complex by dissolving APTES and PEG (1:1 ratio, 7.5 µmol of each molecule) in 0.1 mL of DMF under constant stirring (800 rpm) for ON at RT. When elapsed the time, we directly dispersed the bare DNPs (1 mg) in the APTES–PEG/DMF solution under stirring, ON at RT. We centrifuged the NPs for 30 min at 15,000 rpm and discarded the supernatant. We rinsed the NPs (DNPs–PEG) thrice with DMF, twice with MilliQ-water and re-suspended them in the same solvent. Finally, we conjugated the DNPs–PEG (1 mg) with PNA wild-type (0.1 µmol, molar ratio NPs:PNA = 5:1) in 0.5 mL of 40 mM sodium phosfate, 2 mM EDTA solution, pH 7.6 at 30°C, ON under stirring. The DNPs–PNA were centrifuged for 30 min at 15,000 rpm and the supernatant was removed and the NPs were washed five times with MilliQ-water. We used the same bioconjugation procedure to functionalize the NPs with the different PNA sequences, as shown in Table 3.

NMR spectroscopy standard 1H NMR experiments

We collected the solution 1H proton NMR data by a Bruker Advance III 700 spectrometer (Bruker BioSpin GmbH, Rheinstetten, Germany), operating at 700 MHz. The following samples, APTES (0.01-7.5 µmol) in 600 µL of DMF-d; OPSS-PEG-NHS (0.010-7.5 µmol) in 600 µL DMF-d; APETS/PEG complex (ratio 1:1, 7.5 µmol of each molecule) in 600 µL DMF-d; PNA 0.01 µmol in 600 µL DMF-d were all performed using standard 1H NMR protocol (128-256 scans, 2 dummy scans, 1 s relaxation delay). For qNMR, we dispersed dried modified-NPs (0.1 up to 2 mg) in 600 µL DMF-d or D2O, sonicated in an ultrasonic bath for 60 s, transferred to dry NMR tube (5 mm) and characterized them by NMR (256 scans, 2 dummy

scans, 6 s relaxation delay). We used fumaric acid (10 mg in 1 mL of DMF) with resonance at 6.64 ppm as internal calibrant and we added approximately 5-50 µL of the prepared solution the NPs sample before each analysis.
NMR spectra were processed by MestReNova software (Mestrelab Research, S.L., Spain). After Fourier transformation, the chemical shift was referenced by the residual signal of DMF-d7 used as solvent (a broad peak cantered at 8.03 ppm). The phase was corrected automatically first, followed manual adjustment for specific peaks if the automatic correction was not satisfying. The baseline was corrected by fifth-order polynomial fit with manually adjusted filter.
To calculate the functionalization yield, we compared the signals of the compound of interest with those of fumaric acid as internal calibration compound. The concentration of a compound in the presence of a calibrant is calculated using Equation (1):

$$Cx = \frac{I_x}{I_{cal}} \times \frac{N_{cal}}{N_x} \times C_{cal} \quad (1)$$

where, I, N and C are the integral area, number of protons and molar concentration of the compound of interest (x) and the calibrant (cal), respectively.
The number of mols of the interest compound is obtained by Equation (2):

$$Cx = \frac{n}{V} \quad (2)$$

where, n and V are the number of mols and volume of the solution compound of interest (x), respectively.

Drug loading and release

We determined the drug loading capacity of the PNA-FITC modified-DNP (DNPs–PNA*) by immersing the NPs (0.1 mg) into PBS buffer (1 mL, pH 7.4 and 5.5) without or with DTT (20 and 100 mm) at 37 °C for 48 h under mild stirring. After the release test, we added an excess of DTT (100 mm) into the NPs suspension to completely release all PNAs. We removed the NPs by centrifugation, and we quantified the PNA* released in the supernatant by spectrofluorometer (FP-8250, Jasco Europe, Italy). All measurements were repeated at least three times. We quantified the amount of PNA using an external calibration method by comparing the fluorescence intensity of the supernatant at 520 nm with known concentration of PNA-FITC as standard.

In vitro release tests were performed by shaking the DNPs–PNA* (0.1 mg) into PBS buffer (1 mL, pH 7.4) without or with DTT (20 and 100 mM) at 37 °C for 48 h under mild stirring. At predetermined time intervals, we centrifuged the release solution was at 15,000 rpm for 5 min, collecting the supernatant and replacing it with fresh buffer until the subsequent sampling time. We analyzed the collected supernatants by spectrofluorometer according to the above-described method. The cumulative percentage release was calculated by using Equation (3) and (4):

$$\text{Release } \% = \frac{\text{PNA released at t time (µmol)}}{\text{total PNA loaded (µmol)}} \cdot 100 \quad (3)$$

$$\text{Cumulative release } \% = \mathrm{P(t-1)} + \mathrm{Pt} \quad (4)$$

where, P(t-1) = percentage of PNA released at a previous time to t and Pt = percentage of PNA released at time t.

Activity studies

The activity of PNA in inhibiting the expression of PD-L1 was assessed by quantification of the expression of PD-L1 on the cell membrane by FCM. Briefly, 1×105 cells were seeded in 12-well plates and then placed back in the incubator for 24 h to allow for a complete attachment. The medium was then removed, and the samples were added at the concentration of 50 µg mL-1in complete medium. The cells were then incubated with the samples for 24, 48, and 72 h. At each time-point, the samples were removed from the wells. Then, we washed the wells twice with PBS. The cells were detached from the wells with a scraper, transferred to a v-bottom 96 well plate and centrifuged at 300g in an Eppendorf R5100 centrifuge for 5 min. The supernatant was discarded, and the cells were resuspended in 20 µL of TruStainX FcBlock solution (2 µL of TruStainX FcBlock plus 18 µL of PBS) and incubated at RT for 10 min. We then added 80 µL of Antibody solution to each of the samples, except for the blanks (1 µL PE anti human CD274 plus 79 µL of PBS). We added 80 µL of PBS in the blank wells. The cells were then incubated on ice at +4°C for 20 min. The cells were washed twice with cold PBS, resuspended in 200 µL of cold PBS and analyzed with a BD Accuri flow cytometer equipped with C6 autosampler (BD Biosciences, USA). The data were then analyzed

with floreada.io to quantify the mean fluorescence intensity and the percentage of PE positive cells, according to the gating strategy reported in Figure S15.

Statistical analysis

Results of the assays are expressed as mean ± standard deviation (s.d.) of at least three independent experiments. Results were evaluated by means of one-way analysis of variance (ANOVA) with the level of significance set at the probabilities of *p< 0.05, **p< 0.01, and ***p< 0.001 using Origin 8.6 (Origin Lab Corp., USA).

Conclusion

PNA as the best oligo-mimetic requires to be delivered and as Anisha Gupta et al. reported several attempts were tried to accomplish the goal (DOI:10.1016/j.jconrel.2016.01.005). We identified the production of redox-responsive drug delivery systems using natural silica from diatomite as suitable platform for controlling intracellular delivery of a PNA. We started from designing and synthetizing a PNA strand to downregulate the PD-L1 expression on cancer cells via antisense strategy. The synthesis and functionalization of nanoparticles was obtained by a simple one-pot chemical strategy, even though the conventional multi-step strategy was unsuccessfully performed. The used approach allowed to reach the highest percentage of PEG surface coating needed to confer them stability, biocompatibility, and functional moiety for covalent PNA conjugation via the redox responsive disulfide bond. The drug loading study assessed the interaction of PNA with the NPs and the in vitro release study showed a redox-triggered of the PNA compared with the amount of PNA realised studies in physiological coditions. The preliminary activity studies on different cancer cell lines (MDA-MB-231; A549 and U87) showed the downregulation of PD-L1 only on MDA-MB-231 by the NPs conjugated to the wild-type sequence (DNP–PNA), while no activity was observed in the case of NPs conjugated to a scrambled PNA sequence (DNPs–PNA-CTR), confirming the specificity of the synthesized PNA sequence towards PD-L1. Overall, the developed redox-responsive natural-based silica nanocarriers, easy to produce, with suitable physicochemical properties for on-demand drug delivery are

promising for targeted therapy overcoming the drawbacks of conventional therapy.

Objective 3 Development of an Oncolytic Adenoviral platform for the delivery of an anti-PD-L1 PNA to modulate the PD-L1 overexpression in cancer cells (Unpublished manuscript)

It is widely acknowledged that tumors have the ability to change gene expression and modulate the surrounding biological microenvironment to deal with growth, invasion, and metastasis. There is a growing body of knowledge regarding the role of PD-L1/PD-1 immune checkpoint in cancer cells, and the discovery of a link between PD-1/PD-L1 expression and poor prognosis in many tumor types such as gastric, ovarian, lung, and renal carcinoma is illustrative of this finding [93].

It has been shown that permeant-activated immune cells (primarily T-cells) are able to infiltrate tumors and induce tumor cell death by exploiting, among other mechanisms, the PD-1/ PD-L1 checkpoint one. It was found that cancer exposed PD-L1 as a transmembrane protein on the surface of the cell, which acted as an escaping signal for the immune system, thus promoting tumor proliferation. In response, monoclonal antibody treatments have been developed to boost defenses against cancer by blocking PD-L1 or PD-1 activity in cancer patients [94].

While nearly half of the treated patients showed a positive response to monoclonal antibody treatments (66%), this approach also had several negative aspects, particularly those that involved unspecific action against healthy cells [95].

With the advent of oligonucleotide therapeutics as an emerging approach to modulate the alteration of protein expression in tumor conditions, we proposed a novel approach by targeting PD-L1 mRNA for the downregulation of PD-L1 protein. Gene and protein expression are controlled by antigene or antisense mechanisms, which use synthetic oligonucleotides to target an endogenous DNA or RNA sequence and trigger the arrest of transcriptional and translational machinery recruitment, respectively [96,97].

There are limitations to the application of synthetic oligonucleotides in therapy due to their pharmacokinetics. Hence, the oligonucleotide scaffold is selectively recognized and inactivated by endogenous enzymes, such as nucleases. In order to overcome this limitation and to enhance their relevance in therapy by overcoming their early enzymatic interception and degradation, the

synthesis of chemically modified mimics of oligonucleotides was proposed [98].

Peptide Nucleic Acids (PNAs) [99]are oligonucleotides that mimic DNA and RNA by replacing the sugar-phosphate backbone with a neutral peptidyl group enabling the precise recognition of a complementary DNA or RNA strand and the formation of a more robust heteroduplex complex suitable for the antisense and antigene therapeutic approach [[100,101].

Because PNA is highly apolar and has a neutral backbone, it cannot pass through cell membranes on its own, so a delivery platform is required for PNA applications [102]. Several delivery platforms for PNA have been developed, and it is speculated that they need to function as tissue-specific platforms to control the side effects associated with non-specific release of drugs [103]. Our group has proposed the functionalization of anticancer adenoviral particles with the ability to infect and multiply malignant tumors [104]. Oncolytic virus therapy broadly emphasizes the oncolytic nature of viruses to facilitate the development of immunotherapy-based anticancer therapies. In addition to their ability to penetrate only cancer cells, oncolytic viruses are also excellent platforms for developing anticancer therapies. The anionic viral surface can carry cationic small molecule compounds and drugs through electrostatic interactions. Due to its high infection specificity and ability to complex with therapeutic agents, the adenovirus form was designated as a predicate delivery platform for the proposed anti-PD-L1 strategy. Therefore, in this study, an antisense strategy PNA-based to develop a delivery platform favorable for electrostatic interaction with the carrier was set up. The coating of adenovirus Δ24 5/3 surface with an anti-PD-L1 PNA tagged with a lysine tail affected the PD-L1 overexpression in cancer cells.

PNA Sequence Identification

PNAs, as oligonucleotide mimics, have been extensively studied in therapy. It has been reported that PNA-based treatments worked with antisense, antigene, and anti-miRNA activity 105 The dynamism of PNA synthesis allows designing the PNA strands to adjust their cell delivery according to the desired application. Consequently, the addition of peptidyl residue at PNA terminals is used to regulate the overall charge of the PNA. The addition of the serine phosphate residue confers on PNA backbone a negative

charge, suitable for the complexation of lipofectamine, used as a standard for the intracellular release of exogenous DNA and RNA molecules, for example[106]. In previous works, we developed a proper virus-mediated delivery platform by conjugating a positively charged PNA strand to the surface of an oncolytic adenovirus thanks to the manual elongation of a six-residue lysine tail on the carboxyl terminal of the PNA. Following the lines of the previous work, we laid out a sequence of a six-lysine conjugated PNA of 18 bases, called anti-PD-L1 antisense PNA, to target a small region of PD-L1 mRNA in cancer cells. In silico studies were conducted to choose the target sequence of PD-L1 mRNA and its complementary PNA to be synthesized. The wild-type PD-L1 amino acid chain was identified, and the open reading frame of PD-L1 was isolated, ORF 1. (https://www.bioinformatics.org/sms2/revtrans.html). Altogether, along the entire ORF 1 region, we selected a short tract of the transcript, 18 mer in length, to target with a complementary PNA strand, acting as an antisense oligonucleotide (ASO). The following criteria had to be satisfied to identify the most targetable mRNA tract and its complementary PNA to be synthesized107:

· Isolate a high purine tract in the target mRNA to synthesize a complementary antisense PNA rich in pyrimidines and increase the yield (%) of the synthetic process

· Arrange the orientation of the hybridization in the antiparallel mode, that was thermodynamically defined as the most stable and efficient.

· Recognize specific nucleotide repeated motifs along the target and synthetic PNA strands to enhance the chance of a successful hybridization.

· Verify the lack of self-complementarity or self-dimerization by using the OligoAnalyzer™ Tool (https://eu.idtdna.com) for both the selected mRNA tract and the complementary PNA sequences.

· Demonstrate almost the absence of complementarity with the whole transcriptome in both parallel and antiparallel orientation, to avoid potential interactions with random RNA located in the cytoplasm by using the Basic Local Alignment Search (BLAST) Toolset in the BLASTn (nucleotide) interface (https://blast.ncbi.nlm.nih.gov/Blast.cgi).

The parameters above allowed us to pick the mRNA region to target. Table 6 listed the synthesized ASO sequence (Anti-PD-L1 PNA antisense) complementary to the target and its scrambled sequence (Scrambled PNA) used as a control. FITC labeled PNAs for each

sequence were also synthesized for the subsequent cellular uptake studies, fig.22.

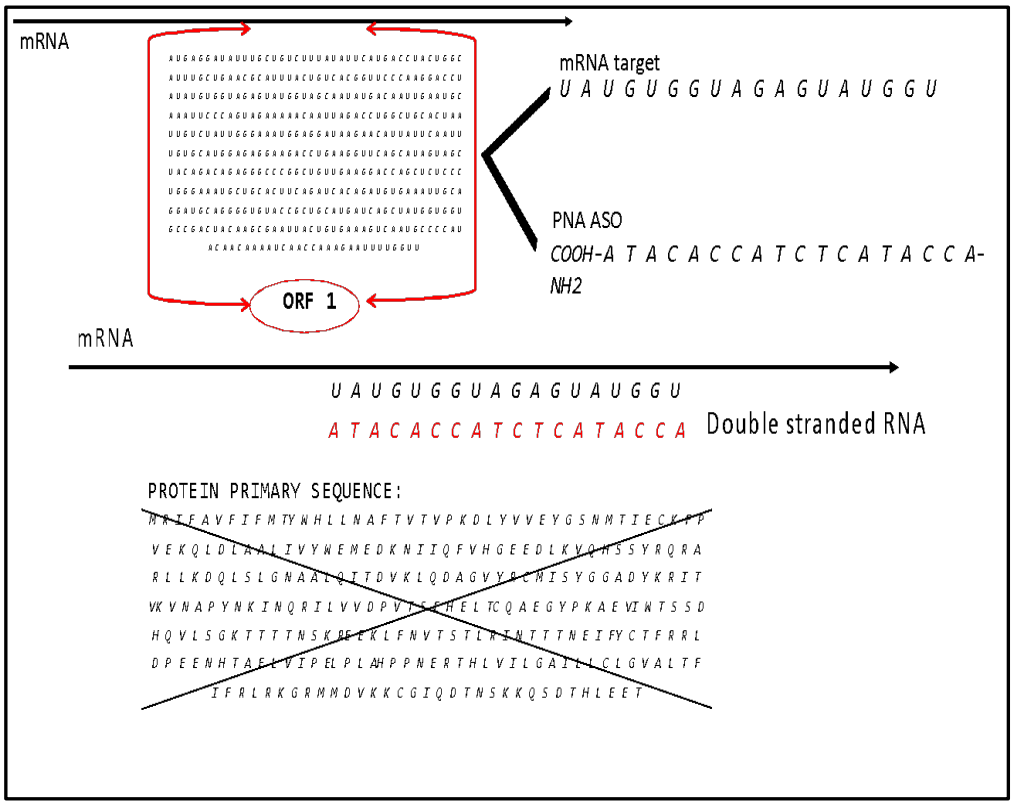

Figure 22 Protein identification: the Uniprot database (https://www.uniprot.org). The transcript (NM_014143.4) in the NCBI dataset (https: //www.ncbi.nlm. nih.gov / nuccore / NM_014143.4) was identified and the Open Reading Frame of the protein verified.

PNA SEQUENCE:	
Anti-PD-L1 PNA antisense [ANTISENSE PNA]	NH_2-ACCATACTCTACCACATA-6K-COOH
Scrambled PNA	NH_2-ATACACTATCCAATCCAC-6K-COOH
FITC Anti-PD-L1 PNA antisense [FITC ANTISENSE PNA]	FITC-linker-linker-ACCATACTCTACCACATA-6K-COOH
FITC Scrambled PNA	FITC-linker-linker-ATACACTATCCAATCCAC-6K-COOH

Table 6 List of PNA Sequences synthesized

Oncolytic Adenovirus decoration

Pilot experiments based on viral treatments, in particular on Adenoviruses (Ad), revealed the enormous immunogenicity derived from the administration of Ad in vivo, related to the specific interaction between the viral capsid and the immune sensors known as pattern recognition receptors (PRR) [108–110]. To resolve the viral safety profile, immunogenicity points have been hidden by masking the external viral fiber and slowing the immune system's reactivity. As one of the first proposed viral functionalization, the PEGylation procedure has been defined as a satisfactory method of bringing down the immune system's reactivity [111,112]. Consequently, the idea of coating the Ad capsid has been extended to different applications to obtain new viral treatments [113]. Hence, viral vector direction guided by peptides, ligands, or part of an antibody added to capsid proteins was proposed and demonstrated viruses' broad range of action as therapeutics.
Furthermore, the arrangement of the viral surface with non-viral traits aimed at the idea of using the adenovirus as a vector to deliver therapeutics. The morphological and physiological asset of oncolytic adenoviruses (OAds) makes them elective vehicles for advancing a specific anticancer treatment thanks to the synergistic effect of the viral oncolytic competence and the antitumor effect of the administered compound. Specifically, the surface reaction between anionic adenovirus with cationic peptides has been extensively

experimented with to form a cationic complex that can be internalized in a wide range of tumor cells [114]. With this last aim, we have provided the complexation of OAds Δ 24 5/3 with an anti-PD-L1 antisense PNA. The surface functionalization for developing a viral delivery platform was based on the OAd protein: PNA weight ratio, as described elsewhere. The functionalization process working on a significant excess of reagents, respect to the surface to be functionalized, was set at 10, 50, and 100 equivalents of PNA to react with the viral surface. The electrostatic interaction between the viral membrane and the PNAs was mediated by the positively charged lysine tail disposed at carboxyl-termini of the PNAs. The complexation process protocol was evaluated by Dynamic Light Scattering (DLS) analysis. The DLS acquisition analyzed the quality of functionalization by measuring the resulting size OAd:PNA complexes. In general, the size of the final complex, when is very close to the size of the non-functionalized support, ensures the absence of aggregates in the solution. Accordingly, we measured the size of the OAd alone and the average viral particle size calculated was 121 nm. The complexation step in the three different concentration of PNA was tested and after the DLS measurement, we selected the ten equivalents of PNA as the proper experimental setting to generate homogeneous-size-distributed OAd complexes with each PNA. The selected experimental approach produced particles of 129 nm and 135 nm, OAd:PNA antisense and OAd:PNA scrambled, respectively. The calculated polydispersity index (PDI) was 0.2 for each sample and accordingly with the homogeneity of the analyzed solution we excluded the presence of aggregates in the solution. The Zeta Potential measurement corroborated the success of functionalization. We studied the Zeta potential of anionic OAd dissolved in water as a starting point, measuring -23mV. As expected, OAd:Antisense PNA and OAd:Scrambled PNA surface potential shifted from the negative range to the positive one after the functionalization, recording 26.5 and 21 mV. Data shown in fig.23.
The OAd complexes resulting size and surface potential were compared with the hydrodynamic diameter and the zeta potential of an antisense PNA aqueous solution. As expected, the analysis detected the presence of aggregated and partially insoluble particles of 439 nm and with a net cationic charge of 30 mV. Subsequently, the last observations confirmed the hardly dissolution in near physiological condition and supported the urgency of developing a suitable delivery platform for their further application in therapy.

OAd: PNA complexes derived from the combination of 50 and 100 PNA equivalents were similarly tested, and for both conditions, DLS analysis detected large particles in solution after complexation, data reported in the support section. Considering that the particle size, bigger than 200 nm, was not conceivable with the intracellular release [115], we did not test the derived complexes in vitro. Furthermore, positive values of Zeta Potential were measured for both conditions, suggesting that functionalization occurred.

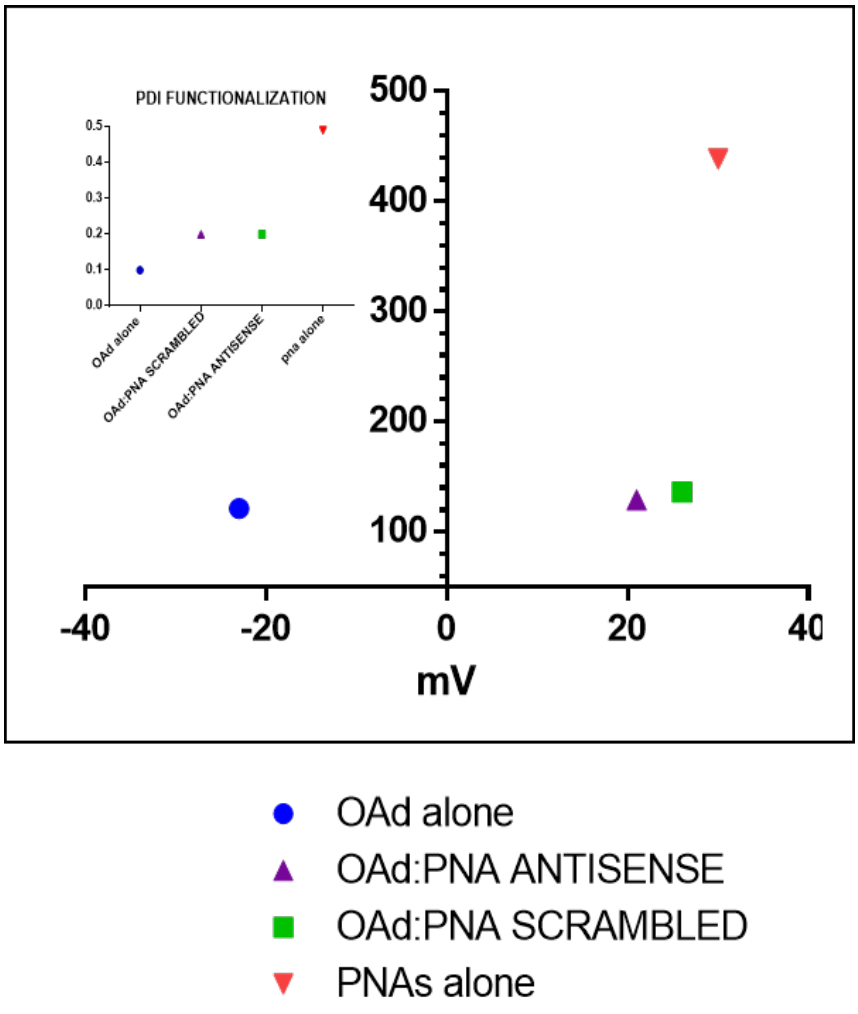

SAMPLE	SIZE (nm)	ζ POTENTIAL (mV)	PDI
OAd alone	121 ± 4	-23 ± 0	0,15
OAd:PNA Antisense	129 ± 3	+26,5 ± 2	0,2
OAd:PNA Scrambled	136 ± 4	+21 ± 8	0,26
Pnas Alone	439,7	+30	0,49

Figure 23 DLS and Zeta Potential characterization of OAd particles unfunctionalized, functionalized with Antisense and Scrambled PNA in the 1:10 weight ratio, the analyzed condition listed in the table.

Cytotoxicity

A549 and SK-OV3 human cell lines, lung and ovarian tumors, respectively, were used to perform the in vitro studies. Both cell lines were reported to be characterized by by PD-L1 deregulation[116]. As a starting point, we analyzed the toxicity of the OAd:PNA complexes by performing a cell viability test (MTS assay), referring to cells infected with the OAd alone as a positive control. In the end, we correlated each other with the untreated cells (NT), and cells treated with PNAs alone viability levels were considered negative controls.
As already mentioned, the severity of the viral infection depends on the time lasting and the amount of the viral particles infecting cells. The MOI (multiplicity of infection) is the number of viral particles (VPs) that can infect each cell in the tissue culture vessel. The MOI value, measured for high concentrated viral preparation, can be tuned to module the acerbity of the infection in vitro [117].
Considering the well-known known OAd cytotoxicity[118], we measured the cell viability after 48 h. Here, we discuss the 100 VPs/cell combination (0.1-1000VPs/cell conditions were tested). For the best interpretation of the resulting data, we considered comparable the two different cellular systems' responses due to the adenovirus del 24 5/3 infection capability of obeying several cell mechanisms for infecting tumor cells.
After two days from the infection, no further cytotoxicity was shown for both the cell lines treated with the viral complex compared to those infected with the OAd. In the a549 cell line the treatment with OAd alone the cell survivor was 60%.

Whereas the viability of the cells treated with OAd:PNA antisense and the OAd:PNA scrambled measured 63% and 75%, respectively. A slight enhancement of the cell viability was displayed for the cells infected with the OAd:PNA complexes compared with the cells treated only with OAd.
Furthermore, the viability of NT, 100 %, was correlated to the viability of the cells treated with the PNA antisense alone (100%) and PNA scrambled alone (90%). Therefore, the correlated analysis highlighted that no relevant differences (~10%) in cytotoxicity were attributable to PNA activity.
Conversely, SK-OV3 cells treated with the OAd alone showed the typical cytotoxic profile of infected cells with 56% of viability. The cell viability due to the treatment with the complex OAd:PNA antisense was 67% and 69% for the OAd:PNA scrambled, thus confirming the decreased cytotoxic effect of the viral complexes. The NT viability (100%) was compared to cells treated with PNAs alone, 87% and 90% for the antisense and scrambled PNA. The viability test after 48h of treatment in any considered conditions showed a similar response for both A549 and SK-OV3 cell lines, as mentioned above.
In conclusion, the cytotoxicity test fig. 24, confirmed that the cell suffering derived from the viral infection, at 100 VPs/cell condition tested, was not enhanced by the complexation of viral cells with the PNA strands. Moreover, the severity of the infection seemed to be lightly positive modulated by the functionalized OAd, infection thus recording a higher cell survivor after 48h of treatment.

In addition, the effect of the PNAs themselves did not significantly affect cell viability, assuring the maintenance of the cell survivor after the intracellular release.

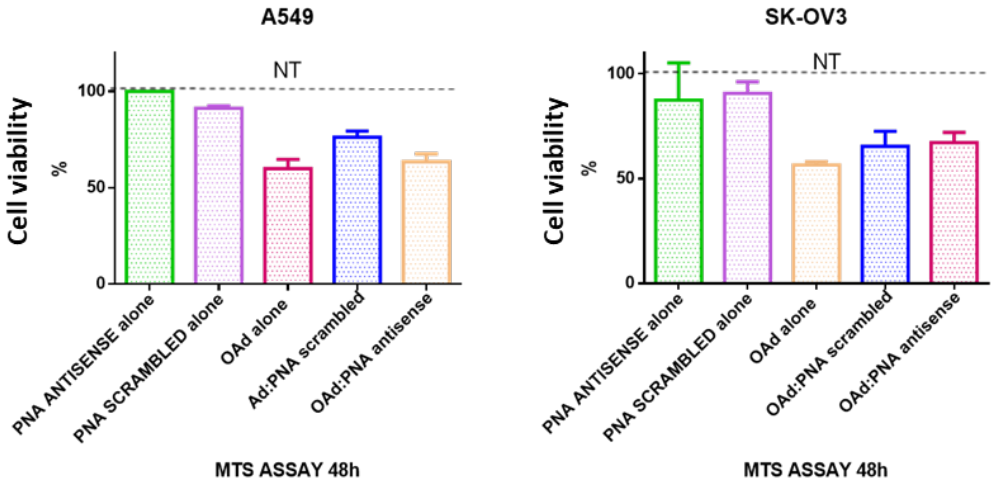

Figure 24 MTS assay at 48 h of A549 (a) and SK-OV 3 (b) cell lines 100 VPs/cell. Dotted line non treated cell (NT).

Intracellular uptake studies

We evaluated the capability of the OAd:PNA complexes and the PNA alone to cross the cell membrane and reach the cell compartments. 100 VPs/cell data were shown.
To perform the analysis, we functionalized, as above mentioned, the OAd with labeled FITC PNAs to allow the tracking of the PNA strands in the cell compartments. As known in the literature the oncolytic adenovirus the lowest timelapse of infection is six hours, hence, we experimented with the PNA internalization process after 24 h of treatment to be sure that the infection process was already expired. The Flow cytometry analysis (FCS) allowed us to evaluate the number of cells that were sensitive to the FITC excitation wavelength, plotting the count of FITC positive cells versus the FITC signal intensity, fig.22. The NT cells and the one treated with OAd were used as control due to the total absence of active fluorescence. The comparative analysis of the cells treated with both OAd:FITC PNA complexes and FITC PNA alone confirmed the positive FITC signal output in opposition to cells treated with OAd alone and untreated ones that showed a low positive FITC signal ascribable to

the natural cell autofluorescence emitted between 350 and 550 nm owing to the ubiquity of several cellular compounds (collagen, elastin, cyclic ring compounds, aromatic amino acids). In both cases, it was assumed that the FITC PNAs and the Virus:FITC PNA interacted with cells even though the situ of the FITC PNA emission in each condition required to be further investigated. The flow cytometry output represented by a histogram diagram framing the count of positive FITC cells was shown in fig.25

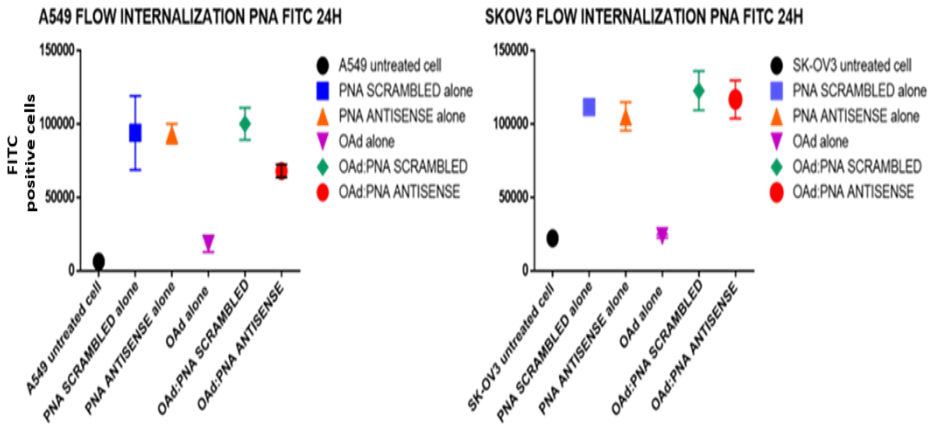

Figure 25 Flow cytometry measurement of FITC positive cells. A549 and SK-OV3, panel a and panel b, treated with FITC PNA, OAd:FITC PNAs, OAd alone, and 1X PBS after 24 h.

Biological Activity by Flow Cytometry (FCS) analysis

The antisense approach recognizes the mRNA sequences of the selected target and reduces the corresponding protein expression avoiding the mRNA translation. We evaluated the antisense effect after 48 h, time-lapse used in the literature to modulate PD-L1 protein expression.
SK-OV3 AND A549 cell lines were treated as mentioned above. The PD-L1 level of expression was quantified by FCS analysis.
OAd, OAd: Antisense PNA, OAd: Scrambled PNA, Antisense PNA alone, and Scrambled PNA alone at 100 VPs/cell were tested compared with the untreated cells, fig.26.
In the cellular population investigated the geometric mean of the antibody's fluorescence intensity (gMFI) for each sample was recorded.

The viral effect on SK-OV3 cells increased the expression level of PD-L1 when infected, as shown in panel a, fig.26. The upregulation of PD-L1 protein might be attributable to a cell mechanism response to the viral infection related to ovarian cancer cells' constitutive production of IL-6.
When the same cell line was treated with the OAd:Antisense PNA complex, the PD-L1 protein signal on the cell membrane significantly decreased, as the gMFI value showed. In addition, the PD-L1 downregulation was evident in comparison with untreated cells but sharper when correlated with the infected ones.
As a negative control, we also analyzed the effect of the undelivered antisense PNA on the SK-OV3 cells as expected. A weak modulation of the protein was displayed, corroborating the inability of the PNA alone to reach the cell compartment sufficiently.
The determination of the sequence-dependent effect of the antisense PNA was verified by studying the biological activity of a Scrambled PNA delivered by an OAd carrier and alone. As expected, no differences in the PD-L1 level of expression in terms of gMFI value were detected after both treatments.
A549 cell lines were studied as well after 48h from the treatment. The treatment with the complex OAd:antisense PNA did not significantly vary the PD-L1 expression when compared with the untreated and with cells infected with OAd.
The same result was obtained after the treatment with the complex OAd:Scrambled PNA fig. 26 panel c-d. Conversely, the Antisense activity of the PNA alone, more than in the SK-OV3 cell line, caused a considerable downregulation of the PD-L1 expression.
Consistently, Scrambled PNA alone did not influence the protein expression after two days of treatment, confirming the attendant data.
The inconsistent ability of OAd:Antisense PNA to modulate the PD-L1 expression in the A549 cell system could be ascribable to the PD-L1 mRNA level of expression. As opposed to SK-OV3, the A549 viral infection did not increase the PD-L1 expression, and considering that in the antisense strategy the downregulation of the protein derives from the mRNA negative modulation we used the A549 system as control to study the OAd:PNA complex platform.
Whereas the proposed delivery platform was already set up to discriminate between tumor and normal tissues, it could further differentiate between cell systems expressing a high and low target

level. This comparative study allowed us to appreciate the desired tissue-specific activity of the proposed antisense strategy.

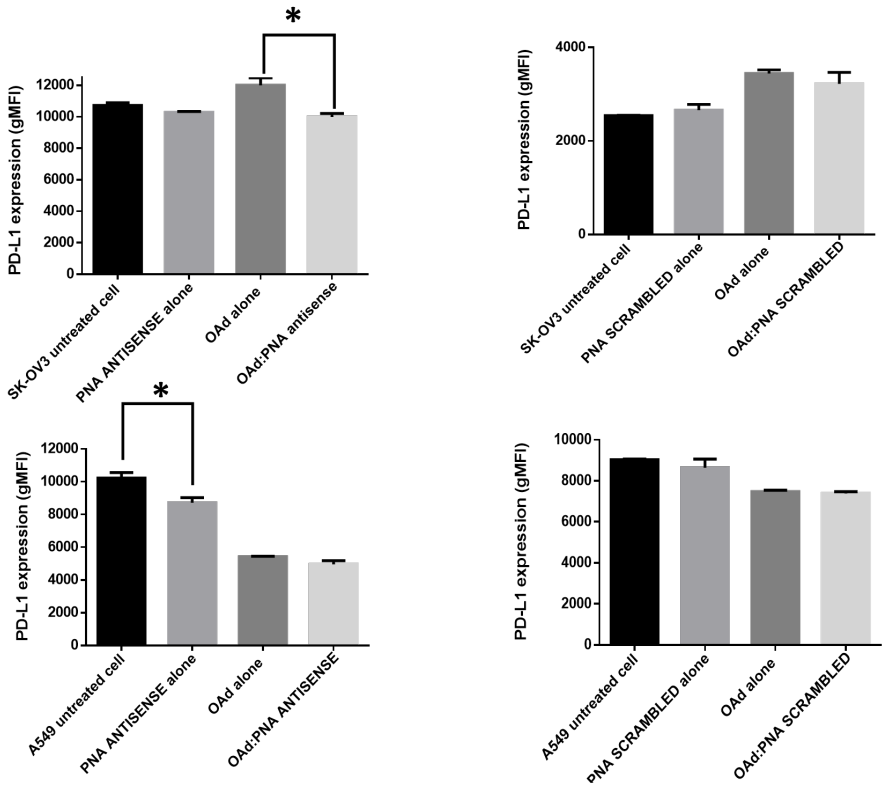

Figure 26 Flow cytometry analysis of PD-L1 espression (gMFI) of SK-OV3 and A549 cell lines, panel a-d, treated with antisense PNA, scrambled PNA, OAd:antisense PNA, OAd:scrambled PNA, OAd alone and 1X PBS after 24 h.

Confocal microscopy analysis

The cell internalization already discussed with FCS analysis was as well as investigated by Confocal microscopy analysis in SK-OV3 cells.

After the treatment in the above-mentioned conditions, we proceeded with a cell-staining process to label the cell compartments and investigate the FITC PNA cellular uptake after 24h from the treatment. The cellmask deep red fluorescent labeling agent was used to mark the cell membranes and the DAPI, a nuclear counterstain, was also applied to tag the nuclear compartment.

The confocal microscopy acquisitions were collected by a single wavelength channel of acquisition (CELLMASK-FITC-DAPI) and the

merge of each panel was adopted for detecting the intracellular PNA uptake and the cell morphology, fig 27 (a-f).
Firstly, untreated cells (panel f) and the infected ones (panel c) were analyzed as controls and setting the single-channel acquisition, no FITC signal was recorded when irradiated with the FITC excitation wavelength. In addition, the untreated cells showed vital and healthy features, while cells infected with the OAd alone presented a suffering cell morphology, as expected after the viral infection.
The images captured after the treatment with both OAd:antisense PNA and OAd:Scrambled PNA (panel d and e) showed a diffuse fluorescence emission signal in the FITC emission channel attributable to the FITC antisense and scrambled PNA signals, respectively. The merged images allowed us to evaluate the localization of the fluorescent PNA in the cell compartments and as displayed in the panel d and e the PNA signals were mostly spread in the cytoplasmatic area. On top, the cell morphology mirrored a not suffering condition, confirming the less cytotoxic effect of the complex OAd:PNA, previously detected by MTS analysis.
Conversely, the cells treated with undelivered FITC PNAs did not show a diffuse fluorescent emission signal. Cells treated with FITC antisense PNA recorded a slight spotted green signal, confirming moderate capability to cross the cell membrane.
The cell shape observed was very similar to the shape of the untreated one, supporting that no toxic effects could derive from the PNA activity.

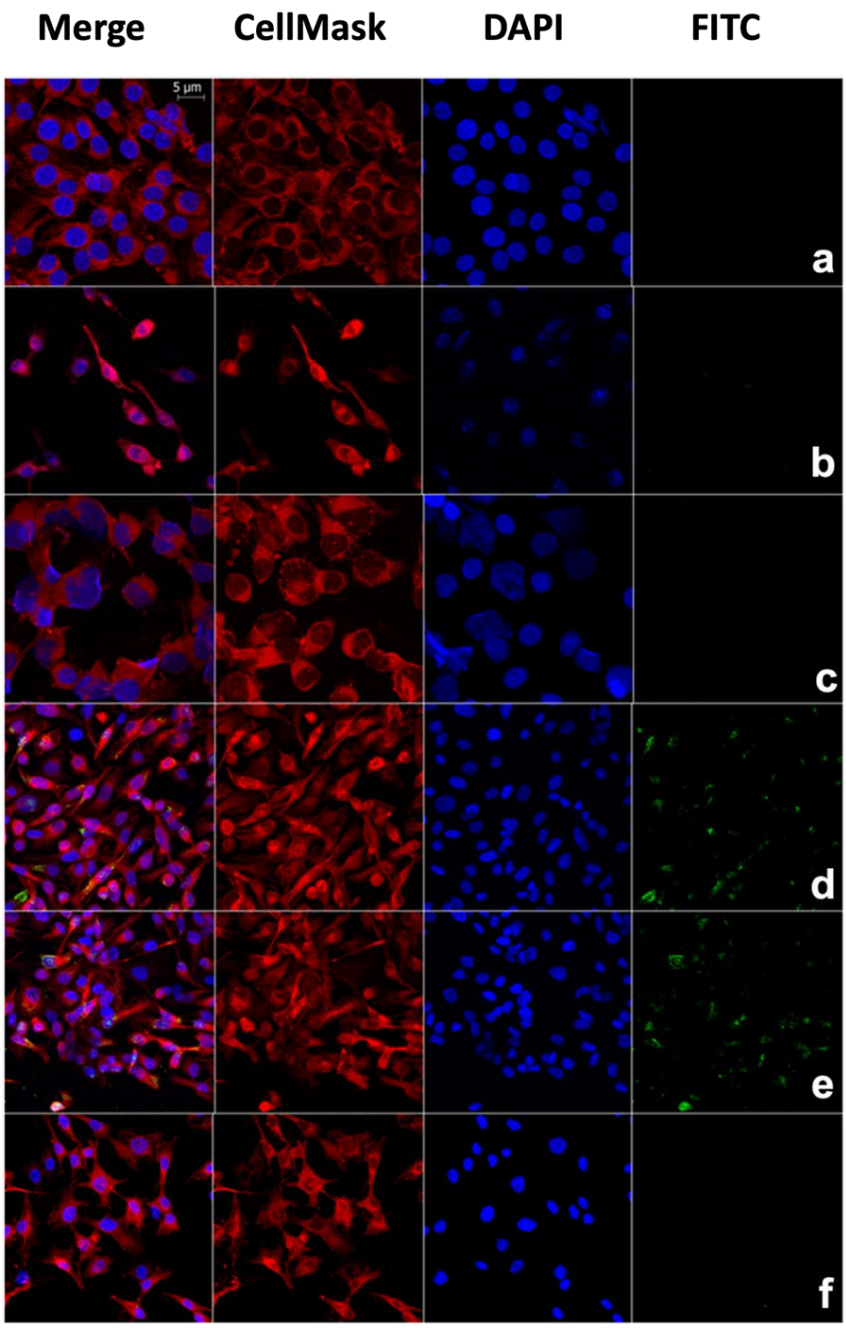

Figure 27 Confocal microscope photographs of SK-OV3 cells after 24 h of growth in DMEM medium low glucose containing scrambled PNA (a), antisense PNA (b), OAd (c), OAd:antisense PNA (d), OAd:scrambled PNA (e) and 1X PBS (f).

The necessity of developing a novel anti-PD-L1 strategy to perform an anticancer activity aimed at the construction of a viral platform for the delivery of an anti-PD-L1 PNA.
The challenging selection of target sequence assured the specificity of the interaction between the ASO PNA strand, and the mRNA region identified. In silico studies were meant to predict the ASO ongoings in vitro, avoiding undesired side reactions that could prevent the hybridization process pivotal for the antisense response.
The step of functionalization was performed to assess the oncolytic Adenoviral carrier complexation with the synthesized PNA allowing to set the best fitting parameters to obtain a functional delivery support. The lowest amount of PNA was loaded on the viral surface (10 equiv.), differing from previous papers, by shortening the cytotoxicity of the treatment.
The successful viability tests and uptake studies permitted further biological investigation by directly measuring the protein expression after the treatment with the functionalized Oncolytic Adenoviruses. The flow cytometry measurements, after 48h of treatment, recorded a negative modulation of PD-L1 protein due to the antisense PNA effect after its delivery. Hence, the specificity of the antisense PNA activity was confirmed by comparing the PD-L1 expression in cells treated with a delivered scrambled PNA to corroborate the sequence dependent mechanism of action. The cell treatments with the oncolytic Adenovirus and with undelivered PNAs were used as controls, the collected data confirmed the down-modulating effect only of the Antisense PNA. The delivery platform developed assessed the increased efficacy of the delivered antisense PNA compared to the undelivered one in SK-OV3 cell line. Moreover, the A549 cell line treated with the functionalized OAd revealed the impossibility of evaluating the downregulation of the protein target due to the low level of PD-L1 expressed in infected cells, demonstrating to act with a specific tissue response. Considering that the lack of tissue specificity represents one of the most weakness of anti-PD-L1 treatment based on monoclonal antibody, the ability of regulating the protein expression in a selective mode encourage to further study this delivery platform. Most of all the cell localization by confocal microscopy of the delivered PNA confirmed the PNA releasing in the cytoplasmatic cell compartment for each OAd complex supporting the successful and specific antisense mechanism occurrence.

Experimental Section

Synthesis of PNA

Antisense PNA, scrambled PNA, FITC antisense PNA, and FITC scrambled PNA (Table 1) were synthesized using the 9-fluorenylmethoxycarbonyl (Fmoc) solid-phase strategy. Briefly, 50 mg of 4-methylbenzhydrylamine (MBHA) resin (0.5 mmol/g) was treated with a solution of 20% piperidine in DMF for 10 min after a swelling step in CH2Cl2 for 30 min and dimethylformamide (DMF) washings. We proceeded with washings in DMF (5×). Then six couplings with Fmoc-L-Lys (MMt)-OH (MMT = monomethoxytrityl) for all PNA sequences were performed using the following conditions: 3 Equiv FmocLys monomer in N-methyl-2-pyrrolidone (NMP) 0.2 M, 3 Equiv 3-oxid hexafluorophosphate (HATU) in DMF 0.2 M; 3 Equiv. N,N-diisopropylethylamine (DIPEA)/5.5 Equiv. lutidine for 10 min at room temperature (RT). PNA monomers were then reacted as here reported: 3 equiv. Monomer building block in NMP 0.2 M, 3 Equiv. HATU in DMF 0.2 M and 3 equiv. DIPEA/ 5 equiv. lutidine, 10 min at RT. The coupling steps were succeeded by acetylation phases performed with a DMF solution with 20 % of Ac2O in the presence of pyridine for 10 min at RT just before the Fmoc group removal with a 20% piperidine solution (10 min).
FITC labeled PNAs were synthesized as already described for the unlabeled compound but three additional coupling steps after the last PNA monomer were performed. We proceeded by reacting the elongated chain with 5 equiv. AEEA Linker-Fmoc in NMP 0.2M, 5 equiv. HATU in DMF 0.2M and 5 equiv. DIPEA/ 7.5 equiv. lutidine, 1h at RT, for each AEEA Linker. As mentioned, the coupling step was followed by the capping and deblock step.
The last coupling step was performed by dissolving 5 equiv Fluorescein Isothiocyanate (FITC) in DMF 0.2 M, over-night in dark at RT. The coupling step was followed by several washings with DMF solvent. PNA and FITC PNA were dethatched from the solid support by treatment with trifluoroacetic acid (TFA)/anisole/ethanedithiol (9:1:1; v/v/v) for 4 h and the products were precipitated with cold diethyl ether. The precipitates were collected by centrifugation, flushed twice with diethyl ether, solubilized in water, and finally lyophilized. The PNAs were obtained with a 48−50% overall yield (95% medium yield for each coupling estimated by Fmoc spectrophotometric measurements). The crude

samples were purified by semipreparative HPLC analyses on a Jasco (Easton, MD, USA) PU-2089 Plus pump equipped with a Jasco UV-2075 Plus UV detector using a 10 × 250 mm C-18 reverse-phase column (particle size 5 μm) with a continuous gradient of CH3CN in H2O, 0.1% (v/v) TFA in both mobile phases, from 0% to 100% in 60 min, flow 3 mL/min. The collected fractions were lyophilized. The amount of each PNA sample dissolved in pure water was estimated by quantitative UV with a Jasco V-530 spectrophotometer (λ = 220−310 nm, 400 nm/min scanning speed, 2.0 nm bandwidth) assuming the following molar extinction coefficients ε = 177,3 cm −1 mM −1 for ANTISENSE PNA, SCRAMBLED PNA, FITC ANTISENSE PNA and FITC SCRAMBLED PNA. The final pure products were characterized by ESI-MS. ANTISENSE PNA and SCRAMBLED PNA: ESI-MS (m/z) calcd. for [M + 4H] 4+ 1384.3, found 1384.3; calcd. for [M + 5H] 5+ 1107.7 found 1107.7; calcd. for [M + 6H] 6+ 923.3 found 923.4 (Figure S7).
FITC ANTISENSE PNA and FITC SCRAMBLED PNA: ESI-MS (m/z) calcd. for [M + 5H] 5+ 1243.54, found 1244.4; calcd. for [M + 6H] +6 1036.44, found 1037.3.

Functionalization protocol and characterization of the complex with Zeta Potential and Dynamic Light Scattering (DLS) Analysis.

We previously quantified the viral protein content by performing the protein quantitative Bradford assay that affects the binding of Coomassie Brilliant Blue G-250 dye to proteins (Bradford 1976) concerning its representative forms: Cationic (red), neutral (green), and anionic (blue) (Compton and Jones 1985). This blue protein-dye form is detectable at 595 nm in the assay using a spectrophotometer and permits the final quantification of the protein dissolved in the solution. As soon as the OAd stock was quantified, the functionalization step was performed by mixing and agitating 10, 50 and 100 equiv. of PNA with 1 equiv. of OAd in 0,1 mL of Milli-Q water for 15 minutes at room temperature before diluting the complex to a final volume of 0,7 mL with sterile Milli-Q water adjusted to pH 7.4 and transferred to a polystyrene disposable cuvette for DLS analysis. Subsequently, the samples were moved from the cuvette to a DTS1070 disposable capillary cell (Malvern, Worcestershire, UK) for zeta potential measurements, which were performed at 25 °C using a Malvern Zetasizer Nano ZS system.

Cell lines

A549 (human lung carcinoma), SK-OV3 (ovarian cancer) cells in 10% of fetal bovine serum (FBS) low glucose (1000mg/L) Dulbecco's Modified Eagle's Medium (DMEM), supplemented with 1% of penicillin-streptomycin, 1% of L-glutamine, and 1% of non-essential amino acids. All the cell lines treated were incubated at +37°C and 5% of CO2 in the incubator.

Cell viability assay

The cells (A549 and SK-OV3) were seeded in 96-well plates with a concentration of 1×104 cells per well in 10% of FBS low glucose DMEM. Before the complete seeding, the cells were infected with the virus, and we tested the following range of analysis: 0,1-1-10-100-1000 Viral Particles per cell (VPs/cell) for 48,72 hours and 120h. MTS Assay Kit then measured cytotoxicity levels according to the producer protocol (Cell Titer 96 AQueous One Solution Cell Proliferation Assay; Promega, Nacka, Sweden). Spectrophotometric data was read using the Varioskan LUXMultimode Reader (Thermo Scientific, Carlsbad, C, USA).

Quantitative Flowcytometry (FCM) analysis

The PNA modulation of PD-L1 was verified by quantification of the expression of the protein on the cell membrane by FCM. As performed elsewhere, 1×106 cells were seeded in 6-well plates and then stored at 37°C for 2 h before the treatment. The cells were then infected with OAd, OAd:PNA complexes considering 0.1, 1, 10, 100, 1000 VPs/cell and were also treated with PNAs by adding the same amount of PNA required for the OAd complexes (10 equiv.), subsequently stored at 37°C in the incubator for 48 h. After two days, the samples were removed from the wells. Then, we washed the wells three times with PBS. The cells were detached from the wells with a scraper, transferred to a v-bottom 96 well plate, and centrifuged at 500g in an Eppendorf R5100 centrifuge for 5 minutes. After removing the supernatant, the cells were resuspended in 100 µL of Antibody solution for each sample except for the blanks (2µL APC anti-human CD274 plus 98µL of PBS). We added 100 µL of PBS to the blank wells. The cells were then incubated on the ice at +4°C for 20 minutes. The cells were washed three times with cold

PBS, resuspended in 200 µL of cold PBS, and analyzed with a BD Accuri flow cytometer equipped with C6 autosampler (BD Biosciences, USA). The data were then analyzed with Flow.jo software to quantify the geometric mean fluorescence intensity (gMFI) and the APC or PE positive cell percentage.

Qualitative flow cytometry and confocal microscopy analysis

Flow cytometry (FCM) measured the quantitative cellular uptake on a BD Accuri cytometer equipped with a C6 autosampler (BD Biosciences, USA). The samples were tagged by adding a labeling FITC residue at the PNA amino terminal during the manual synthesis. 1×106 cells were seeded in 6-well plates stored at 37°C in the incubator for 2h before proceeding with the treatment. The complexes OAd/PNAs were added, and the cells were rinsed twice with 1X phosphate saline buffer (PBS) at pH 7.4. After 24 h from the infection, the cells were detached from the plate with a scraper, resuspended in cold PBS, and transferred to a 96-well V bottom plate (Corning, USA). We centrifuged the cells at 500g for 5 min in inserire specifiche strumento. Samples were washed three times with cold PBS; then, the cells were resuspended in 200 µL of cold PBS. The data were then analyzed with Flow.jo software to quantify the percentage of FITC-positive cells.
SK-OV3 cell line was further analyzed by confocal microscopy. The Leica SP8 inverted microscope (Leica Microsystems, Germany confocal microscopy) was used for the experiment. We seeded 5×104 cells into 8-well chambers (Lab Tek, Thermo Fisher Scientific, USA) and we placed the chambers back in the incubator for 2 h and before of complete attachment the PNAs, OAd, and OAd:PNA complexes were added to the corresponding well in the 100 VP/cell concentration. The samples were then incubated for 24 h. The samples were removed from the wells and the wells were washed twice with PBS. Then, we stained the cells with Cell Mask Deep Red (Thermo Fisher, USA), followed by fixation with 4% paraformaldehyde (Sigma Aldrich, USA). The nuclei were then stained with 4’,6-diamidino-2-phenylindole (DAPI) (Thermo Fisher, USA). Finally, we washed the wells for 4 times with PBS. Each well was filled with 200 µL of PBS for the imaging. The images were processed with Leica LASX Software (Leica Microsystems, Germany).

Statistical analysis

Results of the assays are expressed as mean ± standard deviation (s.d.) of three independent experiments. Results were evaluated by means of one-way analysis of variance (ANOVA) with the level of significance set at probabilities of *p< 0.05, **p< 0.01, and ***p< 0.001 using Origin 8.6 (Origin Lab Corp., USA).

Conclusion

The necessity of developing a novel anti-PD-L1 strategy to perform an anticancer activity aimed at the construction of a viral platform for the delivery of an anti-PD-L1 PNA.

The challenging selection of target sequence assured the specificity of the interaction between the ASO PNA strand, and the mRNA region identified. In silico studies were meant to predict the ASO ongoings in vitro, avoiding undesired side reactions that could prevent the hybridization process pivotal for the antisense response.

The step of functionalization was performed to assess the oncolytic Adenoviral carrier complexation with the synthesized PNA allowing to set the best fitting parameters to obtain a functional delivery support. The lowest amount of PNA was loaded on the viral surface (10 equiv.), differing from previous papers, by shortening the cytotoxicity of the treatment.

The successful viability tests and uptake studies permitted further biological investigation by directly measuring the protein expression after the treatment with the functionalized Oncolytic Adenoviruses. The flow cytometry measurements, after 48h of treatment, recorded a negative modulation of PD-L1 protein due to the antisense PNA effect after its delivery. Hence, the specificity of the antisense PNA activity was confirmed by comparing the PD-L1 expression in cells treated with a delivered scrambled PNA to corroborate the sequence dependent mechanism of action. The cell treatments with the oncolytic Adenovirus and with undelivered PNAs were used as controls, the collected data confirmed the down-modulating effect only of the Antisense PNA. The delivery platform developed assessed the increased efficacy of the delivered antisense PNA compared to the undelivered one in SK-OV3 cell line. Moreover, the A549 cell line treated with the functionalized OAd revealed the impossibility of evaluating the downregulation of the protein target due to the low level of PD-L1 expressed in infected cells,

demonstrating to act with a specific tissue response. Considering that the lack of tissue specificity represents one of the most weakness of anti-PD-L1 treatment based on monoclonal antibody, the ability of regulating the protein expression in a selective mode encourage to further study this delivery platform. Most of all the cell localization by confocal microscopy of the delivered PNA confirmed the PNA releasing in the cytoplasmatic cell compartment for each OAd complex supporting the successful and specific antisense mechanism occurrence.

References

(1) Koppelhus, U.; Nielsen, P. E. *C Ellular Delivery of Peptide Nucleic Acid (PNA)*; 2003; Vol. 55.

(2) Ray, A.; Nordén, B. Peptide Nucleic Acid (PNA): Its Medical and Biotechnical Applications and Promise for the Future. *The FASEB Journal* **2000**, *14* (9), 1041–1060. https://doi.org/10.1096/fasebj.14.9.1041.

(3) Avitabile, C.; Moggio, L.; D'Andrea, L. D.; Pedone, C.; Romanelli, A. Development of an Efficient and Low-Cost Protocol for the Manual PNA Synthesis by Fmoc Chemistry. *Tetrahedron Lett* **2010**, *51* (29), 3716–3718. https://doi.org/10.1016/j.tetlet.2010.05.026.

(4) Volpi, S.; Cancelli, U.; Neri, M.; Corradini, R. Multifunctional Delivery Systems for Peptide Nucleic Acids. *Pharmaceuticals*. MDPI AG December 1, 2021, pp 1–31. https://doi.org/10.3390/ph14010014.

(5) Suparpprom, C.; Vilaivan, T. Perspectives on Conformationally Constrained Peptide Nucleic Acid (PNA): Insights into the Structural Design, Properties and Applications. *RSC Chemical Biology*. Royal Society of Chemistry March 18, 2022, pp 648–697. https://doi.org/10.1039/d2cb00017b.

(6) Nabhan, C.; Rosen, S. T. Chronic Lymphocytic Leukemia: A Clinical Review. *JAMA - Journal of the American Medical Association* **2014**, *312* (21), 2265–2276. https://doi.org/10.1001/jama.2014.14553.

(7) Bosch, F.; Dalla-Favera, R. Chronic Lymphocytic Leukaemia: From Genetics to Treatment. *Nat Rev Clin Oncol* **2019**, *16* (11), 684–701. https://doi.org/10.1038/s41571-019-0239-8.

(8) Starostka, D.; Kriegova, E.; Kudelka, M.; Mikula, P.; Zehnalova, S.; Radvansky, M.; Papajik, T.; Kolacek, D.; Chasakova, K.; Talianova, H. Quantitative Assessment of Informative Immunophenotypic Markers Increases the Diagnostic Value of Immunophenotyping in Mature CD5-Positive B-Cell Neoplasms. *Cytometry B Clin Cytom* **2018**, *94* (4), 576–587. https://doi.org/10.1002/cyto.b.21607.

(9) Friedman, D. R.; Guadalupe, E.; Volkheimer, A.; Moore, J. O.; Weinberg, J. B. Clinical Outcomes in Chronic Lymphocytic Leukaemia Associated with Expression of CD5, a Negative Regulator of B-Cell Receptor Signalling. *Br J Haematol* **2018**, *183* (5), 747–754. https://doi.org/10.1111/bjh.15632.
(10) Jaseb, K.; Purrahman, D.; Shahrabi, S.; Ghanavat, M.; Rezaeean, H.; Saki, N. Prognostic Significance of Aberrant CD5 Expression in B-Cell Leukemia. *Oncol Rev* **2019**, *13* (1), 77–82. https://doi.org/10.4081/oncol.2019.400.
(11) Crisci, T.; Falanga, A. P.; Casalino, M.; Borbone, N.; Terracciano, M.; Chianese, G.; Gioffrè, M.; D'Errico, S.; Marzano, M.; Rea, I.; De Stefano, L. De; Oliviero, G. Bioconjugation of a PNA Probe to Zinc Oxide Nanowires for Label-Free Sensing. *Nanomaterials* **2021**, *11* (2), 523. https://doi.org/10.3390/nano11020523.
(12) Gary-Gouy, H.; Harriague, J.; Bismuth, G.; Platzer, C.; Schmitt, C.; Dalloul, A. H. Human CD5 Promotes B-Cell Survival through Stimulation of Autocrine IL-10 Production. *Blood* **2002**, *100* (13), 4537–4543. https://doi.org/10.1182/blood-2002-05-1525.
(13) Gary-Gouy, H.; Harriague, J.; Dalloul, A.; Donnadieu, E.; Bismuth, G. CD5-Negative Regulation of B Cell Receptor Signaling Pathways Originates from Tyrosine Residue Y429 Outside an Immunoreceptor Tyrosine-Based Inhibitory Motif. *The Journal of Immunology* **2002**, *168* (1), 232–239. https://doi.org/10.4049/jimmunol.168.1.232.
(14) Pers, J.; Berthou, C.; Porakishvili, N.; Burdjanadze, M.; Le Calvez, G.; Abgrall, J.; Lydyard, P.; Youinou, P.; Jamin, C. CD5-Induced Apoptosis of B Cells in Some Patients with Chronic Lymphocytic Leukemia. *Leukemia* **2002**, *16* (1), 44–52. https://doi.org/10.1038/sj.leu.2402327.
(15) Gary-Gouy, H.; Sainz-Perez, A.; Marteau, J.-B.; Marfaing-Koka, A.; Delic, J.; Merle-Beral, H.; Galanaud, P.; Dalloul, A. Natural Phosphorylation of CD5 in Chronic Lymphocytic Leukemia B Cells and Analysis of CD5-Regulated Genes in a B Cell Line Suggest a Role for CD5 in Malignant Phenotype. *The Journal of Immunology* **2007**, *179* (7), 4335–4344. https://doi.org/10.4049/jimmunol.179.7.4335.
(16) Loisel, S.; André, P. A.; Golay, J.; Buchegger, F.; Kadouche, J.; Cérutti, M.; Bologna, L.; Kosinski, M.; Viertl, D.; Delaloye, A. B.; Berthou, C.; Mach, J. P.; Boumsell, L. Antitumour Effects of Single or Combined Monoclonal Antibodies Directed against Membrane Antigens Expressed by Human B Cells Leukaemia. *Mol Cancer* **2011**, *10*, 1–12. https://doi.org/10.1186/1476-4598-10-42.

(17) Klitgaard, J. L.; Koefoed, K.; Geisler, C.; Gadeberg, O. V.; Frank, D. A.; Petersen, J.; Jurlander, J.; Pedersen, M. W. Combination of Two Anti-CD5 Monoclonal Antibodies Synergistically Induces Complement-Dependent Cytotoxicity of Chronic Lymphocytic Leukaemia Cells. *Br J Haematol* **2013**, *163* (2), 182–193. https://doi.org/10.1111/bjh.12503.

(18) Mologni, L.; Marchesi, E.; Nielsen, P. E.; Gambacorti-Passerini, C. Inhibition of Promyelocytic Leukemia (PML)/Retinoic Acid Receptor-α and PML Expression in Acute Promyelocytic Leukemia Cells by Anti-PML Peptide Nucleic Acid. *Cancer Res* **2001**, *61* (14), 5468–5473.

(19) Egholm, M.; Buchardt, O.; Christensen, L.; Behrens, C.; Freier, S. M.; Driver, D. A.; Berg, R. H.; Kim, S. K.; Norden, B.; Nielsen, P. E. PNA Hybridizes to Complementary Oligonucleotides Obeying the Watson-Crick Hydrogen-Bonding Rules. *Nature* **1993**, *365* (6446), 566–568. https://doi.org/10.1038/365566a0.

(20) Ganesh, K. N.; Nielsen, P. E. Peptide Nucleic Acids : Analogs and Derivatives. *Curr Org Chem* **2000**, *4*, 931–943.

(21) Montazersaheb, S.; Hejazi, M. S.; Nozad Charoudeh, H. Potential of Peptide Nucleic Acids in Future Therapeutic Applications. *Adv Pharm Bull* **2018**, *8* (4), 551–563. https://doi.org/10.15171/apb.2018.064.

(22) Ghavami; Shiraishi; Nielsen. Cooperative Cellular Uptake and Activity of Octaarginine Antisense Peptide Nucleic Acid (PNA) Conjugates. *Biomolecules* **2019**, *9* (10), 554. https://doi.org/10.3390/biom9100554.

(23) Fabbri, E.; Tamanini, A.; Jakova, T.; Gasparello, J.; Manicardi, A.; Corradini, R.; Finotti, A.; Borgatti, M.; Lampronti, I.; Munari, S.; Dechecchi, M. C.; Cabrini, G.; Gambari, R. Treatment of Human Airway Epithelial Calu-3 Cells with a Peptide-Nucleic Acid (PNA) Targeting the MicroRNA MiR-101-3p Is Associated with Increased Expression of the Cystic Fibrosis Transmembrane Conductance Regulator () Gene. *Eur J Med Chem* **2021**, *209*, 112876. https://doi.org/10.1016/j.ejmech.2020.112876.

(24) Gasparello, J.; Papi, C.; Gambari, R.; Finotti, A.; Gambari, L.; Rozzi, A.; Manicardi, A.; Corradini, R. High Levels of Apoptosis Are Induced in the Human Colon Cancer HT-29 Cell Line by Co-Administration of Sulforaphane and a Peptide Nucleic Acid Targeting MiR-15b-5p. *Nucleic Acid Ther* **2020**, *30* (3), 164–174. https://doi.org/10.1089/nat.2019.0825.

(25) Amato, F.; Tomaiuolo, R.; Borbone, N.; Elce, A.; Amato, J.; D'Errico, S.; De Rosa, G.; Mayol, L.; Piccialli, G.; Oliviero, G.; Castaldo, G. Design, Synthesis and Biochemical Investigation, by in Vitro Luciferase Reporter System, of Peptide Nucleic Acids as New Inhibitors of MiR-509-3p Involved in the Regulation of Cystic Fibrosis Disease-Gene Expression. *Med. Chem. Commun.* **2014**, *5* (1), 68–71. https://doi.org/10.1039/C3MD00257H.

(26) Amato, J.; Pagano, B.; Borbone, N.; Oliviero, G.; Gabelica, V.; Pauw, E. De; D'Errico, S.; Piccialli, V.; Varra, M.; Giancola, C.; Piccialli, G.; Mayol, L. Targeting G-Quadruplex Structure in the Human c-Kit Promoter with Short PNA Sequences. *Bioconjug Chem* **2011**, *22* (4), 654–663. https://doi.org/10.1021/bc100444v.

(27) Falanga, A. P.; Cerullo, V.; Marzano, M.; Feola, S.; Oliviero, G.; Piccialli, G.; Borbone, N. Peptide Nucleic Acid-Functionalized Adenoviral Vectors Targeting G-Quadruplexes in the P1 Promoter of Bcl-2 Proto-Oncogene: A New Tool for Gene Modulation in Anticancer Therapy. *Bioconjug Chem* **2019**, *30* (3), 572–582. https://doi.org/10.1021/acs.bioconjchem.8b00674.

(28) Comegna, M.; Conte, G.; Falanga, A. P.; Marzano, M.; Cernera, G.; Di Lullo, A. M.; Amato, F.; Borbone, N.; D'Errico, S.; Ungaro, F.; D'Angelo, I.; Oliviero, G.; Castaldo, G. Assisting PNA Transport through Cystic Fibrosis Human Airway Epithelia with Biodegradable Hybrid Lipid-Polymer Nanoparticles. *Sci Rep* **2021**, *11* (1), 6393. https://doi.org/10.1038/s41598-021-85549-z.

(29) Montano, G.; Vidovic, K.; Palladino, C.; Cesaro, E.; Sodaro, G.; Quintarelli, C.; Angelis, B. De; Errichiello, S.; Pane, F.; Izzo, P.; Grosso, M.; Gullberg, U.; Costanzo, P. WT1-Mediated Repression of the Proapoptotic Transcription Factor ZNF224 Is Triggered by the BCR-ABL Oncogene. *Oncotarget* **2015**, *6* (29), 28223–28237. https://doi.org/10.18632/oncotarget.4950.

(30) Hirohata, S.; Jelinek, D. F.; Lipsky, P. E. T Cell-Dependent Activation of B Cell Proliferation and Differentiation by Immobilized Monoclonal Antibodies to CD3. *J Immunol* **1988**, *140* (11), 3736–37344.

(31) Lipsky, P. E. The Induction of Human B-Cell Activation, Proliferation and Differentiation by Anti-CD3-Stimulated T Cells--a Model of T Cell/B Cell Collaboration. *Res immunol* **1990**, *141*, 424–427.

(32) Riccio, P.; Sessa, R.; de Nicola, S.; Petruzziello, F.; Trombetti, S.; Menna, G.; Pepe, G.; Maddalena, P.; Izzo, P.; Grosso, M. GATA-1 Isoforms Differently Contribute to the Production and Compartmentation of Reactive Oxygen Species in the Myeloid

Leukemia Cell Line K562. *J Cell Physiol* **2019**, *234* (11), 20829–20846. https://doi.org/10.1002/jcp.28688.
(33) Sodaro, G.; Blasio, G.; Fiorentino, F.; Auberger, P.; Costanzo, P.; Cesaro, E. ZNF224 Is a Transcriptional Repressor of AXL in Chronic Myeloid Leukemia Cells. *Biochimie* **2018**, *154*, 127–131. https://doi.org/10.1016/j.biochi.2018.08.011.
(34) Cesaro, E.; Pastore, A.; Polverino, A.; Manna, L.; Divisato, G.; Quintavalle, C.; Sanzo, M. Di; Faniello, M. C.; Grosso, M.; Costanzo, P. ZNF224 Is a Mediator of TGF-β pro-Oncogenic Function in Melanoma. *Hum Mol Genet* **2021**, *00* (00), 1–10. https://doi.org/10.1093/hmg/ddab173.
(35) Sodaro, G.; Cesaro, E.; Montano, G.; Blasio, G.; Fiorentino, F.; Romano, S.; Jacquel, A.; Aurberger, P.; Costanzo, P. Role of ZNF224 in C-Myc Repression and Imatinib Responsiveness in Chronic Myeloid Leukemia. *Oncotarget* **2018**, *9* (3), 3417–3431. https://doi.org/10.18632/oncotarget.23283.
(36) Kilså Jensen, K.; Ørum, H.; Nielsen, P. E.; Nordén, B. Kinetics for Hybridization of Peptide Nucleic Acids (PNA) with DNA and RNA Studied with the BIAcore Technique. *Biochemistry* **1997**, *36* (16), 5072–5077. https://doi.org/10.1021/bi9627525.
(37) Mergny, J.; Li, J.; Lacroix, L.; Amrane, S.; Chaires, J. B. Thermal Difference Spectra : A Specific Signature for Nucleic Acid Structures. *Nucleic Acids Res* **2005**, *33* (16), 1–6. https://doi.org/10.1093/nar/gni134.
(38) Rosén, A.; Bergh, A.-C.; Gogok, P.; Evaldsson, C.; Myhrinder, A. L.; Hellqvist, E.; Rasul, A.; Björkholm, M.; Jansson, M.; Mansouri, L.; Liu, A.; Teh, B. T.; Rosenquist, R.; Klein, E. Lymphoblastoid Cell Line with B1 Cell Characteristics Established from a Chronic Lymphocytic Leukemia Clone by in Vitro EBV Infection. *Oncoimmunology* **2012**, *1* (1), 18–27. https://doi.org/10.4161/onci.1.1.18400.
(39) Hertlein, E.; Beckwith, K. A.; Lozanski, G.; Chen, T. L.; Towns, W. H.; Johnson, A. J.; Lehman, A.; Ruppert, A. S.; Bolon, B.; Andritsos, L.; Lozanski, A.; Rassenti, L.; Zhao, W.; Jarvinen, T. M.; Senter, L.; Croce, C. M.; Symer, D. E.; de la Chapelle, A.; Heerema, N. A.; Byrd, J. C. Characterization of a New Chronic Lymphocytic Leukemia Cell Line for Mechanistic In Vitro and In Vivo Studies Relevant to Disease. *PLoS One* **2013**, *8* (10), e76607. https://doi.org/10.1371/journal.pone.0076607.
(40) Goltermann, L.; Nielsen, P. E. PNA Antisense Targeting in Bacteria: Determination of Antibacterial Activity (MIC) of PNA-Peptide

Conjugates. In *Methods in molecular biology (Clifton, N.J.)*; 2020; Vol. 2105, pp 231–239. https://doi.org/10.1007/978-1-0716-0243-0_14.
(41) *https://www.who.int*. https://www.who.int (accessed 2022-04-21).
(42) van der Meel, R.; Sulheim, E.; Shi, Y.; Kiessling, F.; Mulder, W. J. M.; Lammers, T. Smart Cancer Nanomedicine. *Nat Nanotechnol* **2019**, *14* (11). https://doi.org/10.1038/s41565-019-0567-y.
(43) Li, D.; Zhang, R.; Liu, G.; Kang, Y.; Wu, J. Redox-Responsive Self-Assembled Nanoparticles for Cancer Therapy. *Advanced Healthcare Materials*. 2020. https://doi.org/10.1002/adhm.202000605.
(44) Medicina, B. A.-; 2019, undefined. Tumor Microenvironment. *mdpi.com*. https://doi.org/10.3390/medicina56010015.
(45) Guo, X.; Cheng, Y.; Zhao, X.; Luo, Y.; Chen, J.; Yuan, W. E. Advances in Redox-Responsive Drug Delivery Systems of Tumor Microenvironment. *Journal of Nanobiotechnology*. BioMed Central Ltd. September 22, 2018. https://doi.org/10.1186/s12951-018-0398-2.
(46) Mollazadeh, S.; Mackiewicz, M.; Yazdimamaghani, M. Recent Advances in the Redox-Responsive Drug Delivery Nanoplatforms: A Chemical Structure and Physical Property Perspective. *Materials Science and Engineering C*. Elsevier Ltd January 1, 2021. https://doi.org/10.1016/j.msec.2020.111536.
(47) Rabiee, N.; Khatami, M.; Jamalipour Soufi, G.; Fatahi, Y.; Iravani, S.; Varma, R. S. Diatoms with Invaluable Applications in Nanotechnology, Biotechnology, and Biomedicine: Recent Advances. *ACS Biomaterials Science and Engineering*. 2021. https://doi.org/10.1021/acsbiomaterials.1c00475.
(48) Rea, I.; Terracciano, M.; de Stefano, L. Synthetic vs Natural: Diatoms Bioderived Porous Materials for the Next Generation of Healthcare Nanodevices. *Advanced Healthcare Materials*. Wiley-VCH Verlag February 8, 2017. https://doi.org/10.1002/adhm.201601125.
(49) Terracciano, M.; Shahbazi, M. A.; Correia, A.; Rea, I.; Lamberti, A.; de Stefano, L.; Santos, H. A. Surface Bioengineering of Diatomite Based Nanovectors for Efficient Intracellular Uptake and Drug Delivery. *Nanoscale* **2015**, *7* (47), 20063–20074. https://doi.org/10.1039/c5nr05173h.
(50) Tramontano, C.; Chianese, G.; Terracciano, M.; de Stefano, L.; Rea, I. Nanostructured Biosilica of Diatoms: From Water World to

Biomedical Applications. *Applied Sciences (Switzerland)*. MDPI AG October 1, 2020. https://doi.org/10.3390/app10196811.

(51) Martucci, N. M.; Migliaccio, N.; Ruggiero, I.; Albano, F.; Calì, G.; Romano, S.; Terracciano, M.; Rea, I.; Arcari, P.; Lamberti, A. Nanoparticle-Based Strategy for Personalized B-Cell Lymphoma Therapy. *Int J Nanomedicine* **2016**, *11*, 6089–6101. https://doi.org/10.2147/IJN.S118661.

(52) Terracciano, M.; de Stefano, L.; Rea, I. Diatoms Green Nanotechnology for Biosilica-Based Drug Delivery Systems. *Pharmaceutics*. 2018. https://doi.org/10.3390/pharmaceutics10040242.

(53) Rea, I.; Martucci, N. M.; de Stefano, L.; Ruggiero, I.; Terracciano, M.; Dardano, P.; Migliaccio, N.; Arcari, P.; Taté, R.; Rendina, I.; Lamberti, A. Diatomite Biosilica Nanocarriers for SiRNA Transport inside Cancer Cells. *Biochim Biophys Acta Gen Subj* **2014**, *1840* (12), 3393–3403. https://doi.org/10.1016/j.bbagen.2014.09.009.

(54) Managò, S.; Migliaccio, N.; Terracciano, M.; Napolitano, M.; Martucci, N.; de Stefano, L.; Rendina, I.; de Luca, A. C.; Lamberti, A.; Rea, I. Diatomite Nanovectors Uptake in Cancer Cells: A Raman Imaging Study; 2018. https://doi.org/10.1117/12.2315371.

(55) Managò, S.; Tramontano, C.; Delle Cave, D.; Chianese, G.; Zito, G.; de Stefano, L.; Terracciano, M.; Lonardo, E.; de Luca, A. C.; Rea, I. SERS Quantification of Galunisertib Delivery in Colorectal Cancer Cells by Plasmonic-Assisted Diatomite Nanoparticles. *Small* **2021**, *17* (34). https://doi.org/10.1002/smll.202101711.

(56) Sharma, C.; Awasthi, S. K. Versatility of Peptide Nucleic Acids (PNAs): Role in Chemical Biology, Drug Discovery, and Origins of Life. *Chemical Biology and Drug Design*. 2017. https://doi.org/10.1111/cbdd.12833.

(57) Saadati, A.; Hassanpour, S.; Guardia, M. de la; Mosafer, J.; Hashemzaei, M.; Mokhtarzadeh, A.; Baradaran, B. Recent Advances on Application of Peptide Nucleic Acids as a Bioreceptor in Biosensors Development. *TrAC - Trends in Analytical Chemistry*. 2019. https://doi.org/10.1016/j.trac.2019.02.030.

(58) Shen, T.; Zhang, Y.; Zhou, S.; Lin, S.; Zhang, X. B.; Zhu, G. Nucleic Acid Immunotherapeutics for Cancer. *ACS Appl Bio Mater* **2020**, *3* (5). https://doi.org/10.1021/acsabm.0c00101.

(59) Moretta, R.; Terracciano, M.; Rea, I.; de Stefano, L. Bioconjugation of Peptides to Hybrid Gold Nanoparticles. In *Methods in Molecular Biology*; 2021; Vol. 2355. https://doi.org/10.1007/978-1-0716-1617-8_10.

(60) Gasparello, J.; Manicardi, A.; Casnati, A.; Corradini, R.; Gambari, R.; Finotti, A.; Sansone, F. Efficient Cell Penetration and Delivery of Peptide Nucleic Acids by an Argininocalix[4]Arene. *Sci Rep* **2019**, *9* (1). https://doi.org/10.1038/s41598-019-39211-4.
(61) Tahmasbi Rad, A.; Malik, S.; Yang, L.; Oberoi-Khanuja, T. K.; Nieh, M. P.; Bahal, R. A Universal Discoidal Nanoplatform for the Intracellular Delivery of PNAs. *Nanoscale* **2019**, *11* (26). https://doi.org/10.1039/c9nr03667a.
(62) Comegna, M.; Conte, G.; Falanga, A. P.; Marzano, M.; Cernera, G.; di Lullo, A. M.; Amato, F.; Borbone, N.; D'Errico, S.; Ungaro, F.; d'Angelo, I.; Oliviero, G.; Castaldo, G. Assisting PNA Transport through Cystic Fibrosis Human Airway Epithelia with Biodegradable Hybrid Lipid-Polymer Nanoparticles. *Sci Rep* **2021**, *11* (1). https://doi.org/10.1038/s41598-021-85549-z.
(63) Falanga, A. P.; Cerullo, V.; Marzano, M.; Feola, S.; Oliviero, G.; Piccialli, G.; Borbone, N. Peptide Nucleic Acid-Functionalized Adenoviral Vectors Targeting G-Quadruplexes in the P1 Promoter of Bcl-2 Proto-Oncogene: A New Tool for Gene Modulation in Anticancer Therapy. *Bioconjug Chem* **2019**, *30* (3). https://doi.org/10.1021/acs.bioconjchem.8b00674.
(64) Blank, C.; Mackensen, A. Contribution of the PD-L1/PD-1 Pathway to T-Cell Exhaustion: An Update on Implications for Chronic Infections and Tumor Evasion. In *Cancer Immunology, Immunotherapy*; 2007; Vol. 56. https://doi.org/10.1007/s00262-006-0272-1.
(65) Schütz, F.; Stefanovic, S.; Mayer, L.; von Au, A.; Domschke, C.; Sohn, C. PD-1/PD-L1 Pathway in Breast Cancer. *Oncology Research and Treatment*. 2017. https://doi.org/10.1159/000464353.
(66) Wu, Q.; Jiang, L.; Li, S. cheng; He, Q. jun; Yang, B.; Cao, J. Small Molecule Inhibitors Targeting the PD-1/PD-L1 Signaling Pathway. *Acta Pharmacologica Sinica*. 2021. https://doi.org/10.1038/s41401-020-0366-x.
(67) Salmaninejad, A.; Valilou, S. F.; Shabgah, A. G.; Aslani, S.; Alimardani, M.; Pasdar, A.; Sahebkar, A. PD-1/PD-L1 Pathway: Basic Biology and Role in Cancer Immunotherapy. *Journal of Cellular Physiology*. 2019. https://doi.org/10.1002/jcp.28358.
(68) Xie, Z.; Gong, H.; Liu, M.; Zhu, H.; Sun, H. The Properties of Mesoporous Silica Nanoparticles Functionalized with Different PEG-Chain Length via the Disulfide Bond Linker and Drug Release in Glutathione Medium. *J Biomater Sci Polym Ed* **2016**, *27* (1), 55–68. https://doi.org/10.1080/09205063.2015.1107708.

(69) Wang, Y.; Han, N.; Zhao, Q.; Bai, L.; Li, J.; Jiang, T.; Wang, S. Redox-Responsive Mesoporous Silica as Carriers for Controlled Drug Delivery: A Comparative Study Based on Silica and PEG Gatekeepers. *European Journal of Pharmaceutical Sciences* **2015**, *72*, 12–20. https://doi.org/10.1016/j.ejps.2015.02.008.
(70) Rahikkala, A.; Pereira, S. A. P.; Figueiredo, P.; Passos, M. L. C.; Araújo, A. R. T. S.; Saraiva, M. L. M. F. S.; Santos, H. A. Mesoporous Silica Nanoparticles for Targeted and Stimuli-Responsive Delivery of Chemotherapeutics: A Review. *Advanced Biosystems*. 2018. https://doi.org/10.1002/adbi.201800020.
(71) Shi, L.; Zhang, J.; Zhao, M.; Tang, S.; Cheng, X.; Zhang, W.; Li, W.; Liu, X.; Peng, H.; Wang, Q. Effects of Polyethylene Glycol on the Surface of Nanoparticles for Targeted Drug Delivery. *Nanoscale*. 2021. https://doi.org/10.1039/d1nr02065j.
(72) Mitchell, M. J.; Billingsley, M. M.; Haley, R. M.; Wechsler, M. E.; Peppas, N. A.; Langer, R. Engineering Precision Nanoparticles for Drug Delivery. *Nature Reviews Drug Discovery*. 2021. https://doi.org/10.1038/s41573-020-0090-8.
(73) Begines, B.; Ortiz, T.; Pérez-Aranda, M.; Martínez, G.; Merinero, M.; Argüelles-Arias, F.; Alcudia, A. Polymeric Nanoparticles for Drug Delivery: Recent Developments and Future Prospects. *Nanomaterials*. 2020. https://doi.org/10.3390/nano10071403.
(74) Tramontano, C.; Miranda, B.; Chianese, G.; de Stefano, L.; Forestiere, C.; Pirozzi, M.; Rea, I. Design of Gelatin-capped Plasmonic-diatomite Nanoparticles with Enhanced Galunisertib Loading Capacity for Drug Delivery Applications. *Int J Mol Sci* **2021**, *22* (19). https://doi.org/10.3390/ijms221910755.
(75) Suk, J. S.; Xu, Q.; Kim, N.; Hanes, J.; Ensign, L. M. PEGylation as a Strategy for Improving Nanoparticle-Based Drug and Gene Delivery. *Advanced Drug Delivery Reviews*. Elsevier B.V. April 1, 2016, pp 28–51. https://doi.org/10.1016/j.addr.2015.09.012.
(76) Kunc, F.; Balhara, V.; Brinkmann, A.; Sun, Y.; Leek, D. M.; Johnston, L. J. Quantification and Stability Determination of Surface Amine Groups on Silica Nanoparticles Using Solution NMR. *Anal Chem* **2018**, *90* (22), 13322–13330. https://doi.org/10.1021/acs.analchem.8b02803.
(77) Oliviero, G.; Stornaiuolo, M.; D'Atri, V.; Nici, F.; Yousif, A. M.; D'Errico, S.; Piccialli, G.; Mayol, L.; Novellino, E.; Marinelli, L.; Grieco, P.; Carotenuto, A.; Noppen, S.; Liekens, S.; Balzarini, J.; Borbone, N. Screening Platform toward New Anti-HIV Aptamers Set on Molecular Docking and Fluorescence Quenching Techniques.

Anal Chem **2016**, *88* (4). https://doi.org/10.1021/acs.analchem.5b04268.
(78) Leijon, M.; Gräslund, A.; Nielsen, P. E.; Buchardt, O.; Kristensen, S. M.; Eriksson, M.; Nordén, B. Structural Characterization of PNA-DNA Duplexes by NMR. Evidence for DNA in a B-like Conformation. *Biochemistry* **1994**, *33* (33). https://doi.org/10.1021/bi00199a002.
(79) Roma-Rodrigues, C.; Mendes, R.; Baptista, P. v.; Fernandes, A. R. Targeting Tumor Microenvironment for Cancer Therapy. *International Journal of Molecular Sciences*. 2019. https://doi.org/10.3390/ijms20040840.
(80) de la Harpe, K. M.; Kondiah, P. P. D.; Choonara, Y. E.; Marimuthu, T.; du Toit, L. C.; Pillay, V. The Hemocompatibility of Nanoparticles: A Review of Cell-Nanoparticle Interactions and Hemostasis. *Cells*. NLM (Medline) October 7, 2019. https://doi.org/10.3390/cells8101209.
(81) Chakrabarty, G.; Naveenkumar, S. K.; Kumar, S.; Mugesh, G. Modulation of Redox Signaling and Thiol Homeostasis in Red Blood Cells by Peroxiredoxin Mimetics. *ACS Chem Biol* **2020**, *15* (10). https://doi.org/10.1021/acschembio.0c00309.
(82) Wiradharma, N.; Khan, M.; Yong, L. K.; Hauser, C. A. E.; Seow, S. V.; Zhang, S.; Yang, Y. Y. The Effect of Thiol Functional Group Incorporation into Cationic Helical Peptides on Antimicrobial Activities and Spectra. *Biomaterials* **2011**, *32* (34). https://doi.org/10.1016/j.biomaterials.2011.08.020.
(83) Fontana, F.; Ezazi, N. Z.; Tahir, N.; Santos, H. A. Cell–Nanoparticle Interactions: Toxicity and Safety Issues. In *Characterization of Pharmaceutical Nano and Microsystems*; 2021. https://doi.org/10.1002/9781119414018.ch6.
(84) Sabourian, P.; Yazdani, G.; Ashraf, S. S.; Frounchi, M.; Mashayekhan, S.; Kiani, S.; Kakkar, A. Effect of Physico-Chemical Properties of Nanoparticles on Their Intracellular Uptake. *International Journal of Molecular Sciences*. 2020. https://doi.org/10.3390/ijms21218019.
(85) Schiattarella, C.; Moretta, R.; Defforge, T.; Gautier, G.; della Ventura, B.; Terracciano, M.; Tortiglione, C.; Fardella, F.; Maddalena, P.; de Stefano, L.; Velotta, R.; Rea, I. Time-Gated Luminescence Imaging of Positively Charged Poly-l-Lysine-Coated Highly Microporous Silicon Nanoparticles in Living Hydra Polyp. *J Biophotonics* **2020**, *13* (12). https://doi.org/10.1002/jbio.202000272.
(86) Zhang, J.; Yamada, O.; Kida, S.; Murase, S.; Hattori, T.; Oshima, Y.; Kikuchi, H. Downregulation of PD-L1 via Amide Analogues of

Brefelamide: Alternatives to Antibody-based Cancer Immunotherapy. *Exp Ther Med* **2020**. https://doi.org/10.3892/etm.2020.8553.

(87) Yamaguchi, I.; Nakajima, K.; Shono, K.; Mizobuchi, Y.; Fujihara, T.; Shikata, E.; Yamaguchi, T.; Kitazato, K.; Sampetrean, O.; Saya, H.; Takagi, Y. Downregulation of PD-L1 via FKBP5 by Celecoxib Augments Antitumor Effects of PD-1 Blockade in a Malignant Glioma Model. *Neurooncol Adv* **2020**, *2* (1). https://doi.org/10.1093/noajnl/vdz058.

(88) Nimmagadda, S. Quantifying Pd-L1 Expression to Monitor Immune Checkpoint Therapy: Opportunities and Challenges. *Cancers*. MDPI AG November 1, 2020, pp 1–26. https://doi.org/10.3390/cancers12113173.

(89) Yuan, Y.; Adam, A.; Zhao, C.; Chen, H. Recent Advancements in the Mechanisms Underlying Resistance to Pd-1/Pd-L1 Blockade Immunotherapy. *Cancers*. 2021. https://doi.org/10.3390/cancers13040663.

(90) Ju, X.; Zhang, H.; Zhou, Z.; Wang, Q. Regulation of PD-L1 Expression in Cancer and Clinical Implications in Immunotherapy. *Am J Cancer Res* **2020**, *10* (1).

(91) Ghosh, C.; Luong, G.; Sun, Y. A Snapshot of the PD-1/PD-L1 Pathway. *J Cancer* **2021**, *12* (9). https://doi.org/10.7150/JCA.57334.

(92) Crisci, T.; Falanga, A. P.; Casalino, M.; Borbone, N.; Terracciano, M.; Chianese, G.; Gioffrè, M.; D'errico, S.; Marzano, M.; Rea, I.; de Stefano, L.; Oliviero, G. Bioconjugation of a Pna Probe to Zinc Oxide Nanowires for Label-Free Sensing. *Nanomaterials* **2021**, *11* (2). https://doi.org/10.3390/nano11020523.

(93) Hamanishi, J.; Mandai, M.; Matsumura, N.; Abiko, K.; Baba, T.; Konishi, I. PD-1/PD-L1 Blockade in Cancer Treatment: Perspectives and Issues. *International Journal of Clinical Oncology*. Springer Tokyo June 1, 2016, pp 462–473. https://doi.org/10.1007/s10147-016-0959-z.

(94) Mellman, I.; Coukos, G.; Dranoff, G. Cancer Immunotherapy Comes of Age. *Nature*. Nature Publishing Group December 22, 2011, pp 480–489. https://doi.org/10.1038/nature10673.

(95) Jácome, A. A.; Ana, ; Castro, C. G.; João, ; Vasconcelos, P. S.; Maria, ; Silva, H. C. R.; Marco, ; Lessa, A. O.; Moraes, E. D.; Andrade, A. C.; Lima, F. M. T.; Farias, P. F.; Gil, R. A.; Prolla, G.; Garicochea, B. Efficacy and Safety Associated With Immune Checkpoint Inhibitors in Unresectable Hepatocellular Carcinoma A Meta-Analysis + Supplemental Content Downloaded From:

Https://Jamanetwork.Com/ by a Universita Degli Studi Di Napoli Federico II User on 07/14/2022. *JAMA Netw Open* **2021**, *4* (12), 2136128. https://doi.org/10.1001/jamanetworkopen.2021.36128.
(96) Putnam, D. A. *Antisense Strategies and Therapeutic Applications*.
(97) Nagel, K. M.; Pharm, B. S.; Holstad, S. G.; Isenberg, K. E. *Oligonucleotide Pharmacotherapy: An Antigene Strategy*. https://doi.org/10.1002/j.1875-9114.1993.tb02723.x.
(98) Jain, M. L.; Bruice, P. Y.; Szabó, I. E.; Bruice, T. C. Incorporation of Positively Charged Linkages into DNA and RNA Backbones: A Novel Strategy for Antigene and Antisense Agents. *Chemical Reviews*. March 14, 2012, pp 1284–1309. https://doi.org/10.1021/cr1004265.
(99) Nielsen, P. E.; Egholm, M. *An Introduction to Peptide Nucleic Acid*; 1999.
(100) Montazersaheb, S.; Avci, Ç. B.; Bagca, B. G.; Ay, N. P. O.; Tarhriz, V.; Nielsen, P. E.; Charoudeh, H. N.; Hejazi, M. S. Targeting TdT Gene Expression in Molt-4 Cells by PNA-Octaarginine Conjugates. *Int J Biol Macromol* **2020**, *164*, 4583–4590. https://doi.org/10.1016/j.ijbiomac.2020.09.081.
(101) Hamashita, Y.; Shibata, T.; Takeuchi, A.; Okuno, T.; Kise, N.; Sakurai, T. Inchworm-Type PNA-PEG Conjugate Regulates Gene Expression Based on Single Nucleotide Recognition. *Int J Biol Macromol* **2021**, *181*, 471–477. https://doi.org/10.1016/j.ijbiomac.2021.03.140.
(102) Das, A.; Pradhan, B. Evolution of Peptide Nucleic Acid with Modifications of Its Backbone and Application in Biotechnology. *Chemical Biology and Drug Design*. Blackwell Publishing Ltd April 1, 2021, pp 865–892. https://doi.org/10.1111/cbdd.13815.
(103) Comegna, M.; Conte, G.; Falanga, A. P.; Marzano, M.; Cernera, G.; di Lullo, A. M.; Amato, F.; Borbone, N.; D'Errico, S.; Ungaro, F.; d'Angelo, I.; Oliviero, G.; Castaldo, G. Assisting PNA Transport through Cystic Fibrosis Human Airway Epithelia with Biodegradable Hybrid Lipid-Polymer Nanoparticles. *Sci Rep* **2021**, *11* (1). https://doi.org/10.1038/s41598-021-85549-z.
(104) Falanga, A. P.; Cerullo, V.; Marzano, M.; Feola, S.; Oliviero, G.; Piccialli, G.; Borbone, N. Peptide Nucleic Acid-Functionalized Adenoviral Vectors Targeting G-Quadruplexes in the P1 Promoter of Bcl-2 Proto-Oncogene: A New Tool for Gene Modulation in Anticancer Therapy. *Bioconjug Chem* **2019**, *30* (3), 572–582. https://doi.org/10.1021/acs.bioconjchem.8b00674.

(105) Saarbach, J.; Sabale, P. M.; Winssinger, N. Peptide Nucleic Acid (PNA) and Its Applications in Chemical Biology, Diagnostics, and Therapeutics. *Current Opinion in Chemical Biology*. Elsevier Ltd October 1, 2019, pp 112–124. https://doi.org/10.1016/j.cbpa.2019.06.006.
(106) Cesaro, E.; Falanga, A. P.; Catapano, R.; Greco, F.; Romano, S.; Borbone, N.; Pastore, A.; Marzano, M.; Chiurazzi, F.; D'errico, S.; Piccialli, G.; Olivieroid, G.; Costanzo, P.; Grossoid, M. Exploring a Peptide Nucleic Acid-Based Antisense Approach for CD5 Targeting in Chronic Lymphocytic Leukemia. **2022**. https://doi.org/10.1371/journal.pone.0266090.
(107) Chan, J. H.; Lim, S.; Fred Wong, W. *ANTISENSE OLIGONUCLEOTIDES: FROM DESIGN TO THERAPEUTIC APPLICATION*; 2006; Vol. 33.
(108) Croyle, M. A.; Le, H. T.; Linse, K. D.; Cerullo, V.; Toietta, G.; Beaudet, A.; Pastore, L. PEGylated Helper-Dependent Adenoviral Vectors: Highly Efficient Vectors with an Enhanced Safety Profile. **2005**. https://doi.org/10.1038/sj.gt.3302441.
(109) Seregin, S. S.; Amalfitano, A. Improving Adenovirus Based Gene Transfer: Strategies to Accomplish Immune Evasion. *Viruses* **2010**, *2*, 2013–2036. https://doi.org/10.3390/v2092013.
(110) Liu, Q.; Muruve, D. A. Molecular Basis of the Inflammatory Response to Adenovirus Vectors. https://doi.org/10.1038/sj.gt.3302036.
(111) Wonganan, P.; Croyle, M. A. PEGylated Adenoviruses: From Mice to Monkeys. *Viruses* **2010**, *2*, 468–502. https://doi.org/10.3390/v2020468.
(112) Wonganan, P.; Clemens, C. C.; Brasky, K.; Pastore, L.; Croyle, M. A. Species Differences in the Pharmacology and Toxicology of PEGylated Helper-Dependent Adenovirus. https://doi.org/10.1021/mp100216h.
(113) Kreppel, F.; Kochanek, S. Modification of Adenovirus Gene Transfer Vectors with Synthetic Polymers: A Scientific Review and Technical Guide. *Molecular Therapy*. Nature Publishing Group 2008, pp 16–29. https://doi.org/10.1038/sj.mt.6300321.
(114) Capasso, C.; Hirvinen, M.; Garofalo, M.; Romaniuk, D.; Kuryk, L.; Sarvela, T.; Vitale, A.; Antopolsky, M.; Magarkar, A.; Viitala, T.; Suutari, T.; Bunker, A.; Yliperttula, M.; Urtti, A.; Cerullo, V. Oncolytic Adenoviruses Coated with MHC-I Tumor Epitopes Increase the Antitumor Immunity and Efficacy against Melanoma.

Oncoimmunology **2016**, *5* (4). https://doi.org/10.1080/2162402X.2015.1105429.
(115) Wang, T.; Wang, L.; Li, X.; Hu, X.; Han, Y.; Luo, Y.; Wang, Z.; Li, Q.; Aldalbahi, A.; Wang, L.; Song, S.; Fan, C.; Zhao, Y.; Wang, M.; Chen, N. Size-Dependent Regulation of Intracellular Trafficking of Polystyrene Nanoparticle-Based Drug-Delivery Systems. *ACS Appl Mater Interfaces* **2017**, *9* (22), 18619–18625. https://doi.org/10.1021/acsami.7b05383.
(116) Qu, Q. X.; Xie, F.; Huang, Q.; Zhang, X. G. Membranous and Cytoplasmic Expression of PD-L1 in Ovarian Cancer Cells. *Cellular Physiology and Biochemistry* **2018**, *43* (5), 1893–1906. https://doi.org/10.1159/000484109.
(117) Kirn, D. *Replication-Selective Oncolytic Adenoviruses: Virotherapy Aimed at Genetic Targets in Cancer*; 2000; Vol. 19.
(118) Chu, R. L.; Post, D. E.; Khuri, F. R.; van Meir, E. G. *Use of Replicating Oncolytic Adenoviruses in Combination Therapy for Cancer*.

CHAPTER 3 DNA AND RNA SECONDARY STRUCTURES: FROM THE BIOLOGY TO THE MATERIAL SCIENCE APPLICATION

3.1 DNA secondary structure: G-quadruplex and C-quadruplex structures

Since in the 1950s, Watson and Crick demonstrated the B-double helix conformation of DNA in a physiological environment, a deep interest in DNA morphology has been stressed in the scientific community. Several secondary structures[1] of oligonucleotides were identified fig. 28:
Z and A double helix conformations, hairpin structures, four-way junctions, triplex and quadruplex structures.
It has been proved that the non-canonical structures of DNA represent a way for these molecules to communicate and regulate some physiological processes in the cell environment[2]. The most representative secondary structures are the Quadruplexes: Guanine (G) and Cytosine (C). A prerequisite of sequence leads to their conformation: G-rich and C-rich oligonucleotides (ODN) are requested, respectively. A deep study on G-quadruplex complexes already exists due to their revealed ability to interfere in different biological systems, for example, control of tumoral cell expression centromeres formation and as transcriptional regulators[3-5]. Moreover, they are typically involved in the selection process of aptamers.

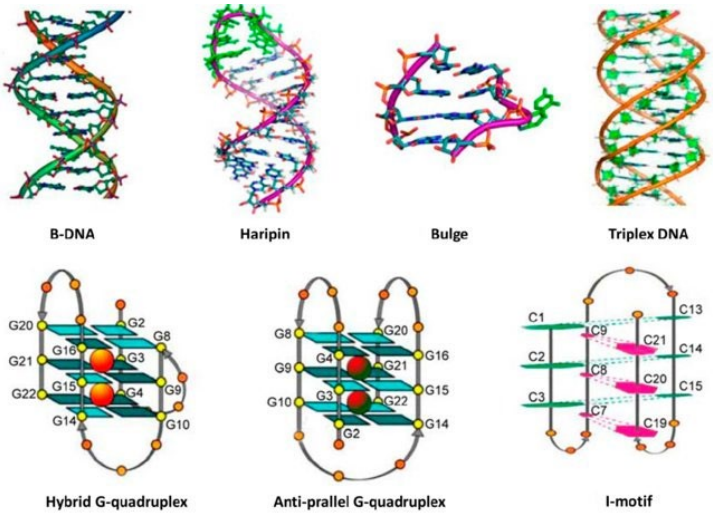

Figure 28 DNA conformations

Zhang, S.; Ding, Y.; Wei, H. Ruthenium Polypyridine Complexes Combined with Oligonucleotides for Bioanalysis: A Review. Molecules 2014, 19, 11933-11987.

The most representative secondary structure of DNA in vivo is G-quadruplexes[6-7]. The G-quadruplex formation depends on oligonucleotide base composition. Four guanine residues, termed G-tetrad, can organize in a planar arrangement through eight Hoogsteen bonds. G-tetrads interact with each other via π-π stacking, allowing the G-quadruplex complex and a metallic ion (K+> Ca2+> Na+>Mg2+> Li+ and K+>Rb+> Cs+) to fit in a pair of G-quartet to coordinate Guanine residue repulsions[8].

G-quadruplex structures can be divided into unimolecular structures and bi/tetra-molecular folding. The diverse conformations also converge in different strand orientations, parallel G4s have the same strand orientation within the system, and antiparallel G4s have alternating strand orientations[9]. When the strands that compose the structures contain C-A-T nucleotides interposed into the Guanine series, they can be part of the conformation but outstanding the secondary structure, forming loops.

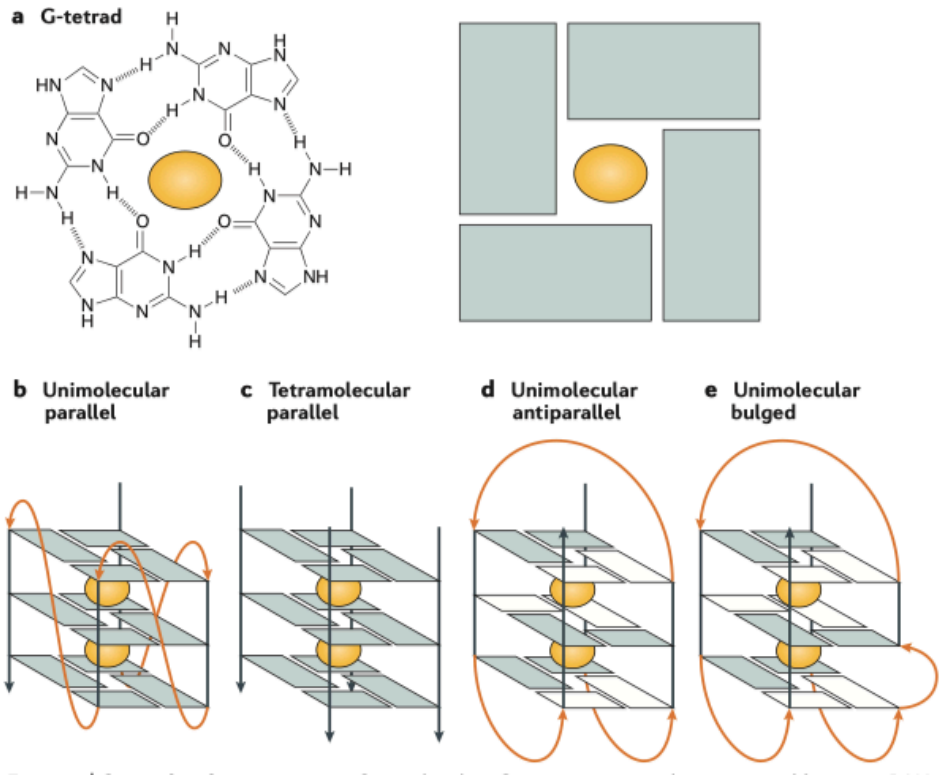

Figure 29 G-quadruplexes polymorphisms

In silico studies using simple algorithms indicates that over 300,000 sequence region in the human genome potentially conforms to G4 secondary structures[13].
Many G4 intragenomic sequences were identified and localized due to the application of specific antibodies based on the employment of the Chip-seq technique.
Therapeutic opportunities related to G4 presence in the genome can depend on several circumstances in which G4s are involved:

1. DNA G quadruplexes can initiate DNA damage and genomic instability (G4s), either by their stabilization with small molecules or by the impairment of helicases that resolve G quadruplexes.
2. G4 ligands, in combination with other therapies in the oncotherapy can stabilize the conformation and prevent the mRNA synthesis of an oncogenic protein.

3. The G4 interaction with drugs or ligands can promote the Double-strand breaks causing DNA damage and inducing activation of DNA repair.

Apart from in vivo representation of DNA secondary structures, they are also often involved in the aptamers selection.

The recognition of several protein systems and the biological effects produced are related to the G-quadruplex ductile and stable conformation, easy to combine with proteins or enzymes. The TBA sequence d(G2T2G2TGTG2T2G2)[10] is the most known aptamer G4 based. It can bind the fibrinogen binding site of thrombin, causing the cleavage of the fibrinogen and inhibiting the formation of fibrin clots in the blood. The binding of TBA to α-thrombin prevents the pathological process of thrombosis. Recent studies on TBA aptamers suggest that they can be used in biosensing, with a nanomolar affinity to thrombin.

Biosensors based on biological probes such as protein, DNA, RNA, antibody are known to be extremely sensitive. ODNs probes are used to diagnose genetic diseases, microorganisms' presence, viruses, and the presence of infectious agents in various environmental matrices. Conformed DNA strands, especially G-quadruplex conformed species, are used for this aim[7].

Furthermore, because Guanine is complementary to Cytosine, in the presence of G-rich sequences, there are also C-rich filaments that are equally able to form quadruplexes (C-quadruplex)[11], more commonly known as I-motif conformations,fig.30. However, having C-rich sequences is not the only request to get I motif structures: an acid environment for Cytosine bases protonation is necessary. The protonation of Cytosines permits the formation of parallel duplexes through three hydrogen bonds between each pair of Cytosine residues. Then a duplex can interact with another one forming a Quadruplex complex that assumes an antiparallel trend[12]. The hemi-protonated C:C+ base pairs are the critical interactions for i-motif stability. The three hydrogen bonds of the C:C+ base-pair confer higher stability. Computer calculations indicate that the base-pairing energy (BPE) for the C:C+ base pair is 169.7 kJ/mol, higher than BPEs of canonical Watson-Crick G·C (96.6 kJ/mol) and neutral C·C (68.0 kJ/mol)[17].

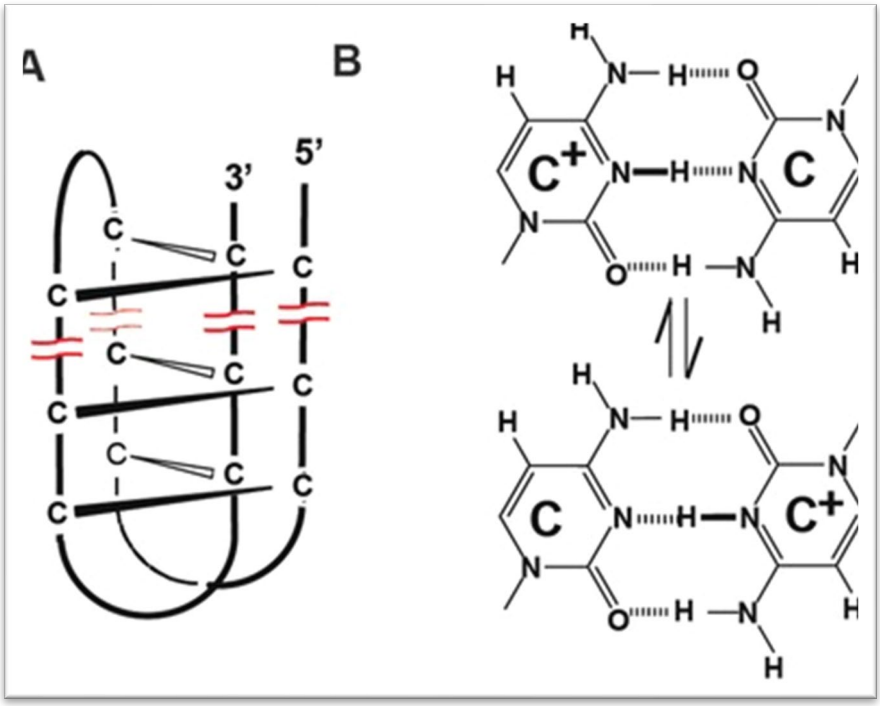

Figure 30 Chemical analysis of I motif conformation Nautiyal S, Rai V, Bhat S, Kumar R, Rather M M, Sankar M (2020) i-Motif DNA: Significance and future prospective. Explor Anim Med Res 10(1): 18-23.

Since their formation requires the hemi-protonation of cytosines, most i-Motif structures are stable only at pH values near the pKa of cytosine N3 (pKa ≈4.8, in water); however recent studies demonstrated that a few examples of i-motif structures had been observed at neutral or nearly neutral pH (6-7).
Lately, C-quadruplexes have been deeply investigated. It has been hypothesized and seen their biological application is linked to gene regulation and expression, fig.31. It was reported that C-rich DNAs are bound by proteins, such as the poly-C-binding proteins (PCBP), and, interestingly, when structured in i-motif, they can bind proteins belonging to the heterogeneous nuclear ribonucleoprotein (hnRNP) family. Besides, these structures can also be recognized by proteins responsible for gene regulation[13]. i-Motif-containing aptamers have been used to specifically bind cells by exploiting the peculiarities of cellular pHs. Furthermore, ultra-pH-responsive i-motif aptamers were employed in sensing technologies to specifically achieve

imaging of different cancer types *in vitro* and *in vivo* by exploiting the slight differences in extracellular pH values of different cancers.

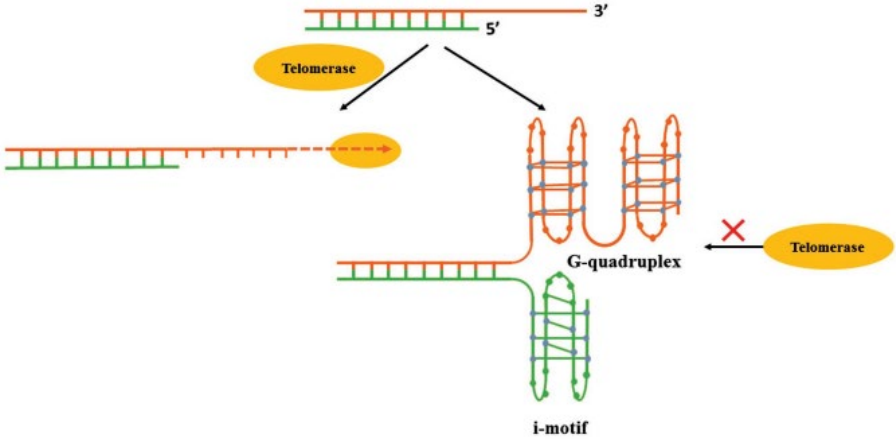

Figure 31 Biological importance of DNA quadruplexes.

Tetramolecular, bimolecular, and monomolecular i-motif complexes have been reported in the literature (C–F, Fig. 32).

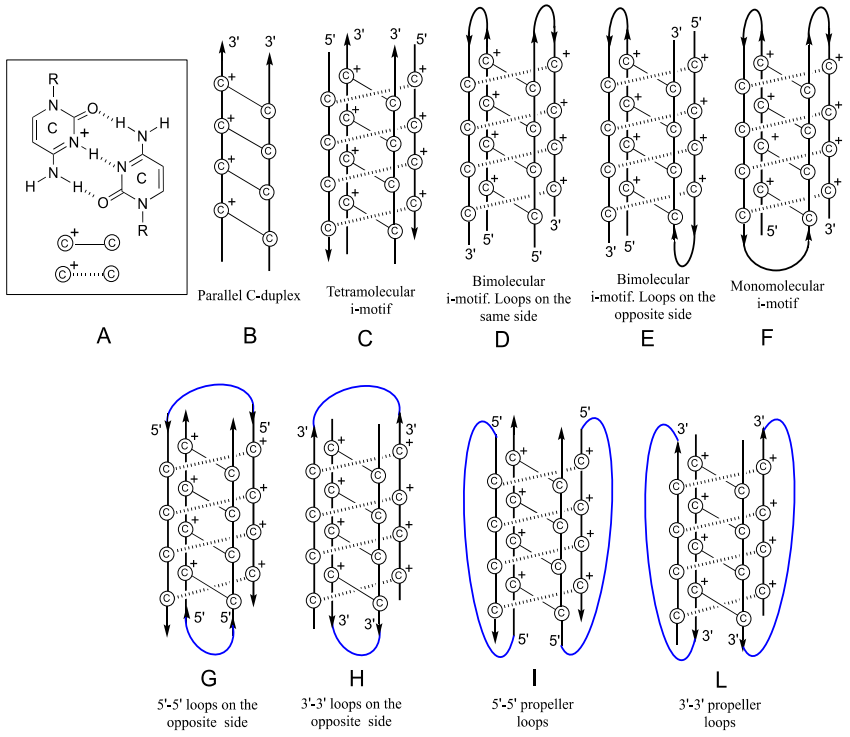

*Figure 32 Structures and topologies of i-motifs: **A**: C-C$^+$ base pair; **B**: parallel C-duplex; **C**: tetramolecular i-motif; **D**,**E**: bimolecular i-motifs; **F**: monomolecular i-motif; **G**,**H**: bimolecular i-motifs containing 5'-5' or 3'-3' diagonal loops (blue), respectively; **I**,**L**: bimolecular i-motifs containing 5'-5' or 3'-3' propeller loops, respectively.*

i-Motif stability can depend on several factors. The non-cytosine nucleotides flanking the poly-C strands play an essential role in i-motif stabilization, especially for tetramolecular complexes. Also, the stability of bimolecular or unimolecular i-motif complexes strictly depends on the length and base composition of the loop[14-17]. Chemical modifications of CROs and the crowding effect aimed to stabilize and enlarge the structural variety of the i-motif DNA have also been investigated.

In 1963, i-Motif structures were discovered and attracted considerable interest because of their possible implication for biological processes.

Over time, the potentiality of i-Motifs has been considered their building blocks attitude for constructing supramolecular assemblies in DNA nanotechnology. Furthermore, based on i-motif structures, pH-responsive DNA nanomachines, hydrogels, pH-stimulated drug-releasing carriers, and controlled nano-gold assemblies have been

reported. In the last studies, it was put forward for consideration the application of i-motif formation not just in biological patterns but also for the synthesis of a new class of polymer DNA based, which could find application in nanotechnologies such as for the development of nanodevices, assemblies of nanoparticles and creation of sensible pH sensors. In the last years, the ability of DNA strands to assume many different secondary structures in vivo increased the interest in studying how to stabilize them in biological relevant sequences and oncogenic regions to widen the current antitumoral approaches.

3.2 Aim of the worl

DNA secondary structures are typically present in regulatory regions of the genome, exploiting a crucial biological role by altering DNA replication, transcription, and translation.
Oncogenes are genomic DNA tracts coding for proteins and enzymes with decisive participation in cancer sustainment. This class of genes, such as c-MYC, VEGF, KRAS, c-kit, PDGF-A, and c-Myb, is abundant in secondary structures.
The first G-quadruplex conformation was identified in the telomers. As a regulatory part of the genome, they were demonstrated to rearrange in G-quadruplex structures to arrest and control cell senescence. In this context, studies based on the stabilization attempts of these regulatory sequences were carried out to increase their thermal and enzymatic resistance. In therapy, the possibility of freezing the secondary DNA conformations to regulate the gene expression finds application in oncology, for example. Conversely, the use of G-quadruplex or C-quadruplex ODN represents a valid alternative for designing new biosensors for diagnostics purposes, too. Lately, the DNA scaffold is emerging as a promising tool for obtaining stable self-assembled and supramolecular structures opening the way to further DNA applications such as in nanotechnology and bioelectronics. It is noteworthy that experimental findings indicate that DNA G4s are a great conductor of electricity, even more than the DNA duplex.
Supporting the aforementioned themes, my research activity has been focused on:

- Objective 1: Synthesis and characterization of i-motif structures, exploiting the influence of a non-nucleotide chemical linker in the final assemblies.
- Objective 2: Spectroscopic and computational investigation on the binding of the c-myc oncogene NHE III1 region through the phytochemical polydatin ligand.

Objective 1 Cytosine-rich oligonucleotides incorporating a non-nucleotide loop: A further step towards the obtainment of physiologically stable i-motif DNA (Publication n°1)

This study reports the design of new structurally modified Double-Ended-Linker-CROs (DEL-CROs), capable of forming stable i-motif structures. Here, two C-rich strands having sequences d(AC4A) and d(C6) have been attached, in a parallel fashion, to the two linker's edges by their 3' or 5' ends.
DEL-CROs 3–6 were synthesized through a solid-phase automated DNA synthesizer, using the commercially available controlled pore glass (CPG)-sulphone-resin 1 (Scheme 2) and the phosphoramidite linker 9 to obtain the support 2. On support 2, the CRO syntheses were performed using 3' or 5' phosphoramidite building blocks to obtain the DEL-CROs 4 and 6, and 3 and 5, respectively [40]. The natural d(AC4A) (7) and d(C6) (8) were synthesized by standard phosphoramidite protocols. After their synthesis, 3–8 were purified as described elsewhere [40], and their chemical identity was confirmed by ESI-MS data. All compounds were analyzed at least 24 h after the annealing procedure.

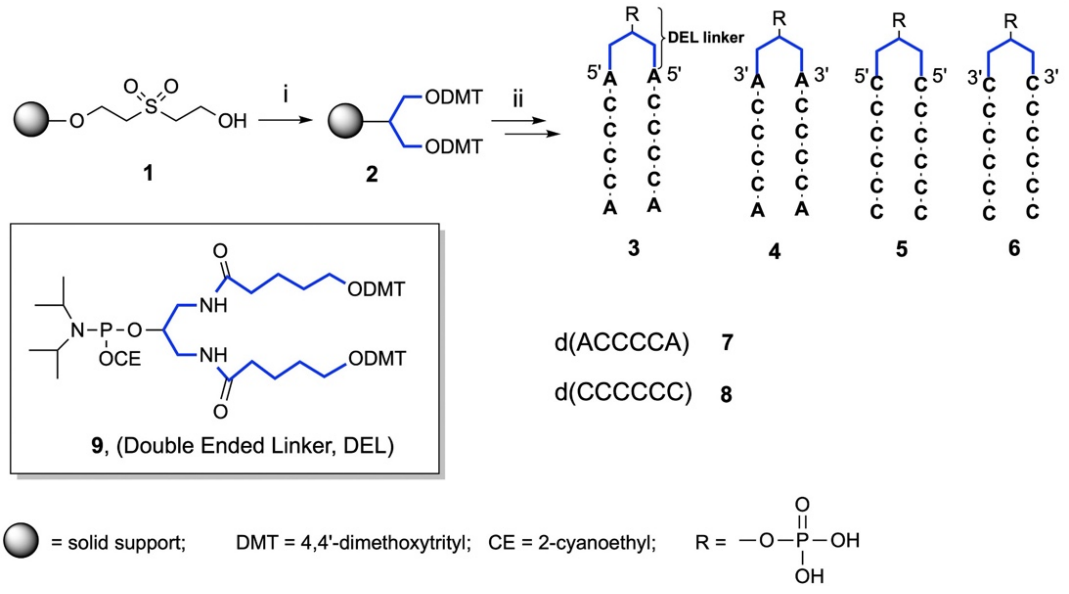

Scheme 2. General synthetic route for the preparation of DEL-CROs 3–6: (i) couplings with the phosphoramidite linker 9; (ii) automated solid-phase DNA synthesis by 5 '-phosphoramidite nucleosides (for 3 and 5) and 3 ' -phosphoramidite nucleosides (for 4 and 6).

Circular Dichroism Studies

CD spectroscopy provides essential information about the conformational properties of DNA secondary structures, including the B, A, and Z-forms of duplexes, triplexes, G-quadruplexes, i-motifs, and other less characterized DNA structures. We investigated the formation of the i-motif structures for DEL-CROs 3–6 in comparison with the natural d(AC$_4$A) (7) and d(C$_6$) (8) counterparts at pH 4.5 and 7.0. To exclude the effect of the CRO concentration on the formation of i-motif species, we annealed 7 and 8 at 1.0 mM concentration while DEL-CROs 3–6 were at 0.5 mM concentration. It is well reported that the typical CD spectrum of an i-motif structure shows an intense positive band centered around 288 nm, a less intense negative band around 260 nm, and a positive band around 220 nm [41–43]. We recorded the CD spectra in the range 5–90 °C. The CD profiles recorded at 5 and 25 °C are reported in Fig. 33.

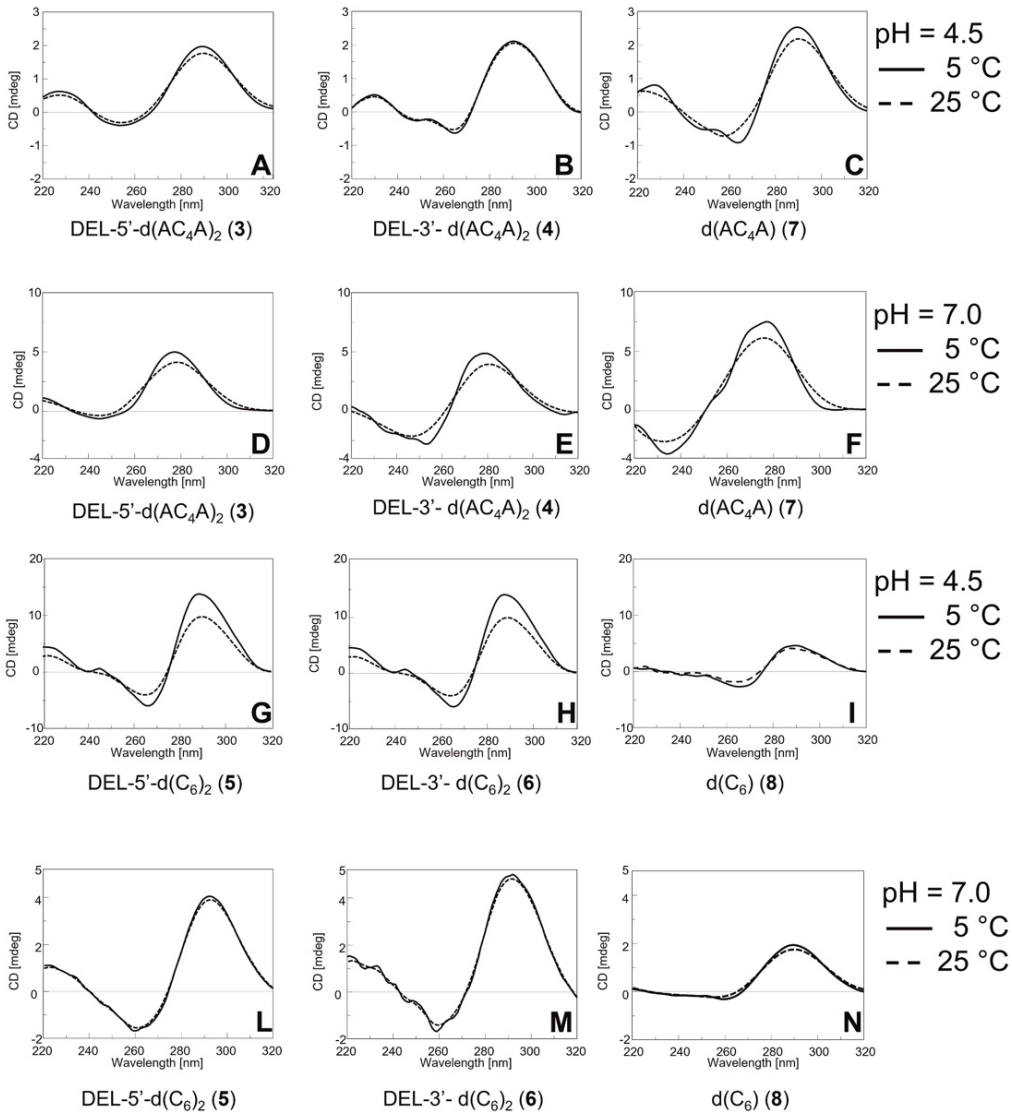

Figure 33. CD profiles of 3–8 annealed in 100 mM K + phosphate buffer at pH 4.5 and 7.0.

The CD spectra of DEL-5'-d(AC_4A)$_2$ (3) at pH 4.5 (Fig. 33a) exhibited the typical CD profile of an i-motif, with a well-defined large positive band at 290 nm, a negative band at 255 nm, and a less intense positive band at 228 nm. DEL-3'-d(AC_4A)$_2$ (4) under the same conditions gave similar CD profiles with two positive bands at 228 and 290 nm and a negative band at 265 nm (Fig. 33b). These data suggested that 3 and 4, independently of the orientation of ODN strands on the DEL linker, could form i-motif structures 24 h after the

annealing at pH 4.5, likely corresponding to the bimolecular arrangements. In the same conditions, the natural d(AC_4A) (7) showed CD profiles which resulted almost superimposable with those of DEL-3'-d($AC_4A)_2$ (4) (positive bands at 228 and 289 nm and a negative band at 264 nm) (Fig. 33c), thus revealing that also 7 could form a detectable amount of an i-motif structure, likely corresponding to the tetramolecular species. The formation of the i-motif structure for 3, 4, and 7 was confirmed by ^{1}H-NMR evidence.
To get insight into the thermal stability of the i-motif arrangements, we estimated their melting temperature by monitoring the intensity of the CD signal at the λ_{max} of the most intense positive band. The T_m value of 52 °C for DEL-5'-d($AC_4A)_2$ (3) suggested that this product formed a more stable i-motif than DEL-3'-d($AC_4A)_2$ (4) (T_m = 44 °C) and d(AC_4A) (7) (T_m = 39 °C). The ensemble of CD data indicated that the coupling of 7 to the two arms of the DEL linker 2 by their 5' or 3' ends, to obtain 3 and 4, respectively, did not hamper the formation of the corresponding bimolecular C-quadruplex, which indeed resulted more stable than the corresponding tetramolecular counterpart.
The CD spectra of 3, 4, and 7 annealed at pH 7.0 were all characterized by a ~10 nm blue shift of the most intense CD band, which moved from ~290 to ~280 nm (Fig. 33 d–f). Although the resulting CD profiles did not confirm the formation of the i-motif structure at pH 7.0, the CD_{280} melting profiles indicated the possible presence in solution of different not defined complexes having melting temperature of about 32 °C. The formation of i-motif complexes starting from CROs containing a run of four cytosines was previously investigated. It was reported that the single-stranded d(C_4) sequence did not form a stable i-motif tetraplex even at acidic pH . Instead, stable i-motif structures could be obtained by hanging one or more non-C bases at 5' and/or 3'-ends, as for d(TC_4T) , d($T_2C_4T_2$) , and d($AC_4A_2C_4$) .
Then, we performed the CD analyses of DEL-d($C_6)_2$ 5 and 6 compared to the natural counterpart d(C_6) (8). For these compounds, it could be expected that the increased number of cytosines could generate more stable i-motif complexes.
The CD spectrum of DEL-5'-d($C_6)_2$ (5) at pH 4.5 showed the characteristic profile of an i-motif structure (Fig. 33 g) with a positive band at 292 nm and a negative band at 260 nm. This finding, together with a higher CD_{292} melting temperature (73 °C), indicated the capability of 5 to fold in a very stable i-motif complex.

The CD of DEL-3'-d$(C_6)_2$ (6) at pH 4.5 showed a profile with an intense positive band at 290 nm and a weaker negative band at 265 nm (Fig. 30h), which accounted for the presence in the solution of an i-motif structure. The related CD_{290} melting analysis indicated for 6 a T_m of 60 °C (Table 7).

ODN	CD λ_{max} (nm) pH 4.5	T_m (°C) pH 4.5	CD λ_{max} (nm) pH 7.0	T_m (°C) pH 7.0
d(AC_4A) (**7**)	289	39	276	32
DEL-5′-d (AC_4A)$_2$ (**3**)	289	52	280	n.d.[a]
DEL-3′-d (AC_4A)$_2$ (**4**)	290	44	279	32
d(C_6) (**8**)	290	50	275	32
DEL-5′-d(C_6)$_2$ (**5**)	290	73	290	36
DEL-3′-d(C_6)$_2$ (**6**)	290	60	290	37

Table 7 Melting temperatures of the i-motifs scaffolds measured by CD (λmax) intensity variation at increasing temperatures at pH 4.5 and 7.0.

The CD analysis of the natural d(C_6) (8) at pH 4.5 showed a similar CD profile, accounting for the formation of a tetramolecular i-motif. The lower CD_{290} melting temperature of 8 (50 °C) compared to that of 5 (73 °C) and 6 (60 °C) confirmed the stabilizing effect of the DEL linker in the formation of i-motif complexes.
The CD spectra of DEL-5'-d$(C_6)_2$ (5), DEL-3'-d$(C_6)_2$ (6), and d(C_6) 8 at pH 7.0 are reported in Fig. 2l–n. 5 and 6 showed the typical CD profile of an i-motif structure, with two positive bands at 290 nm (major) and 225 nm (minor), and a negative band at 265 nm (Fig. 33l and 33m, respectively). Both compounds showed well-defined CD_{290} melting curves with T_m of 36 and 39 °C, respectively. Differently from what was observed at pH 4.5, the CD profile of d(C_6) (8) recorded at pH 7.0 was almost superimposable with that of d(AC_4A) (7), not supporting the presence in the solution of an i-motif secondary structure (Fig. 33n). Finally, the CD_{290} melting analysis of 8 at pH 7.0 (T_m = 32 °C) indicated that likewise 3, 4, and 7 also 8 folds into not defined secondary structures which melt at around 32 °C. C-rich ODN sequences containing six consecutive cytosines

were already studied in the i-motif formation by CD spectroscopy. In these cases, the reports indicated that the introduction of one or more non-C nucleotides at the 5' and 3' ends resulted in the stabilization of the resulting i-motif structures [44]. Our CD data suggested that when the DEL-linker is attached to two 5'-ODN ends (as in 3 and 5), it produces at pH 4.5 i-motifs having higher stability than the corresponding DEL-3'-ODN_2 (4 and 6) and tetramolecular counterparts. At pH 7.0, CD analyses suggested that only the DEL-$d(C_6)_2$ 5 and 6 produced detectable amounts of i-motif structures having, as expected, lower stability than the same complexes obtained at pH 4.5.

Non-Denaturing Polyacrilammide Gel Electrophoresis

To get additional information on the molecularity of the complexes formed by the studied CROs when annealed in 100 mM K^+ buffer at pH 4.5, we performed PAGE investigation in a Tris-Acetate-EDTA buffer (TAE) using UV irradiation at 254 nm (Fig. 34). The tetramolecular G-quadruplex formed by $d(TG_4T)$ was used as the size marker. DEL-3'-$d(C_6)_2$ (6) (lane 1) migrated as a single band, slightly faster than that of the ~24 nt G-quadruplex size marker (lane 8). DEL-5'-$d(C_6)_2$ (5) (lane 2), differing from 6 only for the orientation of the two CRO strands on the DEL, migrated as a smeared band which resulted even faster than the band obtained from 6. Surprisingly, the PAGE mobility of $d(C_6)$ (8) (lane 3) appeared similar to that of the running marker (lane 4). The velocity of the former, attributable to the single-stranded $d(C_6)$ species, was not in agreement with what was expected based on CD and CD melting experiments, which were indicative of the presence in the solution of structured secondary structures. This contradictory result can be attributed to the formation of an insoluble pellet made of $d(C_6)_n$ i-motif aggregates, whose formation is favored at the high sample concentration required by the PAGE experimental setting.
DEL-3'-$d(AC_4A)_2$ and DEL-5'-$d(AC_4A)_2$ products (lanes 5 and 6) migrated both as a pair of bands. The most intense and faster band had a mobility rate very close to that of the 24-nt G-quadruplex marker, whereas the slower band was indicative of the presence in the solution of supramolecular structures. Finally, $d(AC_4A)$ (lane 7) ran as a single band whose migration rate was higher than those of the fastest band observed for 5 and 6. Taken together, the results from the PAGE analysis performed at pH 4.5 confirmed the

formation of ordered secondary structures for all the studied CROs, which, based on the mobility rate and its comparison with the 24-nt G-quadruplex size marker, can be confidently attributed to the bimolecular i-motif arrangements. Moreover, the observation of a less intense and more retained band in lanes 5 and 6 revealed that higher molecular weight supramolecular assemblies could be obtained starting from DEL-3'd(AC_4A)$_2$ and DEL-5'd(AC_4A)$_2$.

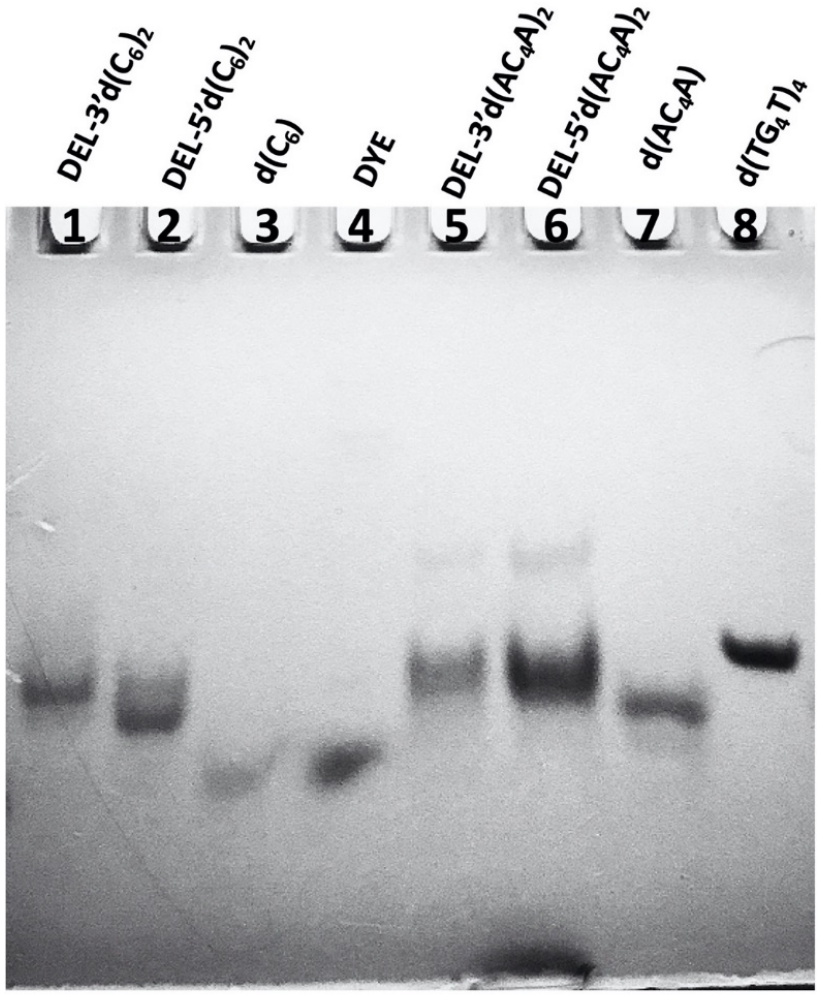

Figure 34. PAGE analysis of d(C 6) and d(AC 4 A) CROs and corresponding DEL-CROs at pH 4.5. The PAGE was exposed to the UV light (λ = 254 nm) after being placed on a PLC silica gel 60 F 254, 1.0 mm thickness, 20 cm × 20 cm glass plate.

SEC HPLC Analysis

In the last years, HPLC Size Exclusion Chromatography (SEC) has been largely utilized to evaluate the molecular weight (MW) of secondary structures of DNA, like G-quadruplexes and related supramolecular assemblies. Here, we analyzed by HPLC-SEC the DEL-CROs 3–6 and their natural counterparts (7, 8) after annealing in 100 mM K^+-containing phosphate buffer at pH 4.5 (Fig. 35). All samples were eluted with 100 mM K^+ phosphate buffer at pH 4.5. As the size markers, we used the unfolded d(T_6) and d(C_6) ODNs (6 nt), and the monomeric (24-nt) and dimeric (48-nt) tetramolecular G-quadruplexes formed respectively by the d(TG_4T) and d(CG_2AG_2T) G-rich sequences. For the d(C_6) size marker, to avoid the formation of the i-motif structure, we raised the pH of the HPLC-SEC elution buffer to 7.0. The HPLC-SEC analyses of d(AC_4A) (7) annealed at pH 4.5 (Fig. 35) showed a broad peak eluted at retention time (t_R) 19.5 min, with a right shoulder ending at t_R 22 min. Considering that the single-stranded d(T_6) and d(C_6) had t_R respectively equal to 20.8 and 20.4 min, and the G4 complex d(TG_4T)$_4$ had t_R equal to 19.1 min, we assume that 7 at pH 4.5 exists as a mixture of the tetramolecular i-motif complex and the unstructured random coil (responsible for the shoulder of the peak), in agreement with the CD and PAGE data.

The HPLC SEC profiles of DEL-5'-d(AC_4A)$_2$ (3) and DEL-3'-d(AC_4A)$_2$ (4) showed a peak at t_R 20.0 and 20.1 min, respectively, which can be reasonably assigned to the bimolecular i-motif complex as suggested by CD e PAGE data. However, the presence of the right shoulder ($t_R \approx 21$ min) and the peak at t_R 21.0 min, respectively for 3 and 4, indicate the concomitant presence in the solution of the unfolded DEL-CROs s 3 and 4. Further peaks at lower retention time (16.0–19.6 min, dotted square boxes in Fig. 35) indicated the formation of higher MW complexes likely belonging to the i-motif family. These findings are in good agreement with the PAGE data of 3 and 4 (Fig. 35, lane 6 and 5, respectively), which showed the presence of a strong band as the main product and a second slower pale band.

The HPLC-SEC profile of d(C_6) (8) annealed at pH 4.5 showed a single peak at t_R 19.0 min with a right shoulder ending at ≈ 21.0 min. This data agrees with the presence in the solution of the tetramolecular d(C_6)$_4$ i-motif which coexists with very low amount of the unfolded 8.

The HPLC-SEC profile of DEL-5'-d$(C_6)_2$ (5) showed three peaks with $t_R \leq 19.7$ min, likely attributable to the type G (Fig. 1) bimolecular i-motif (t_R 19.7 min) and higher MW analogs (t_R 18.6 and 16.5 min). Analogously, DEL-3'-d$(C_6)_2$ (6) showed peaks at 19.2, 17.8 (traces), and 16.0 min. However, differently from what was observed for 5, in the case of 6 the peak eluted at 16.0 min, attributable to higher MW complexes, was more intense than the peak of the bimolecular i-motif, thus indicating that the 3' linkage between the d(C_6) strands and the DEL favors the formation of higher-ordered structures.

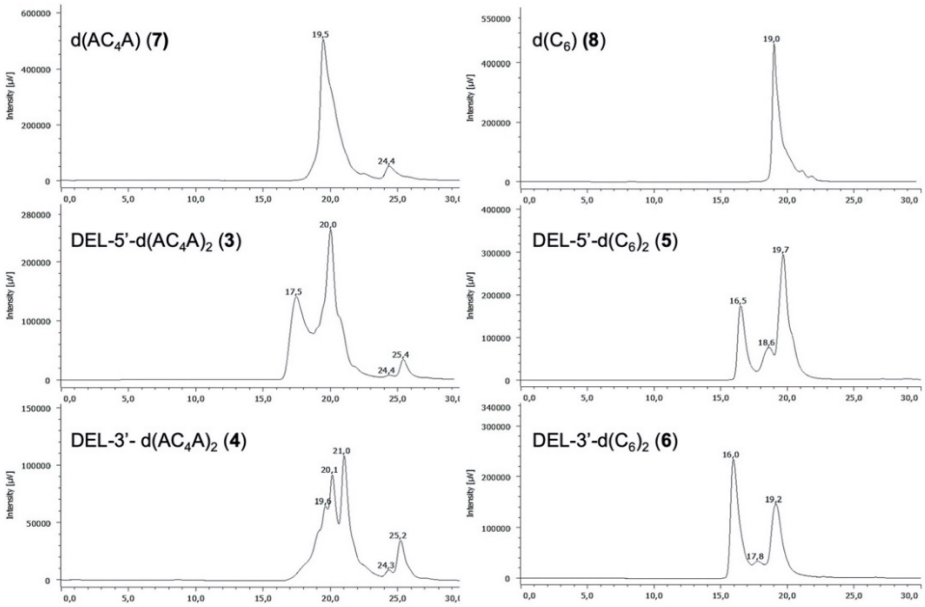

Figure 35 HPLC-SEC of 3–8 eluted with 100 mM K + phosphate buffer at pH 4.5.

NMR Studies

NMR studies have been largely employed to study the secondary structures formed by CROs. CROs containing four cytosines have been investigated in the formation of tetramolecular, bimolecular, and unimolecular i-motif complexes.

To further confirm the formation of i-motif structures by CROs 3–8 in near-physiological conditions, we recorded the ^{1}H NMR spectra of 3–8 annealed in 100 mM K^+-containing water buffer (90% H_2O/10% D_2O) whose pH was corrected to 4.5 and 7.0 to match the conditions used for CD and HPLC-SEC studies. Water-suppressed ^{1}H NMR spectra allow to confirm the presence in the solution of i-

motif structures by showing the i-motif diagnostic imino proton signals resonating at 15–16 ppm due to the formation of an H-bond between hemi-protonated C–C^+ base pairs. An additional broad signal at 8.00–10.00 ppm due to the H-bonded C4 amino protons of C–C^+ base pairs complete the NMR profiling of i-motif structures. The ^{1}H NMR spectrum of d(AC_4A) (7) at pH 4.5 (Fig. 36) showed the presence of two sharp singlets at 15.45 and 15.60 ppm and a weak broad signal at 15.49 ppm accounting for the presence of an i-motif structure containing at least two stable C-C^+ base pairs. The broad signal due to H-bonded amino protons resonating at 9.2–9.3 ppm further confirmed the formation of C-C^+ base pairs. The ^{1}H NMR spectrum of DEL-5'-d(AC_4A)$_2$ at pH 4.5 (3) showed the presence of two sharp singlets at 15.61 and 15.46 ppm, and two minor signals at 15.58 and 15.38 ppm, attributable to the H-bonded N3H imino proton of four C-C^+ base pairs. The broad amino proton signal at 9.3 ppm further supported the formation of the i-motif structure. The ^{1}H NMR spectrum of DEL-3'-d(AC_4A)$_2$ at pH 4.5 (4) resulted very similar to the one shown by 3. However, both the imino and the amino proton signals of 4 resulted less intense than those observed in the NMR spectrum of 3. It is to be noted that besides the enhancement of the i-motif melting temperature, the introduction of the DEL linker at the 5' or 3' end of 7 did not influence the topology of the resulting i-motif structures, as disclosed by the perfect superimposition of the two main imino protons observed in the NMR spectrum of 7, 3, and 4 (Fig. 36). In agreement with the CD evidence, the NMR spectra of 7, 3, and 4 registered at pH 7.0 did not show any signal attributable to i-motif structures (data not shown), thus confirming the unsuitability of the natural d(AC_4A) C-rich ODN and its DEL analogs to form any i-motif structure at neutral pH.

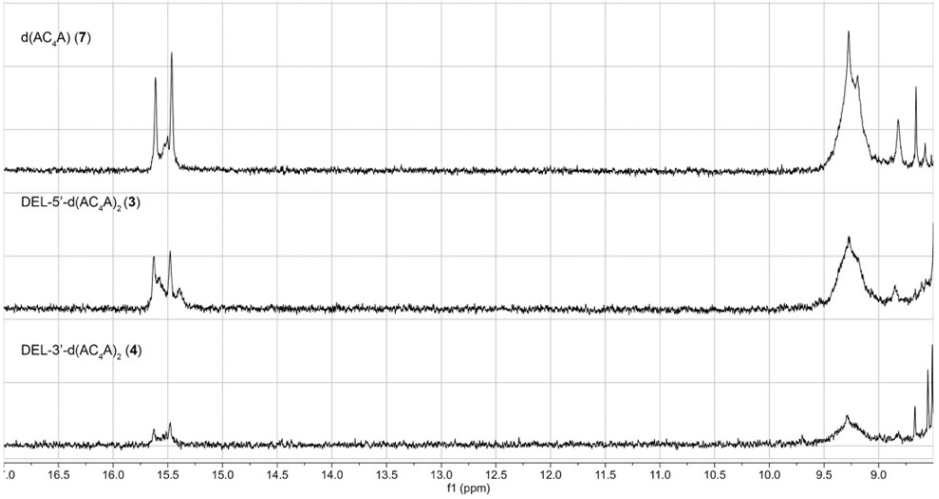

Figure 36 [1]H NMR spectra of 3, 4, and 7 in 100 mM K+ phosphate buffer at pH 4.5 (25 ◦ C, H 2 O/D 2 O 9:1).

The ^{1}H NMR spectrum of d(C_6) (8) recorded at pH 4.5 (Fig. 34) did not show any imino proton nor any C4-NH_2 amino proton signal. This finding was a bit surprising, considering that CD and HPLC-SEC data were indicative of i-motif formation. We attribute this unexpected behavior to the formation of insoluble higher MW aggregates promoted by the greater ODN concentration required for NMR and PAGE investigation (mM vs. μM concentration). The ^{1}H NMR spectra of DEL-5'-d(C_6)$_2$ and DEL-3'-d(C_6)$_2$ at pH 4.5 (5 and 6, respectively, in Fig. 37) displayed the presence of many imino proton signals in the region 15.4–15.8 ppm, including four sharp signals, which were indicative for the presence in solution of i-motif structures stabilized by four very stable C-C$^+$ base pairs. Together with the detection of a broad signal centered at 9.4 ppm (C_4-NH_2) and in agreement with CD, PAGE, and HPLC-SEC data, the NMR data further supported the formation at the acidic pH of stable i-motif structures likely corresponding to the bimolecular complexes. Differently from the NMR spectra of d(AC_4A)-containing C-rich samples recorded at pH 7.0, the NMR spectra of DEL-5'-d(C_6)$_2$ recorded at neutral pH clearly showed the i-motif characteristic exchange-protected imino and amino proton signals, thus confirming that the insertion of the DEL in suitable C-rich sequences can induce the formation of i-motif structures which, differently from their natural analogs, are stable enough to be detectable even at neutral pH.

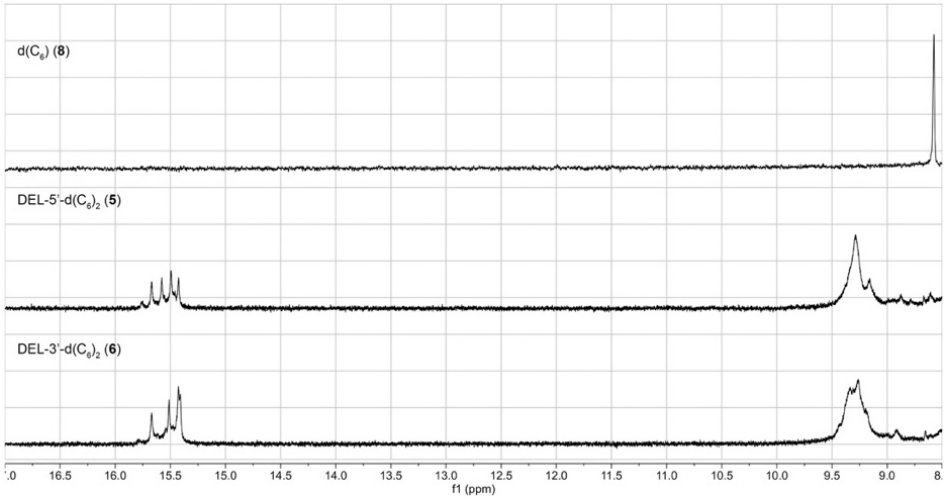

Figure 37 [1]H NMR spectra of 8, 5, and 6 in 100 mM K+ phosphate buffer at pH 4.5 (25 ◦ C, H 2 O/D 2 O 9:1).

DNA oligonucleotides represent an attractive building material to be used in supramolecular assembly and nanotechnology. DNA duplex, triplex, and G-quadruplex secondary structures have been extensively studied to construct desirable molecular or supramolecular scaffolds. DNA i-motif secondary structures enlarge the capability of the DNA toolbox to build new molecular architectures. It is noteworthy that i-motifs are pH-sensitive and can induce conformational changes as the pH varies. Some of these aspects are currently under investigation because of their biological relevance and to obtain pH-responsive structural switches in supramolecular buildings.

Here, we have reported new i-motif structures obtained by connecting two 6-mer C-rich ODN strands containing a run of four (7) or six (8) consecutive cytosines to the two arms of the non-nucleotide Double Ended Linker (DEL), which in previous studies has proved effective in promoting and stabilizing the formation of G-quadruplex structures [59]. We have demonstrated that the use of the DEL linker to obtain DEL-d(AC_4A)$_2$ 3 and 4, and DEL-d(C_6)$_2$ 5 and 6 has determined a considerable thermal stabilization of the resulting DEL-containing i-motif structures with respect to their natural counterparts at pH 4.5. We have also shown that, differently from the natural 8, which was unable to form any secondary structure at neutral pH, 5 and 6 can form stable i-motif structures also at pH 7.0.

Finally, considering the PAGE and HPLC-SEC evidence pointing towards the formation of higher-order aggregates, the here reported results open the way to obtaining new pH-sensitive supramolecular biomaterials based on the i-motif architecture.

Conclusion

DNA oligonucleotides represent an attractive building material to be used in supramolecular assembly and nanotechnology. i-Motif structures, discovered for the first time in 1963 (DOI: 10.1021/bi00902a028), have attracted considerable interest because of their possible implication in biological processes, such as the telomers and centromeres formation, and as transcriptional regulators (DOI: 10.1093/nar/gky735). It was reported that C-rich DNAs are bound by proteins, such as the poly-C-binding proteins (PCBP), and, interestingly, when structured in i-motif, they can bind proteins belonging to the heterogeneous nuclear ribonucleoprotein (hnRNP) family (DOI: 10.1021/jacs.6b11825). i-Motif-containing aptamers have been used to specifically bind cells by exploiting the peculiarities of cellular pHs (*DOI:10.1021/jacs.8b08047).*
Furthermore, ultra-pH-responsive i-motif aptamers were employed in sensing technologies developed to specifically achieve imaging of different cancer types *in vitro* and *in vivo* by exploiting the slight differences in extracellular pH values of different cancers (DOI: 10.1039/c8cc04420a). i-Motifs have been considered potential building blocks for constructing supramolecular assemblies in DNA nanotechnology (dx.doi.org/10.1021/ja3118224 | J. Am. Chem. Soc. 2013, 135, 1593−1599).
DNA i-motif secondary structures enlarge the capability of the DNA toolbox to build new molecular architectures. It is noteworthy that i-motifs are pH-sensitive and can induce conformational changes as the pH varies. Some of these aspects are currently under investigation because of their biological relevance and to obtain pH-responsive structural switches in supramolecular buildings.
Here, we have reported new i-motif structures obtained by connecting two 6-mer C-rich ODN strands containing a run of four (7) or six (8) consecutive cytosines to the two arms of the non-nucleotide Double Ended Linker (DEL). The use of the DEL linker to obtain DEL-d(AC4A)2 3 and 4, and DEL-d(C6)2 5 and 6 has determined a considerable thermal stabilization of the resulting DEL-containing i-motif structures with respect to their natural

counterparts at pH 4.5. We have also shown that, differently from the natural 8, which was unable to form any secondary structure at neutral pH, 5 and 6 can form stable i-motif structures also at pH 7.0. The here reported results open the way to obtaining new pH-sensitive supramolecular biomaterials based on the i-motif architecture.

Experimental section

DNA synthesis and purification

The ODNs 3-6 were chemically synthesized using CPG-sulphone-resin 1. 45 mg/mL solution of phosphoramidite 9 (in anhydrous CH_3CN) was used for the synthesis support 2. The syntheses continued with reactions with nucleotide 5'-phosphoramidite (for DEL-ODNs 3 and 5) and with 3'-phosphoramidite (for DEL-ODNs 4 and 6). ODNs 7 and 8 were synthesized by standard amidite protocols for DNA synthesis. The solid support was then treated with concentrated aqueous ammonia for 7 h at 55 °C. The filtered solution was concentrated under reduced pressure and purified by HPLC over an anion exchange column, using a linear gradient of buffer B in buffer A (0 to 100% in 30 min.). Buffer A: 20 mM NaH_2PO_4, pH 7.0 containing 20% CH_3CN; buffer B: 1 M NaCl, 20 mM NaH_2PO_4, pH 7.0, containing 20% CH_3CN; flow rate 1 mL/min. The dried products were desalted over a gel filtration column eluted with H_2O/ethanol (9:1, v/v). After lyophilization, pure ODNs 3-8 were obtained. The ODN amounts were determined spectrophotometrically in water at λ = 260 nm (T = 90 °C) using a molar extinction coefficient ε = 113,200 $cm^{-1}M^{-1}$ for DEL-d$(AC_4A)_2$; ε = 86,800 $cm^{-1}M^{-1}$ for DEL-d(C_6); ε = 56,600 $cm^{-1}M^{-1}$ for d(AC_4A) and ε = 43,400 $cm^{-1}M^{-1}$ for d(C_6); calculated for the unstacked ODNs by the nearest-neighbor method.
ODN 7: ESI-MS (*m/z*) calcd. for $[M - 2H]^{2-}$ 859.6, found 859.5. DEL-ODN 3: ESI-MS (*m/z*) calcd. for $[M - 4H]^{4-}$ 982.6, found 982.0; calcd. for $[M - 5H]^{5-}$ 785.9, found 786.1. DEL-ODN 4: ESI-MS (*m/z*) $[M - 4H]^{4-}$ 982.6, found 982.0; calcd. for $[M - 5H]^{5-}$ 785.9, found 786.0; $[M - 7H]^{7-}$ 561.1, found 561.4. ODN 8: ESI-MS (*m/z*) calcd. for $[M - 2H]^{2-}$ 835.6, found 835.0. DEL-ODN 5: ESI-MS (*m/z*) calcd. for $[M - 4H]^{4-}$ 958.6, found 958.0; calcd. for $[M - 5H]^{5-}$ 766.7, found 766.9. DEL-ODN 6: ESI-MS (*m/z*) $[M - 4H]^{4-}$ 985.6, found 985.0; calcd. for $[M - 5H]^{5-}$ 766.7, found 766.9; $[M - 7H]^{7-}$ 547.3, found 547.6.

Annealing procedure

The lyophilized ODNs 3–8 were dissolved in ultrapure water containing 90 mM KCl and 10 mM KH_2PO_4 (100 mM K^+ buffer). The pH was adjusted at 4.5 and 7.0 using HCl and KOH, respectively. The ODNs were annealed by heating to 90 °C for 5 min and then slowly cooled to room temperature over 12 h (annealing procedure). All samples were stored at 5 °C for 24 h (or more) before analyses. The solutions were equilibrated at 25 °C for 2 h before performing the experiments.

CD experiments

CD spectra and CD melting profiles were acquired in the range 220–320 nm at 25 °C using quartz cuvettes of 0.1 cm optical path in 100 mM K^+ buffer (pH 4.5 and 7.0) at the final single strand concentration of 20 μM. All CD spectra were averaged over four scans recorded at 200 nm/min scanning speed, 1 s response time, and 2 nm bandwidth. The buffer baseline was subtracted from each spectrum. The CD melting experiments were performed by monitoring the CD value of the higher positive Cotton effect in the temperature range 5–90 °C at the 0.5 °C/min heating rate.

PAGE analysis

Native gel electrophoresis experiments were performed on 18% polyacrylamide gels containing TAX 1× (40 mM Tris, 40 mM acetate, 1 mM EDTA, Sigma-Aldrich, St. Louis, MO, US) pH 4.5, at 5 °C, 120 V for 2 h. Samples were loaded at a final ODN concentration of 20 μM; glycerol (10%) was added to facilitate sample loading in the wells. After placing the gel on a PLC silica gel 60 F_{254}, 1.0 mm thickness, 20 cm × 20 cm glass plate, the bands were visualized by exposition to UV light (λ = 254 nm).

HPLC-Size Exclusion Chromatography (HPLC-SEC) Analyses

HPLC-SEC analyses and purifications were performed using a Phenomenex (Bologna, Italy) Yarra SEC-2000 column (300 × 7.8 mm, 3 μm) operating in the MW range of 1000–300,000 Dalton. The column was eluted with 90 mM KCl and 10 mM KH_2PO_4/CH_3CN

(80:20, v/v, pH 4.5), flow rate 0.6 mL/min, UV-detector at 260 nm. All analyses were performed at 25 °C.

Nuclear Magnetic Resonance (NMR)

One-dimensional NMR spectra were acquired as 16,384 data points with a recycle delay of 1.0 s at 25 °C, and the spectra were apodised with a shifted sine bell squared window function. Water suppression was achieved by including a double pulsed-field gradient spin-echo (DPFGSE) module in the pulse sequence prior to acquisition [60,61]. NMR samples were prepared at 1.0 mM single strand concentration in 200 μL of 90 mM KCl and 10 mM KH_2PO_4 in H_2O/D_2O 9:1, whose pH was corrected to 4.5 or 7.0 with aqueous HCl.

Objective 2 Spectroscopic and computational investigation of the binding of the c-myc oncogene NHE III1 region by the phytochemical polydatin (Publication n°3)

Trans-polydatin (tPD), the 3-β-D-glucoside of trans-resveratrol, is a natural polyphenol with documented anti-cancer, anti-inflammatory, cardioprotective, and immunoregulatory effects. Considering the anticancer activity of tPD, in this work we aimed at exploring the binding properties of this natural compound with the G-quadruplex (G4) structure formed by the Pu22 [d(TGAGGGTGGGTAGGGTGGGTAA)] DNA sequence by exploiting CD spectroscopy and molecular docking simulations. Pu22 is a mutated and shorter analogue of the G4-forming sequence known as Pu27 located in the promoter of the c-myc oncogene, whose overexpression triggers the metabolic changes responsible for cancer cells transformation. In silico molecular docking study indicated that the interaction of tPD with Pu22 G4 involves end-stacking to the terminal G-quartet and H-bonding interactions between the sugar moiety of the ligand and deoxynucleotides not included in the G-tetrads. Finally, we compared the experimental CD profiles of Pu22 G4, with the corresponding theoretical output obtained using DichroCalc, a web-based server normally used for the prediction of proteins' CD spectra starting from their ".pdb" file. The results indicated a good agreement between the predicted and the experimental CD spectra in terms of spectral bands' profile even if with a slight bathochromic shift of the positive band, suggesting the utility of this predictive tool for G4 DNA CD investigations.

Remarkably, the promoter region of c-myc – an oncogene over-expressed in the majority of solid tumors and closely associated with cancer cell apoptosis, proliferation, invasion, cell-cycle arrest, and metastasis – can form a parallel G4 structure via Hoogsteen hydrogen bonds under specific conditions,and has been proposed as an effective target for antitumor drugs[24-26]. Particularly, it was found that molecules capable of binding and stabilizing this type of G4 downregulate the expression of c-myc, finally resulting in the apoptosis of cancer cells with great benefit in anticancer therapy[18-22].Trans-polydatin (tPD, Figure 35a) the 3-β-D-glucoside of the well-known nutraceutical trans-resveratrol[23], is a natural polyphenol with documented anti-cancer, anti-inflammatory, cardioprotective, and immunoregulatory effects[24-25]. In a recent work, the G4-binding of

tPD was explored toward three cancer-related G-rich DNA sequences, including c-myc, in comparison with a model duplex[26]. Interestingly, tPD displayed a clear binding ability with all the G4s and a higher ability, respect to its aglycone derivative trans-resveratrol, to discriminate G4 over duplex DNA. Moreover, in vitro assays on melanoma cells proved that tPD significantly reduced telomerase activity, and inhibited cancer cell proliferation[26]. However, the adopted experimental conditions did not allow to detect any significant conformational changes of the analyzed G4 DNA upon binding with tPD. Moreover, it was not possible to estimate thermal stability of both c-myc and its complex with tPD, as needed for evaluating any stabilizing or destabilizing effects of the polyphenol on the G4-folded c-myc promoter[26]. On the other hand, other studies clearly indicated that the anticancer effects (including inhibition of cell proliferation and metastasis) of tPD took place through suppressing the c-myc expression, as proven in a model of human cervical cancer[27]. Therefore, conscious of the role of G4-structure binding and stabilization by ligands in c-myc deregulation we decided to examine in more detail the molecular recognition of c-myc G4 by tPD through an approach differing from the previously reported in the literature from both experimental and in silico perspectives. To this aim, the interaction of tPD with c-myc DNA was studied in the present work focusing on the G4 structure formed by Pu22 region having the sequence 5′-TGAGGGTGGGTAGGGTGGGTAA-3′, a mutated and shorter analogue of the sequence known as Pu27 located in the promoter of the c-myc oncogene and associated with the regulation of promoter activity and gene transcription.

Circular dichroism (CD) spectra of Pu22, either unliganded or in complex with the tPD, were recorded at variable temperatures in a buffer containing a lower concentration of potassium ions than previously reported[27]. Being aware of the utility of molecular docking in identifying DNA ligands through verification of the favored binding sites in a complex, and in the estimation of the binding affinity, the c-myc G4 binding affinity with tPD was studied by docking experiments. The CD spectrum of the parallel G4 structure of Pu22 was further predicted by DichroCalc software[28], with the aim to verify whether the experimental profile could be reproduced by simulation as described below.

The combination of experimental and computational work started from the examination of the CD spectral features of Pu22 DNA and

its complex with tPD. Moreover, a thermal denaturation study was conducted with both unliganded Pu22 and tPD-Pu22. The observations from CD spectroscopy were then interpreted in the light of the docking experiments performed by us on tPD-Pu22, but also on (tPD-Pu22)-Pu22, $(Pu22)_2$, and tPD-$(Pu22)_2$ molecular systems.

CD spectroscopic analysis of the binding of Pu22 by tPD

With the aim to shed light on the possible mechanisms underlying the previously-reported anticancer activity of tPD, the potential of this polyphenol in binding Pu22 was evaluated. The CD study displayed a spectrum for Pu22 corresponding to a G4 with parallel topology, as identified by the characteristic positive band at ~265 nm and the negative one at 240 nm (Figure 34b, black line). In the presence of the polyphenol, we observed an increase of the positive CD signal at 263 nm accompanied with a 1-nm red-shift of the band maximum, and a concomitant reduction of the CD minimum at 240 nm (Figure 34 b, red line). Also, some differences in the CD spectra were evidenced in the 280-300 nm region. Overall, in the studied conditions tPD induced a greater degree of structuration in the Pu22 G-quadruplex, as evidenced by the “difference” CD spectrum obtained by subtracting the CD spectrum of the Pu22 G4 to that of the tPD-Pu22 complex (inset of Figure 34b).

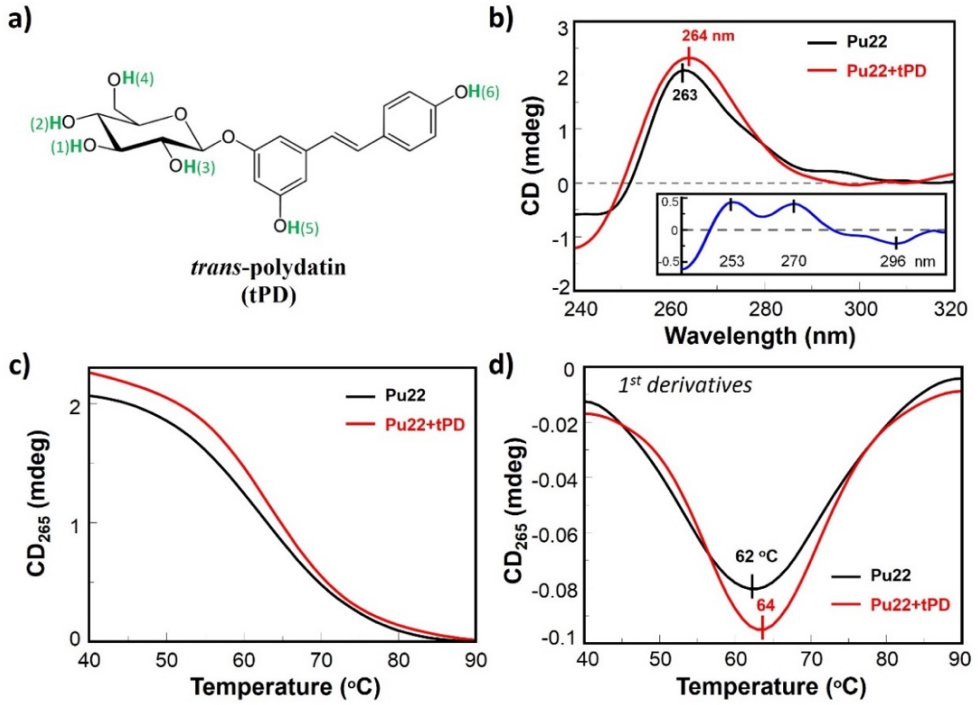

*Figure 29. (**a**) Chemical structure of tPD; some atoms are numbered as in the docking program. **(b)** CD spectra of Pu22 2.5 μM (black) and its complex with tPD (red) at 40 °C. In the inset the "difference" CD spectrum [tPD-Pu22 (mdeg) – Pu22 (mdeg)]. **(c)** CD thermal denaturation curves [CD_{265} (mdeg) vs. T (°C)] and **(d)** their first derivatives vs. T plots for Pu22 (2.5 μM, black) and its complex with tPD (red). All experiments were run in PBS, pH 7.4 (optical path length = 0.1 cm).*

Then, we studied the effect of tPD on the stability of this G4 DNA by recording, for Pu22 and its mixture with the polyphenol, the CD values at 265 nm as a function of temperature (Figure 34 c). We found a slight thermal stabilization in the presence of tPD, detectable by the increased value of the G4 melting temperature (T_m = 64 °C) with respect to the unliganded Pu22 G4 reference (T_m = 62 °C), leading to a ΔT_m of +2 °C (Figure 34 d and Table 9). Furthermore, the overall variation of the CD signal at the λ_{max} upon heating, i.e., between 40 (folded state) and 90 °C (unfolded), for Pu22 alone or in complex with tPD, was 1.99 and 2.23, respectively, again confirming a higher structuration degree of the quadruplex when bound by the ligand. Specifically, the highest difference in the ΔCD for the two systems was evidenced between 40 and 50 °C (Figure 34, black-line dashed squares, and Table 8). Some differences between the two systems were also detected in the CD spectra recorded at the

various temperatures in the 280–300 nm spectral region (Figure 35 a,c).

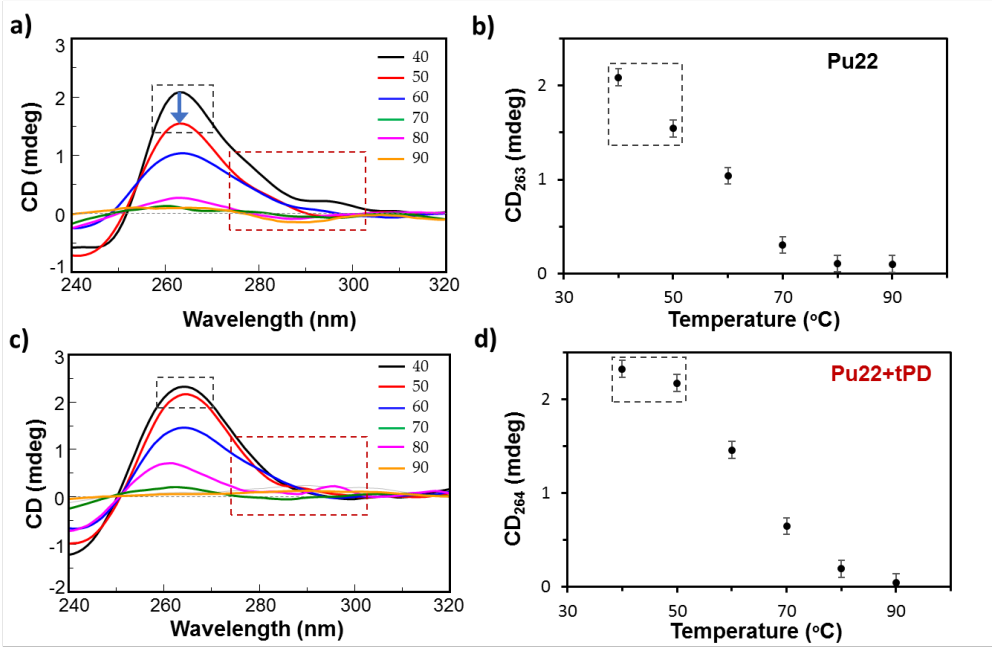

*Figure 30 CD spectra of Pu22 (2.5 μM) **(a)** and its complex with tPD **(c)** recorded in the 40-90 °C temperature range. Plots of the CD signal at λ_{max} (in mdeg) vs. temperature (in °C) for Pu22 **(b)** and its complex with tPD **(d)** derived from panels **a** and **c**. All experiments were run in PBS, pH 7.4 (optical path length = 0.1 cm).*

Entry	ΔT_m* (°C)	$\Delta CD_{max\ 40–90}$ (mdeg)	°C $\Delta CD_{max\ 40–50}$ (mdeg) °C
Pu22	0	1.99	0.54
tPD-Pu22	+2	2.23	0.15

Table 8 Summary of the CD and CD melting data for Pu22 and the complex tPD-Pu22. ΔT_m is the variation of the melting temperature of the complex with respect to the Pu22 reference; $\Delta CD_{max\ 40-90}$ is the difference in the CD value at the λ_{max} between 40 (folded state) and 90 °C (unfolded); whereas $\Delta CD_{max\ 40-50}$ is the one between 40 and 50 °C.

* T_m Pu22 = 62 °C

Molecular Docking studies

In this context we used herein in silico methods, and more specifically molecular docking, in analogy to other recent literature examples using polyphenols as anticancer drug candidates, to deeper analyze the interaction between tPD and the target Pu22 G4,

whose sequence is located in a regulatory region of the c-myc oncogene. More in detail, we exploited the Hdock software for the computational studies involving DNA. Hdock is used for both macromolecule-macromolecule and small molecule-macromolecule dockings, including those involving DNA and RNA G4. It is worth noting that the docking software provides dimensionless scores (Hdock scores) that are correlated to binding affinities. This allows to compare the binding affinity of ligands for a given target by simply comparing their docking scores, with the most negative values being associated to the highest affinity ligands. We found by Hdock docking that tPD bound the G4 target in proximity of the G4, G8, G13, and G17 nucleotides (Figure 36, Table 9). Comparing the Hdock scores for the top-1 poses, we can predict that the ligand bound Pu22 with a lower affinity than its aglycone resveratrol (tRES, Table 8), as experimentally shown in the literature.

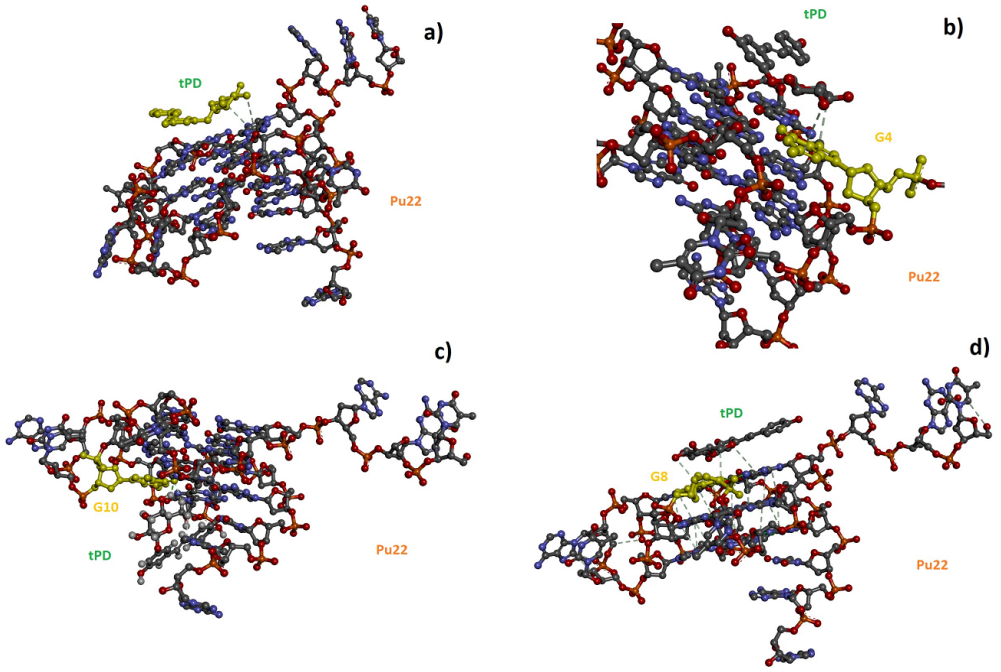

*Figure 31 The docked structures of the tPD-Pu22, with the Pu22 PDB ID: 6AU4, corresponding to the top 1–3 ranked poses: **(a,b)** pose 1; **(c)** pose 2; **(d)** pose 3. Note how in all three cases tPD seems to interact by end-stacking and H-bondings with the nucleotides represented in yellow in panels **b**, **c**, and **d**.*

The interactions emerged by analyzing the top 1–3 poses are held by H-bondings with aromatic rings involving the tPD H1 (Figure 37a) and the guanine residues 4 (3.15 Å, ligand H1–G-ring; π donor H-

bond) and 8 (3.05 Å, ligand H1–G ring; π donor H-bond), respectively in pose 1 and 3 (Figure 37 b,d). In the pose 2, a H-bond between ligand H2 (Figure 37a) and the O6 (2.14 Å) of the guanine residue 10 was also detected (Figure 37c). Interestingly, in poses 1 and 3 the tPD aromatic moieties tend to lay almost parallel to the terminal quartets of the quadruplex (Figure 37), suggesting thus an end-stacking interaction of the polyphenol to the G4.

Complex	HDOCK score* top-1 ranked pose	HDOCK score mean value (top 1–3 poses) ± SD	Interface residues
tPD/Pu22	–112.1	–111.7 ± 0.3	G4, G6, G8, G10, G13, G15, T16, G17, G19, T20, A21
tRES/Pu22	–120.6	–112.9 ± 7.3	G6, T7, G10, G15, T16, G19,T20, A21
tPD/(Pu22)$_2$	–103.2	–102.7 ± 0.5	G6, G10, T11, G15, T16, G19, T20, A21, G'14, G'15, T'16, G'17, G'18, G'19, T'20, A'21

Table 9 HDOCK docking scores (for the top-ranked pose and mean value from the top-1–3 poses). The interface nucleotide residues within 5.0 Å from the ligand in the top-1–3 complexes are reported in the last column.

* The docking energy scores.

The dimerization of Pu22 G4 was described in the literature under some conditions; for example, a quadruplex dimer was clearly evidenced in the solid state, whereas in solution this G4 is present mainly as monomer. Nonetheless, Jana and Weisz using non-denaturing polyacrylamide gel electrophoresis showed that in solution *MYC*-Δ1,6 and, albeit to a much lesser extent, Pu22 (indicated by them as '*MYC*-Δ1,6[1.2.1]', carrying two G replacements by T with respect to *MYC*-Δ1,6) presented dimeric forms corresponding to slower migrating bands, more evident in the former case and somewhat faint, but still detectable, in the case of Pu22. Similarly, the electrophoretic assays of Moriyama et al. showed for Pu22 (indicated by them as c-myc) a main band and two slower migrating bands. The presence of dimeric Pu22 in solution was suggested also by size exclusion chromatography (SEC)

revealing two main SEC peaks for the Pu22 solution that led to hypothesize the coexistence of monomeric and dimeric forms in solution. Therefore, we hypothesize that Pu22 in solution is found mainly as monomer, which justifies its usage in biomolecular studies as a model of G4 DNA not prone to undesirable multimerization, but also, albeit at a much lesser degree, as dimer. G4 DNA dimer binding by ligands could in principle alter the monomer-dimer equilibrium, and importantly some ligands can induce dimerization of truncated parallel c-myc G-quadruplexes.

With all the above considerations in mind, we decided to explore by molecular docking also the propensity of tPD to bind the $(Pu22)_2$ dimer model. We found for the top-ranked pose, as well as the poses 1–3 of this docking, higher Hdock scores (–103.2 and –102.7 ± 0.5, respectively; Table 8) with respect to those found in the case of the docking of the same ligand with the monomeric G4 (–112.1 and –111.7 ± 0.3), suggesting a slightly higher affinity of tPD for the most abundant monomeric form of Pu22 G4 structure.

We also performed DNA-DNA dockings to explore the dimerization of Pu22 G-quadruplex to get $(Pu22)_2$ and the effects of tPD on this process. To this scope, in the first case we docked Pu22 G4 to a second Pu22 G4 unit, set as target (Figure 41 a), while in the second docking we used the pre-docked tPD-Pu22 G4 for docking to a second Pu22 G4 unit (Figure 37b). We found that tPD-Pu22 G4 binds Pu22 G4 with an affinity 1.3 times lower than that showed by unliganded Pu22 G4 with the same target [Hdock scores (mean of top 1–3 values): –460.1 ± 14.1 vs. -601.3 ± 7.3, respectively]. In other terms, it seems that tPD hinders Pu22 G4 dimerization that in its absence is more favored (Figure 38 a,b), and binds Pu22 G4 monomer with slightly higher affinity than the dimeric $(Pu22)_2$ G4 (Figure 37 b,d).

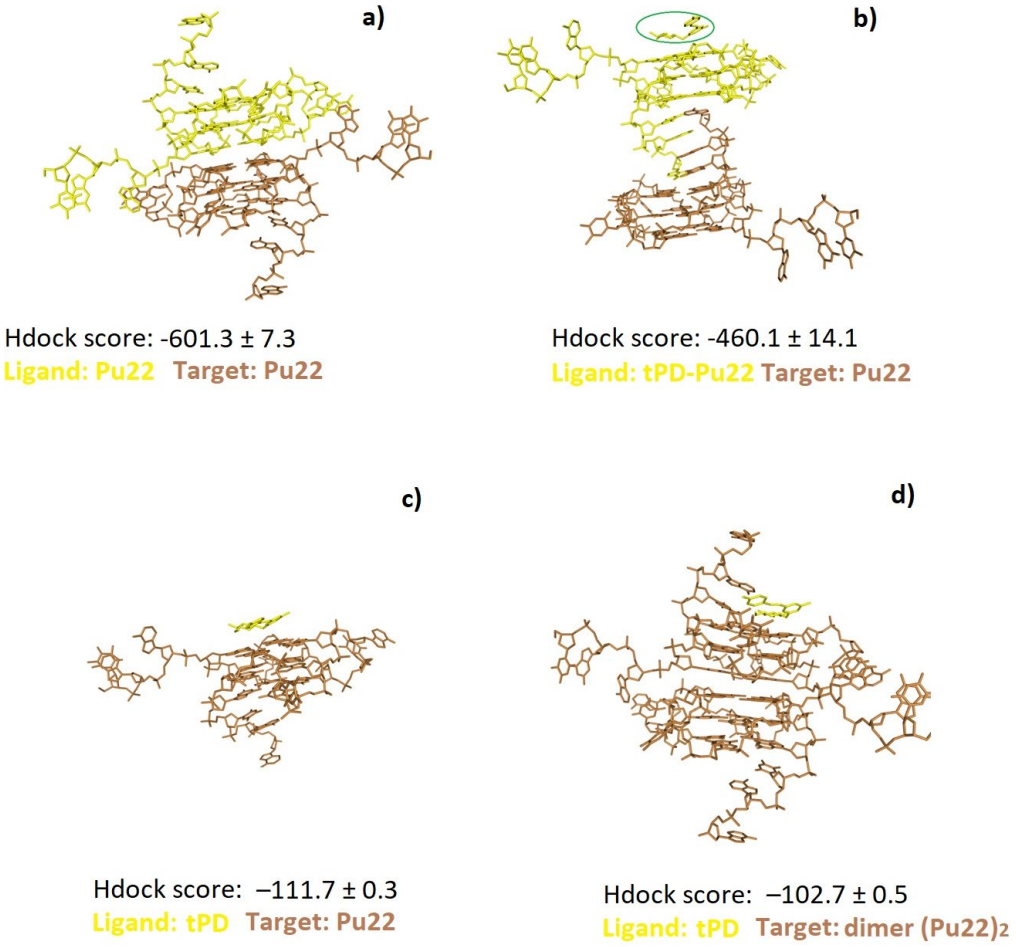

*Figure 32 Docking of Pu22 (**a**) or tPD-Pu22 (**b**) to another Pu22 unit. Docking of tPD to Pu22 monomer (**c**) or dimer (**d**). Hdock scores (mean of top 1–3 values) were also indicated.*

Remarkably, the dimeric form of Pu22 G4 with tPD (Figure 38b and 37a) was predicted to show considerable structural differences with respect to the unliganded $(Pu22)_2$ G4 dimer (Figure 37a). In this regard, it is worth noting how 18 hydrophobic/π-π stacking Pu22-Pu22 intermolecular interactions (pink, Figure 37b) alongside with six intermolecular H-bonds (green) are predicted to sustain the trimeric complex structure.

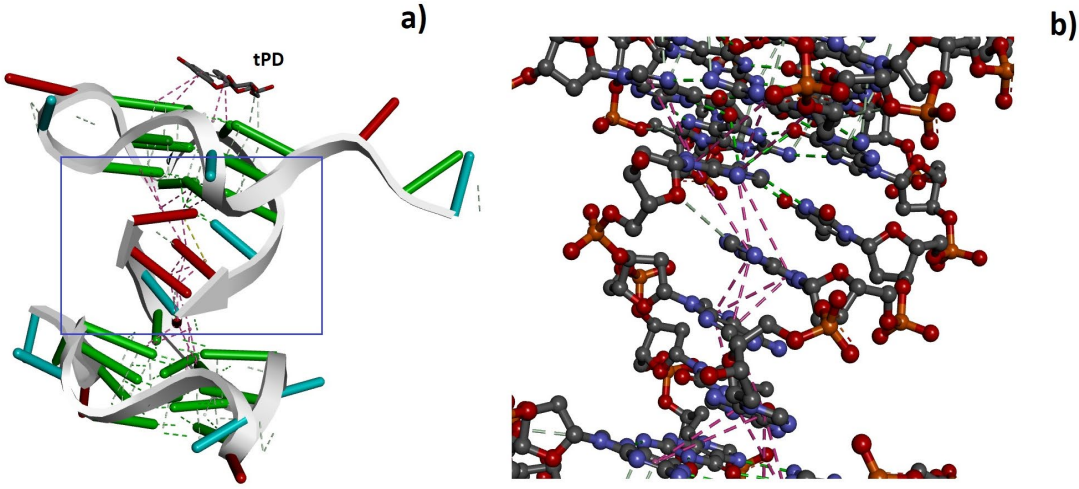

Figure 33 ***(a)*** *Detailed pose view of the trimeric complex (tPD-Pu22)-Pu22 of Figure 4b; tPD structure is indicated.* ***(b)*** *Enlargement of the area delimited by the blue rectangle.*

CD predictions and comparison with experimental spectroscopic data

Furthermore, the solution NMR structure of the monomeric model of Pu22 G4 formed in human c-myc promote, was used to simulate its CD spectrum by DichroCalc. This software is routinely used for obtaining simulated CD spectra of proteins starting from their PDB structure files. In our approach, we applied the method to the prediction of the spectroscopic profile of the G4 structure object of our study. In particular, a positive band at 268 nm and a negative one at 244 were predicted by DichroCalc (Fig. 39a), which were to some extent in analogy to what we experimentally found by CD (Fig. 39b) and was previously described in the literature for the parallel G4 structure of Pu22**,** though with a bathochromic shift of the bands by about 5 nm.

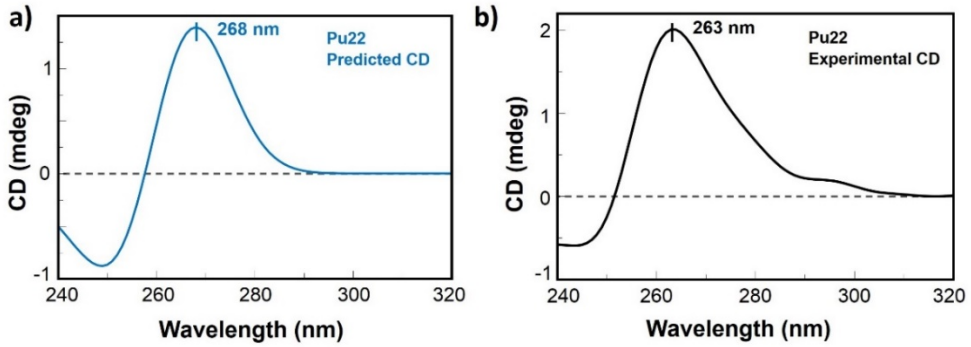

Figure 34 Theoretical CD spectrum of Pu22 G4 ***(a)*** *as simulated by DichroCalc* ***[45]*** *using the PDB ID 1XAV, compared with the experimental counterpart* ***(b)*** *obtained for Pu22 at 2.5 μM in PBS.*

Here, we described a combined approach including in silico (molecular docking) and experimental (CD binding assay/CD thermal denaturation) analyses, through which we verified that tPD can interact with Pu22, a G4-forming sequence related to the promoter region of the c-myc oncogene, stabilizing this DNA structure. The tPD anticancer activity previously observed in vitro, well correlates with its stabilizing effects on this cancer-related target. The interaction of tPD with the parallel quadruplex has been proven by CD, showing changes in the CD spectrum of this DNA secondary structure under our experimental conditions, especially in the characteristic positive band centred at 263 nm. Moreover, thermal stabilization effects on the G4 by tPD has been revealed by CD melting studies. The binding with the DNA structure has been described in more detail in silico by molecular docking which suggests that the interaction of tPD with Pu22 G4 may take place through end-stacking to the terminal quartet and involves deoxynucleotides placed in the external regions of the G4 and the sugar moiety of the ligand. Finally, the exploitation of the DichroCalc web-based server, normally used for the prediction of CD spectra of proteins, for the computation of CD spectra of Pu22 revealed the feasibility of the method for the predictions of CD spectra of G4 DNA.

Experimental Section

CD studies

Circular dichroism (CD) spectra were registered with procedures similar to previous literature reports [66] on a Jasco J-810 (Jasco Europe S.R.L., Cremella, Italy) spectropolarimeter, equipped with a Peltier ETC-505 T temperature controller, in a Hellma (Milan, Italy) quartz cell with a light path of 0.1 cm. The spectra were recorded within the 240–320 nm wavelength range and corrected subtracting the contribution of the solvents. All experiments were performed in PBS buffer (137 mM NaCl, 2.7 mM KCl, 10 mM Na_2HPO_4, and 1.8 mM KH_2PO4, pH 7.4; Sigma Aldrich, Milan, Italy), using 2.5 μM DNA (Pu22), diluted from the stock solution in water, and 125 μM tPD (50 equiv. respect to the DNA), diluted from the stock solution in DMSO.

CD denaturation studies

All G4-containing solutions were annealed by heating them at 95 °C for 5 min and then letting them to slowly cool down to room temperature (over 16 h). The presented melting curves (obtained recording CD_{265nm} *vs* T in the 40–90 °C temperature range) are representative of three independent experiments. Melting temperature (T_m) values were determined as the temperatures relative to minima of the 1st derivative plots of the denaturation curves. All experiments were repeated at least three times and all spectra were recorded in triplicate.

Molecular docking

We conducted our blind molecular docking with the program HDOCK [50, 51] using default parameters for all dockings and the PDB entry 6AU4 that is suitable for studies involving dimerization (selecting one of the two G4 monomers) of Pu22 G4 structure [56]. HDOCK server uses the iterative knowledge-based scoring function ITScore-PP to rank the top ten poses provided after each docking run. HDOCK score furnished by the program is an energy score whose values are listed dimensionless and larger negative numbers of HDOCK score indicate stronger binding interactions between the interacting ligand/macromolecules, which was reported to correlate well to experimental binding affinities.

The HDOCK server used as 3D structure of the Pu22 DNA that with the PDB (Protein Data Bank) ID: 6AU4 [56]. The 3D structure, including H-atoms, for the natural compound trans-polydatin was retrieved by us from the PubChem database (https://pubchem.ncbi.nlm.nih.gov/, accessed on 8th November 2021). More details on HDOCK docking server and on the procedures for docking experiments can be found at http://hdock.phys.hust.edu.cn/ (accessed on November 9th, 2021). We analyzed the top-ranked pose (Top-1) and the top three ranked poses for the complexes predicted by HDOCK according to the energy scores provided by the program as explained in the Results section. Ligand/DNA complexes were visualized by Discovery studio software [67] that was used also to analyzing H-bonding between tPD and G4 DNA.

CD predictions

The prediciton of the CD spectrum of the monomeric Pu22 G4 structure was performed using the DichroCalc web server starting from the PDB file of the NMR structure deposited with PDB ID 1XAV. At first the 1XAV.pdb file was manually edited by replacing the unrecognized ‘DA, DC, DG, DT’ text for deoxyribonucleotides with ‘A, C, G, T’. Then, the edited PDB file was uploaded as the input file in DichroCalc obtaining the predicted CD spectrum file which was edited with SpectraGryph 1.2. The predicted CD spectrum from the ‘ds’ format was finally visualized in Jasco Spectra Manager (JASCO Corporation, Sendai, Japan).

Conclusion

A combined approach including in silico (molecular docking) and experimental (CD binding assay/CD thermal denaturation) analyses was proposed for verifing that tPD can interact with Pu22, a G4-forming sequence related to the promoter region of the c-myc oncogene, stabilizing this DNA structure.The interaction of tPD with the parallel quadruplex has been proven by CD, showing changes in the CD spectrum of this DNA secondary structure under the tested experimental conditions, especially in the characteristic positive band centred at 263 nm. Moreover, thermal stabilization effects on the G4 by tPD has been revealed by CD melting studies. In silico description of the binding with the DNA structure suggests that the interaction of tPD with Pu22 G4 takes place through end stacking to the terminal quartet and involves deoxynucleotides placed in the external regions of the G4 and the sugar moiety of the ligand. Finally, the exploitation of the DichroCalc web-based server, normally used for the prediction of CD spectra of proteins, for the computation of CD spectra of Pu22 revealed the feasibility of the method for the predictions of CD spectra of G4 DNA.

References

1. Wu, T. te. *SECONDARY STRUCTURES OF DNA*; 1969; Vol. 19.
2. Ma, Y.; Iida, K.; Nagasawa, K. Topologies of G-Quadruplex: Biological Functions and Regulation by Ligands. *Biochem Biophys Res Commun* 2020, *531* (1), 3–17. https://doi.org/10.1016/j.bbrc.2019.12.103.
3. Riccardi, C.; Napolitano, E.; Platella, C.; Musumeci, D.; Montesarchio, D. G-Quadruplex-Based Aptamers Targeting Human Thrombin: Discovery, Chemical Modifications and Antithrombotic Effects. *Pharmacology and Therapeutics*. Elsevier Inc. January 1, 2021. https://doi.org/10.1016/j.pharmthera.2020.107649.
4. Hänsel-Hertsch, R.; di Antonio, M.; Balasubramanian, S. DNA G-Quadruplexes in the Human Genome: Detection, Functions and Therapeutic Potential. *Nat Rev Mol Cell Biol* 2017, *18* (5), 279–284. https://doi.org/10.1038/nrm.2017.3.

5. Balasubramanian, S.; Neidle, S. G-Quadruplex Nucleic Acids as Therapeutic Targets. *Current Opinion in Chemical Biology*. June 2009, pp 345–353. https://doi.org/10.1016/j.cbpa.2009.04.637.
6. *LETTERS TO NATURE h*; 1993.
7. Yang, H.; Zhou, Y.; Liu, J. G-Quadruplex DNA for Construction of Biosensors. *TrAC - Trends in Analytical Chemistry*. Elsevier B.V. November 1, 2020. https://doi.org/10.1016/j.trac.2020.116060.
8. Bhattacharyya, D.; Arachchilage, G. M.; Basu, S. Metal Cations in G-Quadruplex Folding and Stability. *Frontiers in Chemistry*. Frontiers Media S. A 2016. https://doi.org/10.3389/fchem.2016.00038.
9. Popenda, M.; Miskiewicz, J.; Sarzynska, J.; Zok, T.; Szachniuk, M. Topology-Based Classification of Tetrads and Quadruplex Structures. *Bioinformatics* 2020, *36* (4), 1129–1134. https://doi.org/10.1093/bioinformatics/btz738.
10. Riccardi, C.; Napolitano, E.; Platella, C.; Musumeci, D.; Montesarchio, D. G-Quadruplex-Based Aptamers Targeting Human Thrombin: Discovery, Chemical Modifications and Antithrombotic Effects. *Pharmacology and Therapeutics*. Elsevier Inc. January 1, 2021. https://doi.org/10.1016/j.pharmthera.2020.107649.
11. Yang, B.; Rodgers, M. T. Base-Pairing Energies of Proton-Bound Heterodimers of Cytosine and Modified Cytosines: Implications for the Stability of DNA i-Motif Conformations. *J Am Chem Soc* 2014, *136* (1), 282–290. https://doi.org/10.1021/ja409515v.
12. Amato, J.; Iaccarino, N.; Randazzo, A.; Novellino, E.; Pagano, B. Noncanonical DNA Secondary Structures as Drug Targets: The Prospect of the i-Motif. *ChemMedChem* 2014, *9* (9), 2026–2030. https://doi.org/10.1002/cmdc.201402153.
13. Ja410934b 1..11 | Enhanced Reader.
14. Benabou, S.; Aviñó, A.; Eritja, R.; González, C.; Gargallo, R. Fundamental Aspects of the Nucleic Acid I-Motif Structures. *RSC Adv* 2014, *4* (51), 26956–26980. https://doi.org/10.1039/c4ra02129k.
15. Fujii, T.; Sugimoto, N. Loop Nucleotides Impact the Stability of Intrastrand I-Motif Structures at Neutral PH. *Physical*

Chemistry Chemical Physics 2015, *17* (26), 16719–16722. https://doi.org/10.1039/c5cp02794b.
16. Iaccarino, N.; Cheng, M.; Qiu, D.; Pagano, B.; Amato, J.; Di Porzio, A.; Zhou, J.; Randazzo, A.; Mergny, J. Effects of Sequence and Base Composition on the CD and TDS Profiles of I-DNA. *Angewandte Chemie International Edition* 2021, *60* (18), 10295–10303. https://doi.org/10.1002/anie.202016822.
17. (17) Serrano-Chacón, I.; Mir, B.; Escaja, N.; González, C. Structure of I-Motif/Duplex Junctions at Neutral PH. *J Am Chem Soc* 2021, *143* (33), 12919–12923. https://doi.org/10.1021/jacs.1c04679. 1. Patel, D. J.; Phan, A. T. n.; Kuryavyi, V., Human telomere, oncogenic promoter and 5′-UTR G-quadruplexes: diverse higher or-der DNA and RNA targets for cancer therapeutics. Nucleic acids research 2007, 35, (22), 7429-7455.
18. Ciribilli, Y.; Singh, P.; Spanel, R.; Inga, A.; Borlak, J., Decoding c-Myc networks of cell cycle and apoptosis regulated genes in a transgenic mouse model of papillary lung adenocarcinomas. Oncotarget 2015, 6, (31), 31569.
19. Zhang, Z.; Wu, Q.; Wu, X.-H.; Sun, F.-Y.; Chen, L.-M.; Chen, J.-C.; Yang, S.-L.; Mei, W.-J., Ruthenium (II) complexes as apoptosis inducers by stabilizing c-myc G-quadruplex DNA. European Journal of Medicinal Chemistry 2014, 80, 316-324.
20. Georgiades, S. N.; Abd Karim, N. H.; Suntharalingam, K.; Vilar, R., Interaction of metal complexes with G-quadruplex DNA. Angewandte Chemie International Edition 2010, 49, (24), 4020-4034.
21. Brooks, T. A.; Hurley, L. H., Targeting MYC expression through G-quadruplexes. Genes & cancer 2010, 1, (6), 641-649.
22. Yan, S.; Zheng, Z.; Cui, Y.; Mi, Y.; Liu, H.; Zhao, X.; Luo, D., C-MYC G-QUADRUPLEX STABILIZATION AND CYTOTOXICITY OF AN OXADIAZOLE-BEARING RUTHENNIUM (II) COMPLEX. REVUE ROUMAINE DE CHIMIE 2021, 66, (5), 423-433.
23. Platella, C.; Guida, S.; Bonmassar, L.; Aquino, A.; Bonmassar, E.; Ravagnan, G.; Montesarchio, D.; Roviello, G. N.; Musumeci, D.; Fuggetta, M. P., Antitumour activity of resveratrol on human melanoma cells: A possible mechanism related to its interaction with malignant cell

telomerase. Biochimica et Biophysica Acta (BBA)-General Subjects 2017, 1861, (11), 2843-2851.
24. Quagliariello, V.; Berretta, M.; Buccolo, S.; Iovine, M.; Paccone, A.; Cavalcanti, E.; Taibi, R.; Montopoli, M.; Botti, G.; Maurea, N., Polydatin reduces cardiotoxicity and enhances the anticancer effects of sunitinib by decreasing pro-oxidative stress, pro-inflammatory cytokines, and nlrp3 inflammasome expression. Frontiers in Oncology 2021, 11.
25. Lanzilli, G.; Cottarelli, A.; Nicotera, G.; Guida, S.; Ravagnan, G.; Fuggetta, M. P., Anti-inflammatory effect of resveratrol and polydatin by in vitro IL-17 modulation. Inflammation 2012, 35, (1), 240-248.
26. Platella, C.; Raucci, U.; Rega, N.; D'Atri, S.; Levati, L.; Roviello, G. N.; Fuggetta, M. P.; Musumeci, D.; Montesarchio, D., Shedding light on the interaction of polydatin and resveratrol with G-quadruplex and duplex DNA: A biophysical, computational and biological approach. International Journal of Biological Macromolecules 2020, 151, 1163-1172.
27. Bai, L.; Ma, Y.; Wang, X.; Feng, Q.; Zhang, Z.; Wang, S.; Zhang, H.; Lu, X.; Xu, Y.; Zhao, E., Polydatin Inhibits Cell Viability, Mi-gration, and Invasion Through Suppressing the c-Myc Expression in Human Cervical Cancer. Frontiers in cell and developmen-tal biology 2021, 9.
28. Bulheller, B. M.; Hirst, J. D., DichroCalc—circular and linear dichroism online. Bioinformatics 2009, 25, (4), 539-540

CHAPTER 4 SIDE COLLABORATION

CD, UV, and In Silico Insights on the Effect of 1,3-Bis (10 -uracilyl) -2-propanone on Serum Albumin Structure

(Publication n°2)

Francesca Greco, Andrea Patrizia Falanga, Monica Terracciano, Carlotta D'Ambrosio, Gennaro Piccialli, Giorgia Oliviero, Giovanni Nicola Roviello, and Nicola Borbone.

Abstract: 1,3-diaryl-2-propanone derivatives are synthetic compounds used as building blocks for the realization not only of antimicrobial drugs but also of new nanomaterials thanks to their ability to selfassemble in solution and interact with nucleopeptides. However, their ability to interact with proteins is a scarcely investigated theme considering the therapeutic importance that 1,3-diaryl-2-propanones could have in the modulation of protein-driven processes. Within this scope, we investigated the protein binding ability of 1,3-bis (10 -uracilyl)-2-propanone, which was previously synthesized in our laboratory utilizing a Dakin–West reaction and herein indicated as U2O, using bovine serum albumin (BSA) as the model protein. Through circular dichroism (CD) and UV spectroscopy, we demonstrated that the compound, but not the similar thymine derivative T2O, was able to alter the secondary structure of the serum albumin leading to significant consequences in terms of BSA structure with respect to the unbound protein (∆β-turn + ∆β-sheet = +23.6%, ∆α = −16.7%) as revealed in our CD binding studies. Moreover, molecular docking studies suggested that U2O is preferentially housed in the domain IIIB of the protein, and its affinity for the albumin is higher than that of the reference ligand HA 14−1 (HDOCK score (top 1–3 poses): −157.11 ± 1.38 (U2O); −129.80 ± 6.92 (HA 14−1); binding energy: −7.6 kcal/mol (U2O); −5.9 kcal/mol (HA 14−1)) and T2O (HDOCK score (top 1–3 poses): −149.93 ± 2.35; binding energy: −7.0 kcal/mol). Overall, the above findings suggest the ability of 1,3-bis(10 -uracilyl)-2-propanone to bind serum albumins and the observed reduction of the α-helix structure with the concomitant increase in the β-structure are consistent with a partial protein destabilization due to the interaction with U2O.

Probing the Ca2+ mobilizing properties on primary cortical neurons of a new stable cADPR mimic
(Publication n°6)

Stefano D'Errico, Francesca Greco, Andrea Patrizia Falanga, Valentina Tedeschi, Ilaria Piccialli, Maria Marzano, Monica Terracciano, Agnese Secondo, Giovanni Nicola Roviello, Giorgia Oliviero, Nicola Borbone.

Abstract: Cyclic adenosine diphosphate ribose (cADPR) is a second messenger involved in the Ca2+ homeostasis. Its chemical instability prompted researchers to tune point by point its structure, obtaining stable analogues featuring interesting biological properties. One of the most challenging derivatives is the cyclic inosine diphosphate ribose (cIDPR), in which the hypoxanthine isosterically replaces the adenine. As our research fo- cuses on the synthesis of N1 substituted inosines, in the last few years we have produced new flexible cIDPR analogues, where the northern ribose has been replaced by alkyl chains. Interestingly, some of them mobilized Ca2+ ions in PC12 cells. To extend our SAR studies, herein we report on the synthesis of a new stable cIDPR derivative which contains the 2″S,3″R dihydroxypentyl chain instead of the northern ribose. Interestingly, the new cyclic derivative and its open precursor induced an increase in intracellular calcium concentration ([Ca2+]i) with the same efficacy of the endogenous cADPR in rat primary cortical neurons.

FINAL DISCUSSION

In conclusion, the results of my research activity still aim to support the growth potential of oligonucleotides and analogs by embracing one of the most modern applications of biotechnology. The thesis challenges overcoming the poor bioavailability of nucleic acids and analogs by exploiting the active targeting approach to realize new anticancer platforms with reduced side effects and toxicities. As the preferred approach, the antisense approach has been extensively studied. In this context, as an anticancer tool, I have studied the synthesis and application of one the most efficient oligo-mimetic: the Peptide Nucleic Acid.

The forerunner study focused on the design and synthesis of a novel PNA oligomer with antisense activity against a CD5 mRNA tract. The expression level of CD5 protein, upregulated in B-CLL patients, was modulated after treatment with the proposed antisense PNA. Thus, the decisive biological effect of PNA in inhibiting the translation mechanism was confirmed. Furthermore, the combined administration of antisense PNA and a traditional anticancer drug was also evaluated in the reported study, the greater antitumor effects documented by the combo paved the way for more effective therapeutic strategies in B-CLL.

Likewise, considering the PD-L1 pivotal role in cancer onset, it has been designed a novel PNA sequence complementary to a region of PD-L1. The importance of this target exhorted the study of two different delivery platforms. The comparison between the two systems allowed us to measure the active targeting effects of each platform. The administration of the anti-PD-L1 PNA has been set up as here described:

1. development of a controlled release system based on diatomite nanoparticles. The driving force of active targeting for PNA release exploited the altered redox balance of the tumor environment to trigger the PNA release by reducing the disulfide bonds between the NP surface and the PNA.
2. development of a new PNA delivery platform mediated by the surface of oncolytic adenovirus capable of selectively infecting and proliferating only in tumor cells.

The comparative analysis allowed us to appreciate the antitumor effect of both strategies, evaluating that in presence of a selective delivery approach, there was always an improvement in the

mediated target treatments. Beyond the antitumoral effect mediated by both the delivery systems, from the comparative studies appeared that the oncolytic adenovirus carrier could not be used as a delivery platform without considering its own antitumoral nature. Hence, the redox-responsive diatomite nanoparticles gained a winning result.

Broadly speaking, enhancing the uses and applications of targeted therapy is the foundation for personalized medicine. The diagnosis and treatment of tumor pathologies, in fact, certainly represent the clinical area in which personalized medicine has reached and could still reach its maximum development. For this reason, the endorsement of this aspect of oligonucleotides as therapeutics must be further investigated.

Contemporarily, my research has also impacted the study of non-canonical secondary structures of DNA. Since conformational changes in biomolecules is a way for cells to communicate, studies of the DNA secondary structures represent a way of interpreting the sophisticated language of DNA. Keeping in mind that the G-quad and C-quad (i-motif) structures are the most representative alternative secondary structure in the genome, part of my studies have been directed to discover new findings derived from the G-quad and i-motif conformations presence.

For this purpose, a structural study was conducted to evaluate the interaction of natural compounds with G-quadruplexes. The stabilization resulting from the interaction of trans-polydatins with a promoter region of the c-myc oncogene, previously formed in G-quadruplex, was investigated.

On the other hand, although the i-motif is widely represented in the genome we provided the design and synthesis of novel cytosine-rich oligonucleotides structurally modified by non-nucleotide linkers able to form stable i-motif structures. This last finding primes the way for the interdisciplinary employment of i-motif conformations.

Appendix

List of publications

1. *Cytosine-rich oligonucleotides incorporating a non-nucleotide loop: A further step towards the obtainment of physiologically stable i-motif DNA*

Greco, Francesca; Marzano, Maria; Falanga, Andrea; Terracciano, Monica; Piccialli, Gennaro; Roviello, Giovanni; D'errico, Stefano; Borbone, Nicola; Oliviero, Giorgia.

International Journal of Biological Macromolecules (2022). 219. 10.1016/j.ijbiomac.2022.08.016.

2. *CD, UV, and In Silico Insights on the Effect of 1,3-Bis(1'-uracilyl)-2-propanone on Serum Albumin Structure*

Greco Francesca; Falanga Andrea Patrizia; Terracciano Monica; D'Ambrosio Carlotta; Piccialli Gennaro; Oliviero Giorgia; Roviello Giovanni Nicola; Borbone Nicola.

Biomolecules. 2022 Aug 3;12(8):1071. doi: 10.3390/biom12081071. PMID: 36008965; PMCID: PMC9405946.

3. *Exploring the Parallel G-quadruplex Nucleic Acid World: A Spectroscopic and Computational Investigation on the Binding of the C-myc Oncogene NHE III1 Region by the Phytochemical Polydatin*

Greco Francesca; Musumeci Domenica; Borbone Nicola; Falanga Andrea Patrizia; D'Errico Stefano; Terracciano M, Piccialli I; Roviello Giovanni Nicola; Oliviero Giorgia.

Molecules. 2022 May 7;27(9):2997. doi: 10.3390/molecules27092997. PMID: 35566347; PMCID: PMC9099682.

4. *Exploring a peptide nucleic acid-based antisense approach for CD5 targeting in chronic lymphocytic leukemia*

Cesaro Elena; Falanga Andrea Patrizia; Catapano Rosa; Greco Francesca; Romano Simona; Borbone Nicola; Pastore Arianna; Marzano Maria; Chiurazzi Federico; D'Errico Stefano; Piccialli Gennaro; Oliviero Giorgia; Costanzo Paola; Grosso Michela.

PLOS ONE. (2022). 17(3): e0266090. https://doi.org/10.1371/journal.pone.0266090

5. *Development of Surface Chemical Strategies for Synthesizing Redox-Responsive Diatomite Nanoparticles as a Green Platform*

for On-Demand Intracellular Release of an Antisense Peptide Nucleic Acid Anticancer Agent

Terracciano Monica; Fontana; Flavia; Falanga Andrea Patrizia; D'Errico Stefano; Torrieri Giulia; Greco Francesca; Tramontano Chiara; Rea Ilaria; Piccialli Gennaro; De Stefano Luca; Oliviero Giorgia; Santos Helder; Borbone Nicola.

Small 2022, 18, 2204732. https://doi.org/10.1002/smll.202204732

6. *Probing the Ca2+ mobilizing properties on primary cortical neurons of a new stable cADPR mimic*

D'Errico Stefano; Greco Francesca; Falanga Andrea Patrizia; Tedeschi Valentina; Piccialli Ilaria; Marzano Maria; Terracciano Monica; Secondo Agnese; Roviello Giovanni Nicola; Oliviero Giorgia; Borbone Nicola.

Bioorg Chem. 2021 Dec;117:105401.

doi:10.1016/j.bioorg.2021.105401. Epub 2021 Oct 2. PMID: 34662754.

Oral communications

1. *Development of an innovative biosensor for diagnosing Chronic Lymphocytic Leukemia: a PNA probe can detect CD5 biomarker in vitro.*

*Francesca Greco *, A.P.Falanga, S. D'Errico, M. Marzano, M. Terracciano, L. De Stefano, I. Rea, M. Gioffrè, T. Crisci, G. Chianese, N. Borbone, G.Piccialli, G. Oliviero.*

3rd Workshop "I chimici per le biotecnologie" (13th-14 2020, Naples)

2. *A novel antisense strategy Peptide Nucleic Acid-based to downregulate CD5 expression in Chronic Lymphocytic Leukemia*

Francesca Greco, Elena Cesaro ,Andrea Patrizia Falanga,Rosa Catapano, Simona Romano, Nicola Borbone, Arianna Pastore, Maria Marzano, Stefano D'errico, Gennaro Piccialli, Giorgia Oliviero, Paola Costanzo, Michela Grosso.*

7th International Electronic Conference on Medicinal Chemistry (1st – 30th November 2021)

3. *Synthesis and characterization of an antisense PNA to downregulate the pd-l1 protein overexpression in cancer cells*

*F. Greco *, A.P. Falanga, M. Terracciano, V. Cerullo, G. Piccialli, N. Borbone, G. Oliviero.*

XLVI "A. Corbella" International Summer School on Organic Synthesis – ISOS 2022 (12th– 16th June 2022, Gargnano).

4. *Synthesis and characterization of an antisense PNA to downregulate the pd-l1 protein overexpression in cancer cells*

F. Greco, A.P. Falanga, M. Terracciano a, V. Cerullo, G. Piccialli, N. Borbone a, G. Oliviero.*

4° workshop "I chimici per le biotecnologie (1 July 2022, Parma)

Poster presentation

1. *Development of an innovative biosensor for diagnosing Chronic Lymphocytic Leukemia: a PNA probe can detect CD5 biomarker in vitro.*

*Francesca Greco *, A.P.Falanga, S. D'Errico, M. Marzano, M. Terracciano, L. De Stefano, I. Rea, M. Gioffrè, T. Crisci, G. Chianese, N. Borbone, G.Piccialli, G. Oliviero.*

3rd Workshop "I chimici per le biotecnologie" (13th-14 2020, Naples)

2. *Design and synthesis of a cADPR mimic as a novel tool for monitoring the intracellular Ca^{2+} concentration*

S.D'Errico, N.Borbone, A.P.Falanga, I.Piccialli, M.Marzano, M.Terracciano, F.Greco, G.Piccialli, G.Oliviero*

The 1st International Electronic Conference on Biomolecules (ECBM 2020) "Natural and bio-inspired therapeutic for human diseases"